

Response to referee #1 (in RC2)

RC: This paper presents a new method for retrieving the ice particle number concentration  $N_i$  for glaciated clouds, which should be useful for understanding aerosol interactions with ice clouds and the contribution of homogeneous vs. heterogeneous ice nucleation in cirrus clouds. A satellite remote sensing scheme for  $N_i$  is needed since field campaigns cannot adequately inform us how  $N_i$  varies with latitude and the seasons. The paper is well organized and well written, and usually cites the relevant literature. The quality of the figures is good. The methods developed in Sec. 5 for testing the retrieval are especially creative and effective.

AR: We are thankful to the referee for all the useful comments that greatly helped us to improve the quality and clarify of this study. In particular concerning the influence of the PSD shape assumptions, the use of 2D-S data and the consistency between the analyses of  $N_i$  climatologies presented in the 2 papers of this study. Detailed responses to each comment are provided below.

---

RC: A critical limitation of the retrieval algorithm is the use of a normalized universal ice particle size distribution, or PSD (Delanoë et al., 2005), where it is assumed that all PSD in nature conform to this normalized PSD shape. This normalized PSD is based on a four-parameter gamma function (Eq. 4) where parameters  $N_0$  and  $k$  can be deduced through their link with other operationally retrieved properties (IWC and  $N_0^*$ ) while PSD parameters  $\alpha$  and  $\beta$  need to be fixed as constants. This is of little consequence regarding  $\beta$ , which affects the largest ice particles having the lowest concentrations. But this is of major consequence regarding  $\alpha$ , which strongly influences the smallest ice particles that govern  $N_i$ . This is not mentioned in the paper. The small end of the PSD is sensitive to the rate of ice nucleation which is sensitive to the cloud updraft  $w$  (with higher  $w$  making  $\alpha$  more negative, and  $N_i$  higher), as well as the aggregation rate that removes smaller ice particles having higher concentration (Herzogh and Hobbs, 1985, QJRMS; Mitchell, 1991, JAS). Thus, some discussion on this topic is warranted, especially on the errors that may result from “non-standard” conditions where atypical updrafts are common (such as over steep orography).

AR: We thank the referee for pointing out the need for further discussion regarding the impact of non-retrieved shape parameters of the size distributions ( $\alpha$  and  $\beta$ ). We completely agree that this was lacking in the original manuscript.

DARDAR unfortunately does not rigorously account for these uncertainties in its operational retrievals, as they are only represented by additional fixed errors considered on the lidar and radar measurements. More rigorous techniques exist to propagate uncertainties on  $\alpha$  and  $\beta$  through the optimal estimation scheme but they would be too time consuming for an operational algorithm based on active instruments. However, the variability of these two parameters and the subsequent impact on DARDAR has been thoroughly discussed in Delanoë et al. [2014]. It can be noted that, as a result of this study, a revised version of the PSD parameterization has been proposed (notably with a less negative  $\alpha$ , leading to less small ice crystals and a lower  $N_i$ ) but is not yet implemented in the operational product. The referee is therefore absolutely correct in saying that the fixed  $\alpha$  and  $\beta$  parameters constitute a strong limitation to our current method that should be further highlighted. These points are now discussed in Sec. 3.1 and in Appendix

A3 of the revised manuscript and are supported by additional figures in the supplementary materials (see Fig. S3).

The impact of the choice of  $\alpha$  and  $\beta$  on the PSD shape is clearly shown in the upper panel of Fig. S3, and the subsequent impact on  $N_i$  because of straying from the selected values ( $\alpha = -3$  and  $\beta = -1$ ) is quantified in the lower figure. In order to propose a range of realistic shape parameters, values extracted by Delanoë et al. [2014] from individual in situ campaigns are used (color code in upper figure and shapes in the lower figure). IWC and  $N_0^*$  values representative of 3 temperature bins are selected, although it should be kept in mind that each couple of coefficients from the D14 campaigns can realistically applied to only one of these temperature ranges. In agreement with the referee's comment, it can be observed that one D14 campaign displays a more negative  $\alpha$ , namely the "subvisible" campaign, which corresponds to cirrus measured at temperatures between  $-80$  to  $-60^\circ\text{C}$  during CRYSTAL-FACE (Cirrus Regional Study of Tropical Anvils and Cirrus-Layers-Florida Area Cirrus Experiment). We recognize that this analysis remains preliminary but it should still allow to provide rough estimates of the uncertainties on  $N_i^{5\mu\text{m}}$ ,  $N_i^{25\mu\text{m}}$  and  $N_i^{100\mu\text{m}}$  to the reader. This overall uncertainty is here considered to be typically better than about 50% (when considering the variability between all D14 campaigns). This value is now reported in Sec. 3.1 and A3 of the revised manuscript.

---

RC: The lead author gave a nice talk about this retrieval at the A-Train Symposium in 2017. Henceforth,  $N_i$  refers to  $N_i$  for ice particle maximum dimension  $D > 5\mu\text{m}$ . Slide 20 of this presentation, showing global distributions of  $N_i$  for  $10^\circ\text{C}$  intervals, appears almost identical to Fig. 9 of this paper for  $T < -30^\circ\text{C}$ , except that the  $N_i$  legends differ. The  $N_i$  values reported in the presentation are higher by a factor of about 1.7 relative to the  $N_i$  reported in Fig. 9 of this paper. What is the reason for this difference?

AR: We are grateful that the referee took the time to verify the consistency between this paper and the results presented during the A-Train Symposium. The figure referred to here (slide 20 of this presentation, available on <http://atrain2017.org>), corresponded to the  $N_i$  integrated from  $D_{\min} = 1\mu\text{m}$ . This may not have been clearly expressed during the presentation but is suggested by the absence of mention to the size in the label. The  $1\mu\text{m}$  threshold was initially used at early stages of our analyses, but was subsequently changed to  $5\mu\text{m}$  as it is impossible at this point to reasonably evaluate DARDAR-LIM between 1 and  $5\mu\text{m}$ . Also, as discussed before, uncertainties related to PSD shape assumptions are likely to be even more important if  $D_{\min} = 1\mu\text{m}$ .

Fig. 1 shown in this response corresponds to the distribution of  $N_i^{1\mu\text{m}}$  based on the dataset used for this paper. It can be noted that similar values to those shown during the A-Train Symposium presentation are found, despite small differences in absolute values. These could be due to an error found in the script that converts  $D_{\min}$  from maximum diameter to an equivalent melted size prior to the numerical integration of the PSD, which led to slightly underestimated  $D_{\min}$  and thus to higher concentration. This error was corrected before creating the dataset used in these papers. To the best of the first author's knowledge, there should be no other difference between Fig. 1 of this response and the figure in the A-Train Symposium presentation.

---

Major Comments

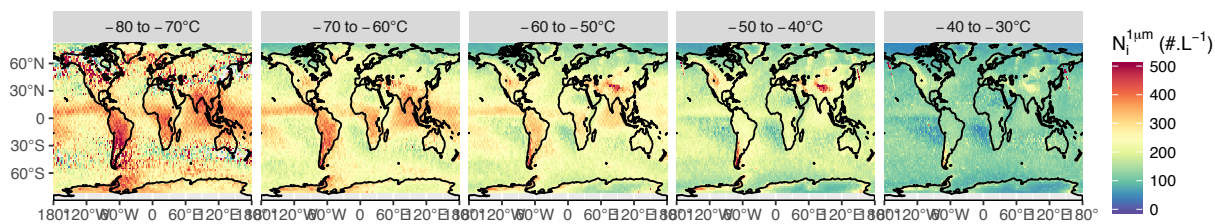


Figure 1: Spatial distribution of  $N_1^{1\mu m}$  from 2006 to 2016, averaged in a  $2 \times 2^\circ$  lat-lon grid and per  $10^\circ$  C temperature bin from  $-80$  to  $-30^\circ$  C.

1. RC: Page 8, line 25: The 2DS photodiode array length is  $1280 \mu\text{m}$ , which should be noted. Evidently the “time dimension” is used to size particles up to  $3205 \mu\text{m}$ ; please indicate the particle selection criteria used to size and count particles.

AR: We are very thankful to the referee for this comment that has led us to investigate in greater detail the various selection criteria for particle size and count that are available for the 2D-S instrument.

In the original manuscript, ATTREX-2014 data was processed with the method  $M_1$ , or  $M_7$  method when available. There are important differences between these methods, in particular concerning the size selection, which are for instance extensively described and discussed in Lawson [2011] and Erfani and Mitchell [2016]. The SPARTICUS data was treated with the  $M_1$  method only, as  $M_7$  isn’t operationally available in the ARM database. Comparing concentrations from these 2 methods should not be an issue as Erfani and Mitchell [2016] showed that the number concentration in small particle isn’t significantly different between them.

Nevertheless, after further discussion with the 2D-S data providers at SPEC Inc. (P. Lawson and S. Woods), it appeared that using a SPARTICUS dataset based on a  $M_4/M_1$  processing could be better adapted to the needs of this study. By  $M_4/M_1$  it is meant that the  $M_4$  method is used for particles sizes less than  $365 \mu\text{m}$  and the  $M_1$  is used otherwise. A main differences between these two methods is that  $M_4$  resizes out-of-focus particles to equivalent in-focus spheres [Korolev, 2007]. This becomes problematic when the ice particle shapes become strongly non-spherical, and this method can therefore only be applied to small particles. Consequently, it was decided with the SPARTICUS 2D-S data providers that a combined  $M_4/M_1$  processing method should be used here.

The differences between the PSDs obtained from  $M_1$  alone and  $M_4/M_1$  are shown in Fig. 2 of this document. The main difference occur for sizes between about  $30$  to  $100\text{--}200 \mu\text{m}$ , with typically more particles with  $D < 100 \mu\text{m}$  and less particles larger than this threshold. As a consequence, the bi-modal structure is less pronounced in  $M_4/M_1$ , but it also is clear from this figure that the results discussed in the original manuscript are not changed by this transition from  $M_1$  to  $M_4/M_1$  2D-S data. It can also be mentioned that slightly less flights with  $M_4/M_1$  treatments were available on the ARM database.

As a response to this comment, Sec. 3.2.1 was edited to explicitly mention the use of the  $M_n$  methods.

Regarding the photodiode specifications, it seems that the 2DS photodiode array length is (if referring to the actual physical size of the array) of about  $7.3 \text{ mm}$  [Lawson et al., 2006]. However, we fully agree with the referee that, because (i) the equivalent size of each photodiode

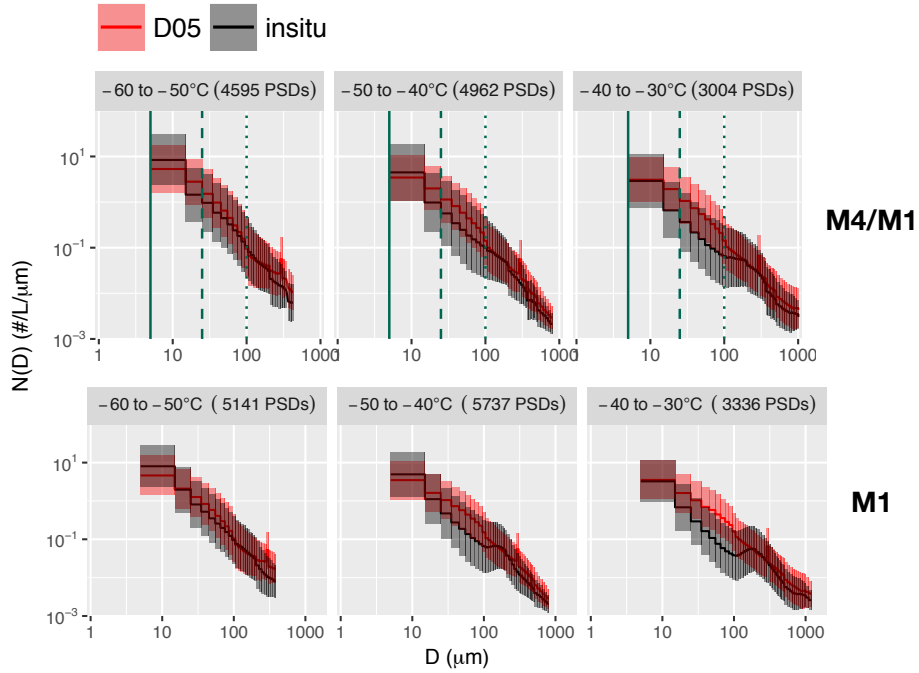


Figure 2: Comparison between the SPARTICUS 2D-S PSDs obtained from the M4/M1 (top; as in Fig. 1 of the revised manuscript) and the M1 method (bottom; as in Fig. 1 of original manuscript.)

is about  $10 \mu\text{m}$  (considering the laser beam magnification) and (ii) the 2D-S being equipped with 128 photodiode, this instrument technically measures particules up to  $1280 \mu\text{m}$  in size and so an extension to  $3205 \mu\text{m}$  is only possible by using a time dimension (i.e., by using 2 consecutive measurements a of  $1280 \mu\text{m}$  particle). This is now mentioned in Sec. 3.2.1 of the revised manuscript.

---

2. RC: Figure 5 and Sec. 4.2: For  $T > -50\text{C}$ , by what factor is  $N_i (D_{\min} = 5\mu\text{m})$  overestimated, on average? For  $T \geq -50\text{C}$ ?

AR: Based on Fig. 5 of the original manuscript, an overestimation of  $N_i^{5\mu\text{m}}$  by a factor of about 2 to 3 can be considered if looking at the distance between the modes of the 2D-S and DARDAR-LIM distributions. We nevertheless agree that this figure did not provide an easy way to clearly quantify the bias, and visually comparing the modes does not really provide a real statistical estimate of the differences between DARDAR-LIM and the 2D-S. This figure has therefore been edited in order to include the geometric means associated with each histogram (DARDAR-LIM, D05 and 2D-S) for each temperature bin and instrumental condition. These should allow for a more quantitative discussion of the biases, included in the revised Sec. 4.2. For instance, overestimations by about 10 to 30% and 20 to 60% are found in the mean values of  $N_i^{25\mu\text{m}}$  by D05 and DARDAR-LIM, respectively.

Complementarily, a line showing a factor of 3 around to one-to-one line has also been added to Fig. 4 of the original manuscript, now Fig. S4 of the complementary materials.



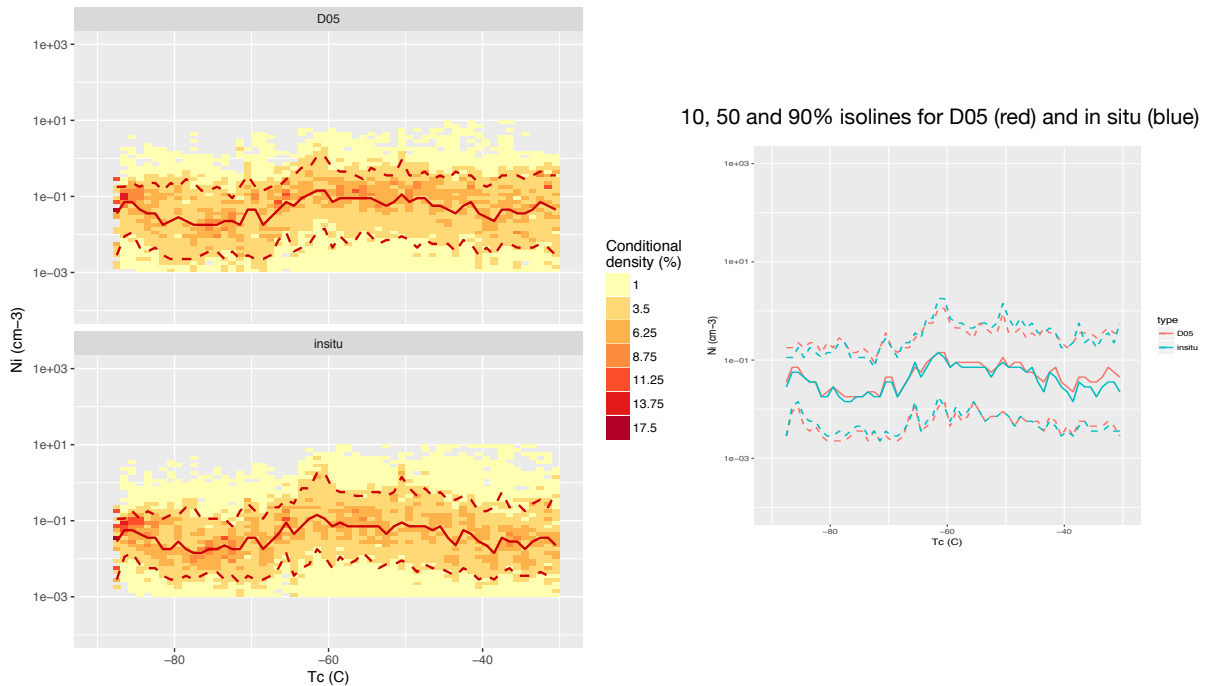


Figure 3: Left: Conditional density of  $N_i^{5\mu\text{m}}$  as function of the temperature, obtained from the insitu data used in this paper (bottom) and the corresponding D05 predictions (top). Plain red lines indicate the median and dashed lines show the 10th and 90th percentiles. The right panel directly compares the medians and 10th and 90th percentile lines.

3. RC: Page 21, lines 9-12: The strong temperature dependence of Ni mentioned here appears at variance with the in situ measurements reported in Krämer et al. (2009). Please mention this.

AR: We thank the referee for this comment, which has encouraged us to further compare our  $N_i$  products with the insitu findings in several studies by Krämer et al.

It should first be mentioned that it is very difficult to compare the temperature dependence of  $N_i$  obtained from in situ campaigns to those from global results shown in Sec. 6. In situ measurements are rather sparse and it is often difficult to tell what part of the cloud has been sampled. However, the enormous advantage of the dataset by Krämer et al is indeed that it consistently merges numerous in situ campaigns and should therefore tend to being comparable to global satellite data. This dataset is still being improved as airborne campaigns are continuously being added. The  $N_i(T)$  relation reported in Krämer et al. [2009] was based on a dataset that was not yet very large and contains some flights in mountain wave clouds that enhanced the frequencies of higher ice concentrations. A new, yet unpublished, dataset called JULIA does not confirm the (slight) dependence of Ni on T shown in Krämer et al. [2009]

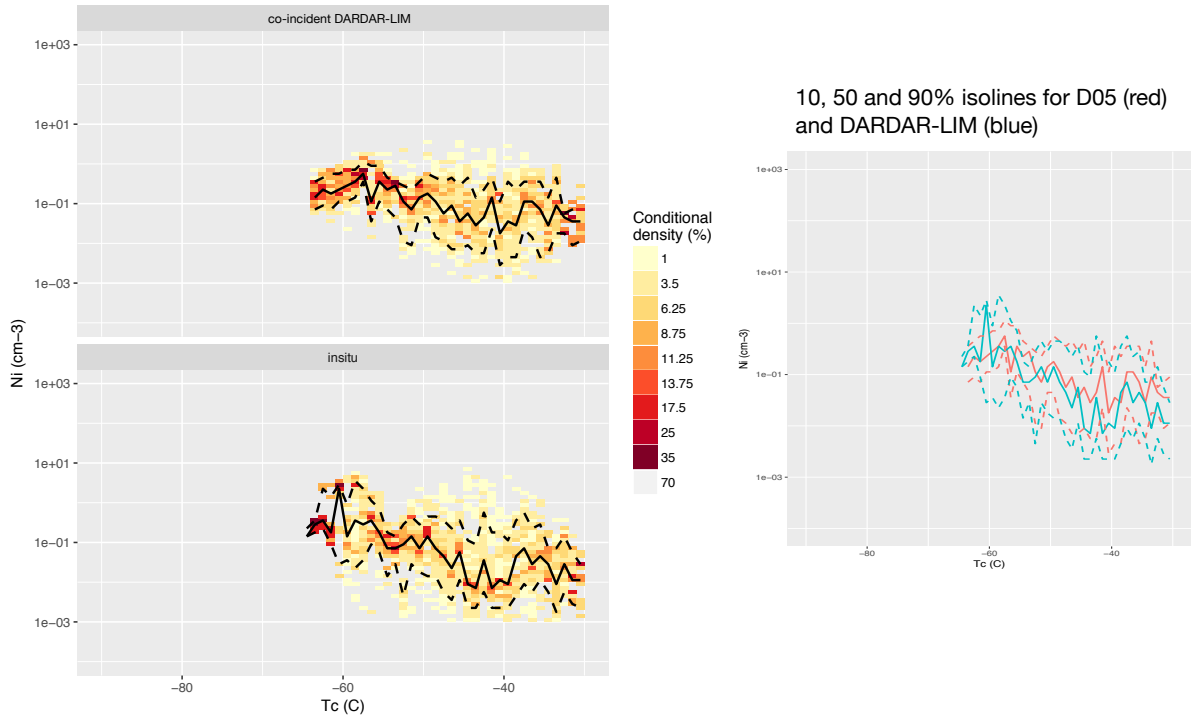


Figure 4: Same as 3 but for DARDAR-LIM  $N_i^{5\mu\text{m}}$  compared to co-incident in situ observations during SPARTICUS.

(personal communication, M. Krämer).

This comment has motivated us to compare the  $N_i(T)$  obtained in this study with the one from JULIA. Due to the complexity of this task, intermediate steps were taken. First, we have verified that the issues noted with D05 (notably due to its limited shape assumptions) does not create clear biases in the  $N_i(T)$  relation. This is shown in Fig. 3 attached to this response, which compares the  $N_i(T)$  dependency obtained from the dataset used in this study to that predicted by D05 based on the in situ data. It can be noted that the consistency of the relation found from our dataset to the one from JULIA has been verified, although this cannot be directly demonstrated here due to the latter being unpublished. Fig. 3 clearly shows that D05 is very well capable of reproducing the relation between  $N_i^{5\mu\text{m}}$  and  $T_c$  found in the in situ measurements, and so similar results could be expected from DARDAR. This has been verified by looking at the same relations based on the co-incident SPARTICUS flights. Fig. 4 in this response shows that DARDAR-LIM reproduces well the  $N_i(T)$  relation observed by the 2D-S. We have checked that these results also hold for  $N_i^{25\mu\text{m}}$  and that they are not sensitive to instrumental conditions.

Consequently, it could be expected that  $N_i(T)$  obtained from global DARDAR-LIM estimates are reasonable and that the observations from Sec. 6 are not necessarily at variance with in situ observations. However, the results presented here are preliminary and further analyses are necessary to confirm them. For instance, it would require to subset similar regions, cloud

type or distance from cloud top by comparison the in situ data. Rigorously assessing the consistency between  $N_i(T)$  observed from DARDAR-LIM and from in situ measurement would be extremely interesting but unfortunately out of the scope of this paper. These results will be the focus in a following study.

---

4. RC: Figure 9 and Sec. 6.1: For  $T > -50^\circ\text{C}$ ,  $N_i$  tends to be lower over regions characterized by extensive marine stratus, like off the west coasts of South America and Africa (from equator and southwards). Is this result real, or is it an artefact of the retrieval? If the latter is true, please explain.

AR: We thank the referee for pointing this out. It is correct that  $N_i$  (for all integration thresholds) tend to be relatively lower in marine stratocumulus regions. There does not seem to be any obvious reason to doubt the retrieval method in these regions but it should indeed be kept in mind that there are relatively less ice clouds in these subsidence regions. The spatial distributions of retrieval counts have now been added to supplementary materials (see Fig. S8) to help determining which regions correspond to statistically significant retrievals. Another physical explanation could be that there are no convective clouds in these regions, which seem to drive the high  $N_i^{5\mu\text{m}}$  and  $N_i^{25\mu\text{m}}$  observed in this figure. This is supported by the seasonal variabilities in  $N_i$  maps shown in Fig. 8 of the revised manuscript. Consequently, values observed correspond to thin cirrus, perhaps remnants of aged anvils or jet stream cirrus, and  $N_i^{5\mu\text{m}}$  values below  $100\text{L}^{-1}$  for  $T > -50^\circ\text{C}$  are thus not surprising, as mentioned in comment #7 of this review. It also means that  $N_i^{5\mu\text{m}}$  in this regions are more comparable to cloud-top values observed in the part 2 paper. This is now noted in Sec. 6.1 of the revised manuscript.

---

5. RC: Page 21, lines 14-19: A similar finding was reported in Mitchell et al. (2016, ACPD), where the highest  $N_i$  were associated with mountainous terrain. (Although this paper was rejected since the editor felt the retrieved  $N_i$  values were too high, and therefore could not be used to infer nucleation modes, no arguments cast doubt on the spatial and temporal relative differences in  $N_i$ , which still appear meaningful.)

AR: We fully agree that further comparisons to existing climatologies would be beneficial to the analyses in Sec. 6.1. A new paragraph discussing comparisons results by Mitchell et al. [2016, 2018] is now included.

---

6. RC: Page 22, lines 7-9: It is more meaningful to compare model results against observations than vice-versa. Suggest removing this paragraph. For example, in the modeling study by Zhou et al. (2016, ACP), the sensitivity of homo- and heterogeneous ice nucleation to various model parameters and updraft schemes were evaluated. Depending on how these are represented, one can get a broad range of  $N_i$ -temperature dependences, including  $N_i$  that is relatively insensitive to temperature (similar to the in situ observations of Krämer et al., 2009, ACP), and that modeling result would not support these DARDAR-LIM findings.

AR: We agree with this comment, comparisons to modeling would require further analyses that are not in the scope of this paper. This paragraph is now removed

---

7. RC: Figure 10 and Sec. 6.2:  $N_i$  ( $D_{\min}=5 \mu\text{m}$ ) in the tropics appears contrary to the  $N_i$  results in Fig. 1 and Fig. 5 of Part 2 of this study by Gryspeerdt et al. (submitted). Fig. 1a of Gryspeerdt et al. show  $N_i$  near cloud top while their Fig. 5 shows that  $N_i$  does not change appreciably with distance below cloud top (up to 3 km from cloud top) between  $-50$  and  $-60^\circ\text{C}$ . Assuming this result extends to other temperatures, the cloud top results in Fig. 1a of Gryspeerdt et al. should also be approximately valid below cloud top. Regarding Fig. 1a in Gryspeerdt et al., for  $T > -65^\circ\text{C}$ ,  $N_i$  is never higher in the tropics relative to the midlatitudes. Between  $-55$  and  $-40^\circ\text{C}$ , where the most optically thick cirrus clouds exist (cirrus defined as clouds having  $T < -38^\circ\text{C}$ ),  $N_i$  in the tropics is substantially lower than  $N_i$  in the midlatitudes. In Fig. 10 of Part 1 (Sourdeval et al.),  $N_i$  increases abruptly in the tropics for  $T < -40^\circ\text{C}$  (shown by the dashed curve), with  $N_i$  here being typically higher than  $N_i$  at similar  $T$  in the midlatitudes. This result appears opposite to the findings in Fig. 1a of Gryspeerdt et al. (Part 2). In addition, the CALIPSO  $N_i$  retrievals of Mitchell et al. (2016, ACPD) qualitatively support the findings of Gryspeerdt et al. (in terms of relative differences), and the in situ measurements from Mühlbauer et al. (2014) show relatively lower “peak  $N_i$ ” values in anvil cirrus (vs. frontal, jet stream and ridge-crest cirrus). Finally, several studies (e.g. Jensen et al., 2013, PNAS; Spichtinger and Krämer, 2013, ACP), show that tropical tropopause layer (TTL) cirrus tend to have  $N_i < 30 \text{ L}^{-1}$ . Since the areal coverage of TTL cirrus exceeds that of anvil cirrus, and TTL cirrus tend to be higher than anvil cirrus (Gasparini et al., 2017, J. Climate), the  $N_i$  of  $\sim 200 \text{ L}^{-1}$  in the TTL region in Fig. 10 appears at variance with in situ observations. Please comment on, and, if possible, reconcile these issues.

AR: We thank the referee for this interesting comment. It has motivated us to further compare the spatial distributions obtained from cloud-top  $N_i$  ( $N_{i(top)}$ ) (part 2) vs. the “all cloud” maps (part 1).

It is first important to point out that this is not straightforward as these two maps are not necessarily representative of the same cloud types within a given temperature bin. For instance, the  $N_{i(top)}$  map between  $-50$  and  $-60^\circ\text{C}$  (in part 2) only shows concentrations for clouds that have a cloud-top within this temperature bin, whereas the total  $N_i$  map (in part 1) also features values that are within deep convective clouds. It is observed that the high values of  $N_i^{5 \mu\text{m}}$  and  $N_i^{25 \mu\text{m}}$  only appear in convective regions, which is confirmed by the seasonal variabilities showed in Fig. 8. The sampling difference is also clear when comparing retrieval counts between  $N_{i(top)}$  and  $N_i$  per  $T_c$  bin, now showed in Fig. 1 of the revised part 2 paper and in Fig. S8 of the revised part 1 paper, respectively. Nearly no retrievals are present in the tropic for the  $N_{i(top)}$  map, whereas convective clouds are present in the  $N_i$  map. To support this analysis, it can be noted that high  $N_i$  values found between  $-50$  and  $-60^\circ\text{C}$  within deep convective clouds is in agreement with modeling results by Paukert et al. [2017], who also reports  $N_{i(top)}$  lower than  $N_i$  for this cloud type.

It could as well be argued that the CALIPSO  $N_i$  retrievals presented in Mitchell et al. [2016, 2018] are also more comparable to the  $N_{i(top)}$  map as the thermal infrared measurements used in these studies extinguishes within a few optical depth. It is therefore reasonable to expect that retrievals from these studies would not compare exactly to  $N_i$  maps presented in part 1 but more to the  $N_{i(top)}$  maps presented in part 2, as it is the case (in terms of relative variations of  $N_i$ ).

Regarding the absolute values of  $N_i$ , we completely agree with the referee that the ones

presented our maps may not be completely exact. An overestimation by a factor of 2, or even 3, could be expected on  $N_i^{5\mu\text{m}}$  considering all uncertainties on the retrievals (especially concerning the assumptions on the PSD shape). These uncertainties should be smaller on  $N_i^{25\mu\text{m}}$ , as the impact of the shape is less significant, and the spatial distributions of  $N_i^{25\mu\text{m}}$  are now also included in Fig. 7 of the revised manuscript. The relative variations are similar to those found for  $N_i^{5\mu\text{m}}$ , despite a slightly weaker temperature dependence, possibly due to the less directly link between particles with  $D > 25\mu\text{m}$  and homogeneous freezing processes. Maximum  $N_i^{25\mu\text{m}}$  (found at  $T_c < -70^\circ\text{C}$  in the tropics) are about  $100\text{L}^{-1}$ , which is more consistent with values found in the studies referred to here by the referee. Exact comparisons between our results and previous in situ findings would nevertheless require further investigation that are out of the scope of this study.

Sec. 6.1 has been substantially edited to include all the aforementioned discussions, and further explanations on the consistency between  $N_i$  and  $N_{i(top)}$  maps are now also given in the revised part 2 manuscript

---

8. RC: Page 23, lines 1-3 and Fig. 10: Fig. 10 and this text indicate that in the midlatitudes for  $T_i < -40\text{C}$ ,  $N_i$  is highest during winter and lowest during summer. This same result was found in Mitchell et al. (2016). One of the ACP review criteria questions is “Do the authors give proper credit to related work and clearly indicate their own new/original

AR: We agree that the consistency between our results and those of Mitchell et al. [2016], especially in the mid-latitude, should have been included. A paragraph is now dedicated to these comparisons in Sec. 6.1.

---

Minor comments

RC: 1. Page 15, line 9: much => slightly?

2. Page 19, line 6: follows => follow?

3. Page 22, line 13: at => as?

4. Figure 10 caption: Mention the meaning of the dashed curve.

5. Page 20, line 1: an => a?

AR: We thank the referee for pointing this out, these typos are corrected in the revised manuscript.

## References:

- J. Delanoë, A. J. Heymsfield, A. Protat, A. Bansemer, and R. J. Hogan. Normalized particle size distribution for remote sensing application. *J. Geophys. Res.*, 119(7):4204–4227, 2014. doi: 10.1002/2013JD020700. URL <http://dx.doi.org/10.1002/2013JD020700>.
- E. Erfani and D. L. Mitchell. Developing and bounding ice particle mass- and area-dimension expressions for use in atmospheric models and remote sensing. *Atmos. Chem. Phys.*, 16(7):4379–4400, 2016. doi: 10.5194/acp-16-4379-2016.
- A. Korolev. Reconstruction of the sizes of spherical particles from their shadow images. part i: Theoretical considerations. *J. Atmos. Oceanic Technol.*, 24(3):376–389, 2007. doi: 10.1175/JTECH1980.1.
- M. Krämer, C. Schiller, A. Afchine, R. Bauer, I. Gensch, A. Mangold, S. Schlicht, N. Spelten, N. Sitnikov, S. Borrmann, M. de Reus, and P. Spichtinger. Ice supersaturations and cirrus cloud crystal numbers. *Atmos. Chem. Phys.*, 9(11):3505–3522, 2009. doi: 10.5194/acp-9-3505-2009.
- R. P. Lawson. Effects of ice particles shattering on the 2d-s probe. *Atmos. Meas. Tech.*, 4(7):1361–1381, 2011. doi: 10.5194/amt-4-1361-2011. URL <http://www.atmos-meas-tech.net/4/1361/2011/>.
- R. P. Lawson, D. O’Connor, P. Zmarzly, K. Weaver, B. Baker, Q. Mo, and H. Jonsson. The 2D-S (Stereo) probe: Design and preliminary tests of a new airborne, high-speed, high-resolution particle imaging probe. *J. Atmos. Oceanic Technol.*, 23(11):1462–1477, 2006. doi: 10.1175/JTECH1927.1.
- D. L. Mitchell, A. Garnier, M. Avery, and E. Erfani. Calipso observations of the dependence of homo- and heterogeneous ice nucleation in cirrus clouds on latitude, season and surface condition. *Atmos. Chem. Phys. Discuss.*, 2016:1–60, 2016. doi: 10.5194/acp-2016-1062.
- D. L. Mitchell, A. Garnier, J. Pelon, and E. Erfani. Calipso (iir-caliop) retrievals of cirrus cloud ice particle concentrations. *Atmospheric Chemistry and Physics Discussions*, 2018:1–60, 2018. doi: 10.5194/acp-2018-526.
- M. Paukert, C. Hoose, and M. Simmel. Redistribution of ice nuclei between cloud and rain droplets: Parameterization and application to deep convective clouds. *J. Adv. Model. Earth Sy.*, 9(1):514–535, 2017. doi: 10.1002/2016MS000841.



Response to referee #1 (in RC4)

AR: We thank Referee #1 for taking the time to read comments from other reviews and provide such insightful comments. This was very helpful to the discussions that have taken place in the context of this overall review process.

This response by Referee #1 very well illustrates that the uncertainties expected on in situ measurements of the concentration in small ice crystals are still not completely understood and require further efforts and investigations. It is clear that large uncertainties occur in the two first size bins of the 2D-S but arguments such as provided here by Referee #1 seem to indicate that measurements in these bins may not be completely meaningless. This is exactly what has initially motivated us to provide the total ice particle concentrations integrated from multiple minimum size thresholds:  $5 \mu\text{m}$ ,  $25 \mu\text{m}$  and  $100 \mu\text{m}$ . As discussed in the manuscript, the absolute values of  $N_i^{5 \mu\text{m}}$  are associated with larger uncertainties than those of  $N_i^{25 \mu\text{m}}$ . However, providing that these issues are clearly stated and discussed, it seems reasonable for  $N_i^{5 \mu\text{m}}$  to still be provided to users, who can then make an educated choice on whether or not this quantity is of interest for their studies. Looking at spatial variations in  $N_i^{5 \mu\text{m}}$ , as mentioned here by Referee #1, are a perfect example of analyses that doesn't require the absolute value to be correct but only the relative changes to be physically meaningful. The results shown in the two parts of this study seem to provide good confidence in the latter point. This comment by Referee #1 has therefore further convinced us that  $N_i^{5 \mu\text{m}}$  should not be completely removed from the revised version of the manuscript.

Finally, it is important to emphasize that satellite products of  $N_i$  are still at an early stage. They have too rarely been attempted and, most importantly, rigorously evaluated before. It is worth noting that, for this reason, "estimates" has been preferred to "retrievals" to describe  $N_i$  in this manuscript. The results presented here, together with the recent studies by Mitchell et al. [2016, 2018], constitute first encouraging steps towards providing more accurate and well understood datasets of  $N_i$  to the community. It is evident that DARDAR-LIM can still largely benefit from further improvements - the evaluation presented in this paper has identified several of them and work is in progress in that direction - but this two-part study also presents evidence that realistic and useful  $N_i$  values can already be reached. The conclusions drawn here hopefully will serve as motivations for further developments of  $N_i$  retrievals from remote sensing measurements.

## References:

- D. L. Mitchell, A. Garnier, M. Avery, and E. Erfani. Calipso observations of the dependence of homo- and heterogeneous ice nucleation in cirrus clouds on latitude, season and surface condition. *Atmos. Chem. Phys. Discuss.*, 2016:1–60, 2016. doi: 10.5194/acp-2016-1062.
- D. L. Mitchell, A. Garnier, J. Pelon, and E. Erfani. Calipso (iir-caliop) retrievals of cirrus cloud ice particle concentrations. *Atmospheric Chemistry and Physics Discussions*, 2018:1–60, 2018. doi: 10.5194/acp-2018-526.

Response to referee #2 (in RC3)

RC: This paper describes an ice concentration retrieval based on the DARDAR CloudSat/CALIPSO combined lidar-radar retrieval. The extension of DARDAR to retrieve ice concentrations, evaluation by comparison with in situ aircraft measurements, and global distributions are discussed. Although the ice concentration retrieval seems reasonable and potentially useful, I have significant concerns with the paper in its current version. In particular, I think the validity of the retrieval in regions without both lidar extinction and radar reflectivity needs much more discussion and evaluation. Also, the use of 2D-S measurements for determining concentrations of small ice crystals is suspect at best. These issues (and others) are discussed in detail below.

AR: We are thankful to the referee for the insightful comments listed in this review. We fully agree with these two major concerns regarding the behaviour of DARDAR-LIM under single-instrument conditions and the uncertainties related to small ice concentrations by the 2D-S. The manuscript has been substantially edited, with the support of supplementary materials and an appendix, to provide further clarifications and discussions on these two points. Detailed answers to each of the referee's comments are provided below.

---

RC: 1. The discussion of the retrieval algorithm in section 2 implicitly assumes that both extinction from the lidar and radar reflectivity are available. The authors should make clear early in the paper that the ice concentration retrieval is dubious in cirrus that are not detected by both radar and lidar (either too optically thin for detection by the CloudSat radar or below optically thick layers where the CALIOP lidar is blocked). When only lidar backscatter or radar reflectivity are available, the ice concentration is entirely dependent on the assumed size distribution. Mean PSDs are shown in the paper, but aircraft data shows that enormous PSD temporal and spatial variability is typically prevalent in cirrus. With only lidar or radar data available, this variability cannot be captured by the retrieval.

AR: The referee is absolutely correct in that DARDAR-LIM can be impacted by the absence of either lidar or radar reflectivity (i.e., referred to as radar- and lidar-only retrievals) and that this issue should explicitly be discussed in the manuscript. Following this comment, the behaviour of the algorithm under such conditions is now discussed in Sec. 3.1 as well as in Appendix A1. These sections clarify that two aspects are important to consider:

- First, it is correct that optimal retrievals should be expected in lidar-radar conditions due to having two pieces of information available to constrain both scaling parameters of the normalized size distribution ( $D_m$  and  $N_0^*$ ). When only one instrument is available, DARDAR must rely on a priori assumptions, and in particular a relation between  $N_0^*$ ,  $\alpha_{\text{ext}}$  and the temperature. Nevertheless, DARDAR also propagates, through its optimal estimation scheme, information vertically by using lidar-radar retrievals within the same column to further constrain this relation. The quality of lidar-only and radar-only  $N_i$  estimates is therefore difficult to predict. A propagation of the operational retrieval uncertainties is now proposed in the revised manuscript (see Sec. A2 and figure S2 of the supplementary materials). Figure S2 in particular shows that errors are indeed minimum in lidar-radar conditions, about 25% against 50% in lidar- and radar-only conditions, at their respective

maximum of occurrence. These numbers should nevertheless be carefully accounted for because DARDAR was not designed to retrieve  $N_i$  and importance quantities, like the shape of the PSD through the  $\alpha$  and  $\beta$  parameters, are not rigorously represented.

- However, it should also be pointed out that, despite instrumental sensitivity, it can be reasonable to expect that lidar-only  $N_i$  estimates can in certain conditions be more accurate than lidar-radar retrievals. Indeed, lidar-only regions are often met at cloud top where the ice clouds are optically thin. Such conditions are likely to be met by small ice crystals that have not yet aggregated, and therefore display a rather monomodal size distribution that is easier to accurately be reproduced by D05. We recall that D05 assumes a monomodal shape and our study has already shown that this is a major limitation of the current method. Under lidar-radar conditions, i.e. deeper in a thick cloud structures, the PSDs are likely to become more complex and the monomodal-shape approximation followed by D05 will not hold anymore, which leads to more uncertain retrievals. In order to clarify this point, a new figure (Fig. 3) has been added to the revised manuscript. This figure explicitly compares the in situ PSDs measured by the 2D-S (coincident with A-Train overpasses, in black) to the PSD predicted by D05 using  $D_m$  and  $N_0^*$  from the 2D-S (i.e. the “optimal retrievals”; in red) and the PSD actually retrieved by DARDAR-LIM (i.e. using  $D_m$  and  $N_0^*$  from DARDAR; in blue). It is clear that in many cases the DARDAR-LIM PSD is close to the D05 PSD, indicating enough sensitivity to properly constrain  $D_m$  and  $N_0^*$  in all instrumental conditions. It is also interesting to note that good agreements to the 2D-S PSDs are obtained in lidar-only conditions due to their tendencies to be monomodal with less large crystals.

Therefore, deciding on the accuracy of DARDAR-LIM  $N_i$  estimates in lidar-only conditions is not trivial, as it depends on the instrumental sensitivity as well as the PSD shape that are met in a given cloud parcel. The manuscript has been revised to make this more clear to the reader.

---

RC: 2. Page 6, lines 24-28: It would be helpful if some formal estimate of the uncertainties in  $N_i$  retrievals associated with measurement uncertainties could be provided.

AR: We agree that a formal estimates of the uncertainties on  $N_i$  due to instrumental error and non-retrieved parameters of the forward model in DARDAR could be useful to the reader. These were not provided in the original manuscript because, as mentioned in the previous point, DARDAR was not designed to estimate  $N_i$  and so some non-retrieved parameters in the retrieval algorithm that are important to  $N_i$  (such as the PSD small mode shape) have not clearly been considered and included for error calculation. We now propagated the Gaussian uncertainties attached to IWC and  $N_0^*$  in order to provide quantitative uncertainties on  $N_i^{5\mu\text{m}}$ ,  $N_i^{25\mu\text{m}}$  and  $N_i^{100\mu\text{m}}$ , which could be considered as lower error bounds. This is now discussed in Sec. 3.1, A2 and Fig. S2 of the supplements. Complementarily, the impact of the shape parameters on  $N_i$  is also discussed in this section and in Fig. S3.

---

RC: 3. Page 6, lines 26-27: Further discussion of the the uncertainty in  $N_i$  retrieval associated with PSD shape assumption should be included. Perhaps examples could be provided as a guide.

AR: We thank the referee for this comment, we fully agree that more discussion on the impact of the PSD shape should be included. This is now discussed in Sec. 3.1, A3 and in Fig. S3 of the supplements. In this figure, several examples of PSD shapes are considered. Values of  $N_0^*$  and  $D_m$  representative of 3 temperature bins, based on the in situ campaigns used in this study, are considered as well as examples of 9 couples of  $\alpha$  and  $\beta$  parameters extracted from several in situ campaigns by Delanoë et al. [2014]. It clearly appears in the top figure of S3 that these parameters indeed greatly influence the assumed PSD shape. Consequences on  $N_i^{5\mu\text{m}}$ ,  $N_i^{25\mu\text{m}}$  and  $N_i^{100\mu\text{m}}$  are shown below. Considering the typical values reported by Delanoë et al. [2014], an overestimation of about 50% can reasonably be expected on  $N_i^{5\mu\text{m}}$ , with the exception of one sub-visible (thin cirrus) case representative of a much higher concentration in small crystals than D05. Lower uncertainties due to the PSD shape are expected on  $N_i^{25\mu\text{m}}$  due to a lesser influence of the  $\alpha$  parameter.

---

RC: 4. As noted in the manuscript, only 2D-S data was available from SPARTICUS. The 2D-S ice concentrations are overwhelmingly dominated by the 1st size bin (5-15  $\mu\text{m}$ ). Artifacts and uncertainties render the first bin or two of 2D-S measurements relatively useless. Most 2D-S data users do not use concentrations in the first two bins in their analyses because of the large uncertainties. I would recommend excluding the first two bins in the PSD comparisons shown in Figure 1 for temperature bins for which little or no ATTREX data is available. Also, I think it is inappropriate to use  $N_i^{5\mu\text{m}}$  data from the SPARTICUS 2D-S-only dataset for evaluation of the satellite retrievals. The MACPEX 2D-S data should only be used for  $N_i^{25\mu\text{m}}$  and  $N_i^{100\mu\text{m}}$ .

AR: We agree with the referee concerning the high degree of uncertainties of the ice concentrations measured in the 2D-S first bin (5-15  $\mu\text{m}$ ). Despite that this matter is still actively discussed, as the response to this review provided by Referee #1 (RC4) illustrates very well, it is important to be careful when dealing with this data. That is why several  $D_{\text{min}}$  thresholds were used in this study, including a  $D_{\text{min}}=25\mu\text{m}$  that allowed for excluding the first two size bins of the 2D-S. The reader can then decide on the degree of trust they put on the 2D-S data and, subsequently, on the DARDAR-LIM evaluation. It should be noted that all three thresholds investigated here ( $D_{\text{min}}=5$  25 and 100  $\mu\text{m}$ ) are part of the product that will soon be made publicly available. After careful consideration, we have decided to not completely remove  $N_i^{5\mu\text{m}}$  analyses from the manuscript but the discussions were instead largely edited throughout the manuscript to remind that  $N_i^{25\mu\text{m}}$  is a more trustworthy reference when it comes to 2D-S data. Further discussions on issues with 2D-S measurements in its first 2 bins have also been included in Sec. 3.2 and 3.3. Finally, all analyses (including for the case study and geographic distributions) are now extended to  $N_i^{25\mu\text{m}}$ . The conclusion was also edited to stress the need for more evaluation of the DARDAR-LIM  $N_i^{5\mu\text{m}}$  because of these issues. We hope that this should provide enough information to the reader to make an educated choice regarding its use of the  $N_i$  dataset that will be provided co-jointly with these papers.

However, it should be noted that  $N_i^{5\mu\text{m}}$  predictions by D05 agree fairly well with the FCDP and NIXE-CAPS measurements (with a possible overestimation by less than a factor of 2 but a good correlation). This gives in further confidence in that  $N_i^{5\mu\text{m}}$  by DARDAR-LIM are useful and contain physical meaning, even if further investigation based on coincident flights will be required to assess the accuracy of their absolute value.

Following the referee’s advice Fig. 1 was edited to exclude the two first bins of 2D-S where little SPARTICUS data is available by comparison to ATTREX (i.e., for  $T_c < -60^\circ\text{C}$ ). However, the MACPEX 2D-S data has not been added to this study as it would not add much more information by comparison to the dataset already used, especially considering the uncertainties on the 2D-S.

Finally, it should be mentioned that, following a comment in by Referee #1 (in RC2), the SPARTICUS dataset has been updated. The new dataset is now based on 2D-S data treated with a different processing method for  $D < 365\ \mu\text{m}$  (see response to RC2 or edits in Sec. 3.2.1 of the revised manuscript). This does not change in any way the conclusions of this study but slight differences in the figures will be noted.

---

RC: 5. Figure 1: Indicate in figure or caption which temperature ranges correspond to ATTREX data (mostly  $< -70^\circ\text{C}$ ) and SPARTICUS data (warmer temperature ranges).

AR: We agree that this would be a useful information to the readers. In order to avoid including too much information in Fig. 1, an histogram showing the temperature distribution for all included campaigns is added in the supplements (Fig. S1) and is referred to in the caption of Fig. 1.

---

RC: 6. Figure 2: The authors should note and discuss the D05 overestimate (by factor of 2-3) for small ( $D < 10\ \mu\text{m}$ ) particles in  $-80$  to  $-70^\circ\text{C}$  bin compared to ATTREX measurements.

AR: Thank you for noting this important point. It is true that D05 seems to overestimate the concentration in small ice crystals (smaller than about 15 to 25  $\mu\text{m}$ ) due to a too steep representation of the PSD small mode (too negative  $\alpha$  coefficient). This is now noted and discussed in the analysis of this figure (now Fig. 1 in revised manuscript) and the now Fig. 2 of the revised manuscript, which indicates a subsequent overestimation by a factor less than 2 on  $N_i^{5\ \mu\text{m}}$ . This point is also now mentioned in the conclusion as it is an aspect that should be improved in future parameterizations used for  $N_i$  retrievals. It can be mentioned that the PSD parameterization planned for the next versions of DARDAR possesses a less steep representation of the concentration in small particles (i.e., a less negative  $\alpha$ , as can be noted in Fig. S3, the new parameterization being “all (DARDAR)”). Improvements are therefore expected in future DARDAR-LIM versions, but discussing them at this stage is out of the scope of this paper.

---

RC: 7. Figure 3: The small sample volume of the FCDP instrument results in discretization of the ice number concentration in steps of about  $12\ \text{conc. bin}^{-1}$ . In other words, the FCDP instrument cannot effectively measure ice concentrations smaller than about  $10\text{-}20\ \text{L}^{-1}$  if the data is used at 1 Hz (as in this study). The CAS data has a similar sample volume issue. Since ice concentrations are often dominated by the small crystals sampled by FCDP and CAS, I would recommend not showing the in situ vs D05 comparisons for concentrations less than 10



$L^{-1}$ . In some of the temperature bins, the data extends to ice concentrations greater than 1000  $L^{-1}$ . Extending the upper limit on the Figure 3 axes would be helpful to show how well the retrieval compares with in situ measurements at higher ice concentrations.

AR: We completely agree with the referee that the FCDP and CAS instruments are not optimal for measuring small concentrations less than about 15  $L^{-1}$ . However, it can be argued that in the occurrence of such small  $N_i$ , the overall concentration is likely to be dominated by large particles that are not measured by these two instruments. Additionally, a minimum detection limit is used in the treatment of the CAS and FCDP data so that concentration smaller than that threshold leads to no signal. Therefore, concentrations less than 15  $L^{-1}$  only originate from ice crystals larger than 25  $\mu\text{m}$  in the 1-Hz dataset. This is not necessarily the case in our dataset as 10 1-Hz PSDs are here merged to create PSDs representative of a 10-s sampling (comparable to the CloudSat overpass, as discussed in Sec. 3.2.2). We therefore kept 1  $L^{-1}$  as the lowest value for these analyses.

Nevertheless, following this comment, the concentrations axes in Fig. 3 (now Fig. 2 of the revised manuscript) have been extended to 5000  $L^{-1}$  to encompass all measured concentrations.

---

RC: 8. Figure 3: The authors should note that discrepancies up to factors of 2-3 occur but are difficult to see with the log-log axis scales.

AR: We thank the referee for pointing this out. Additional lines have been added to this figure in order to explicitly show a factor of 2 and 3 around the one-to-one line.

---

RC: 9. Will the  $N_i$  data be made publicly available? If so, data quality flags should be included to indicate when both radar and lidar signals are available as well as when the retrieval is questionable based on in situ comparisons?

AR: Yes, we think that it is extremely important that this dataset is made publicly available as soon as possible, hopefully together with these papers. A procedure has been initiated to distribute this  $N_i$  dataset via the ICARE data center (<http://www.icare.univ-lille1.fr>), next to the operational DARDAR product. Level-2 (orbital retrievals) as well as Level-3 (daily/monthly gridded means) are currently being produced and we hope to be able to announce a DOI together with the final version of the manuscript. A choice was made to wait for the end of the reviews in case of significant changes to the methodology were requested.

The L2 dataset will include  $N_i^{5\mu\text{m}}$ ,  $N_i^{25\mu\text{m}}$ ,  $N_i^{100\mu\text{m}}$ , as well as numerous flags that will allow to filter for instrumental conditions, cloud types and iteration numbers. It is difficult to create an additional quantitative flag that will reflect the conclusions of the in situ comparison made in this paper but the temperature (from ECMWF reanalyses) is included in the L2 dataset to provide some flexibility to the users in that direction. A filtering following what has been done for Sec. 6 of this study will be applied for the L3 climatologies.

RC: 10. Page 14, lines 1-6: I do not understand what the authors are saying here. I was under the impression that Figures 2 and 3 simply showed statistical comparisons between the in-situ-measured and retrieved PSDs and ice concentrations. The first paragraph of section 4.2 suggests the comparisons in section 4.1 were ideal cases. Perhaps this idealization should be explained and emphasized at the beginning of section 4.1.

AR: We thank the referee for noting that this point was not very clear. As indicated in the introduction and the beginning of Sec. 3.2, two main questions are investigated in this in situ evaluation. First it is determined if D05, which predicts PSDs on the basis of IWC and  $N_0^*$ , is capable of accurately predicting the concentration in small particle and therefore  $N_i^{5\mu\text{m}}$  and  $N_i^{25\mu\text{m}}$ . Second, it is checked that enough sensitivity is available in lidar and radar measurements to properly constrain these two input parameters. Fig. 1-3 of the original manuscript responded to the first question by comparing in situ measurements of PSDs and  $N_i$  to equivalent predictions by D05 (obtained on the basis of IWC and  $N_0^*$  extracted from the same in situ data). In other terms, these correspond to optimal  $N_i$  estimates from DARDAR-LIM since we assume that IWC and  $N_0^*$  perfectly fit the in situ measurements, as if they were perfectly retrieved by DARDAR. This allows to disentangle the errors originating from PSD shape assumptions, which are tested here, from errors related with a lack of sensitivity in lidar-radar measurements, which are investigated later using co-incident flights. Therefore, these comparisons allow to clearly conclude on the limitations of the D05 parameterization and what needs to be improved (e.g. a better representation of the bi-modality) to obtain better  $N_i$  estimates.

This point was clarified by editing the first paragraphs of Sec. 4.1 and 4.2 in the revised manuscript.

---

RC: 11. Section 4.2: I am not convinced that the near-coincident in situ/satellite retrieval comparisons are useful given the enormous spatial/temporal variability in cloud properties and the corresponding need for very close time and space coincidences for meaningful comparisons. Not surprisingly, the scatter in the comparisons shown in Figure 4 is very large, spanning 1-2 orders of magnitude.

AR: We completely acknowledge that it is extremely difficult to colocate and compare aircraft and satellite measurements. Such attempts are still common to evaluated satellite products, including DARDAR [Deng et al., 2012], and always show a strong scatter in direct comparisons. However, even if 2D-S and DARDAR-LIM and not comparable one-to-one, the constraints taken here on the time and space collocation (i.e., 5 km and 30 min) should at least allows them to be statistically representative of similar cloud samples.

Fig. 4 of the original manuscript did not provide very good quantitative comparisons and so it is now moved to the supplementary materials (see Fig. S4 and S5). It can still be noted that the average agreement (around the center of the  $1-\sigma$  isoline in dashed white) agrees well with the one-to-one line for  $N_i^{100\mu\text{m}}$  and shows an expected overestimation by a factor of about 2 to 3 for  $N_i^{25\mu\text{m}}$  and  $N_i^{5\mu\text{m}}$ . This overestimation is consistent with expectations from the limited representation of the PSD shape by D05, as can be observed by comparing Fig. S4 and S5.

Instead, comparisons of the PSDs measured by the 2D-S, predicted by D05 based on 2D-S data, and retrieved by DARDAR-LIM are shown in the new Fig. 3 of the revised manuscript. This figure shows that DARDAR-LIM PSDs are very consistent with the D05 predictions,

meaning that the cloud volumes sampled by the 2D-S and CloudSat/CALIPSO are statistically comparable most each temperature bins and instrumental conditions. The comparisons in terms of histograms, shown in Fig. 4 of the revised manuscript, now also include mean  $N_i$  values to allow for a more quantitative statistical comparisons.

Section 4.2 has therefore been substantially edited to include and adapt to these new analyses, which should provide more convincing evidence of the statistical comparability of 2D-S and coincident DARDAR-LIM products.

---

RC: 12. Page 15, line 9-10: In contrast to the statement here, the DARDAR-LIM retrieval overestimates  $N_{D>5\mu\text{m}}$  and  $N_{D>25\mu\text{m}}$  compared to SPARTICUS data even in the  $-60$  to  $-50^\circ\text{C}$  temperature bins.

AR: We thank the referee for pointing this out. The corresponding sentence has now been removed from the revised manuscript because this section has been substantially edited, following the response to the previous point. As a response to this comment, lines have been added in Fig. 4 of the original manuscript (now Fig. S4) in order to explicitly show a factor of 3 around the one-to-one line and identify more clearly these overestimations.

---

RC: 13. Figure 5: The comparisons shown here are very difficult to see, particularly those for lidar-only and radar-only retrievals. The relative agreement between lidar-radar, radar-only, and lidar-only retrievals should be shown in a separate figure, particularly since the lidar-only and radar-only retrievals are suspect. Also, as discussed above, the SPARTICUS 2D-S-only ice concentrations for  $D>5\mu\text{m}$  are dominated by the first size bin, with enormous associated uncertainties. The comparisons with SPARTICUS 2D-S-only ice concentrations including the first bin are of little value, possibly misleading, and should be removed.

AR: We acknowledge that Fig. 5 of the original manuscript (now also Fig. 5) did not provide clear quantitative messages regarding the differences between 2D-S, D05 and DARDAR-LIM. These were even more difficult to observe for lidar-only and radar-only conditions as often less retrievals are available. We have responded to this issue by included the values of geometric means of  $N_i^{5\mu\text{m}}$ ,  $N_i^{25\mu\text{m}}$  and  $N_i^{100\mu\text{m}}$  for 2D-S, D05 and DARDAR-LIM. The overall mean values are shown, as well as the values corresponding to  $N_i$  estimates obtained in lidar-, radar-only and lidar-radar conditions. Also, as advised by the referee, individual histograms for each of these conditions are shown in Fig. S6 to provide a more clear idea concerning the influence of different instrumental conditions on the retrievals.

Regarding the evaluation of  $N_i^{5\mu\text{m}}$ , we have chosen to keep the corresponding plots in this analyses for the reasons discussed in the response to point 4. However, we fully agree with the referee that great care should be taken when presenting results using concentration from the first size bin of the 2D-S. Sec. 4.2 has therefore been edited so that its analyses are more centered on  $N_i^{25\mu\text{m}}$  and to contain an explicit warning to the reader that  $N_i^{25\mu\text{m}}$  constitutes the better reference concentration for the 2D-S. The revised conclusion also repeats this message as a reminded that more evaluation of  $N_i^{5\mu\text{m}}$  remains necessary.

RC: 14. Page 19, lines 8-10: the lack of clear transitions in retrieved properties between the lidar-only, lidar-radar, and radar-only regions does not necessarily mean the lidar- only and radar-only  $N_i$  retrievals are credible.

AR: We agree with this comment, a lack of transition between lidar/radar-only and lidar-radar regions does not necessarily prove the quality of  $N_i$  estimates obtained in single-instrument conditions. This sentence was more meant as an observation rather than a definite proof, and has therefore been toned down in the revised manuscript. This sentence is also more justified now that the quality of lidar- and radar-only  $N_i$  estimates is further discussed in the revised Sec. 4.2. Nevertheless, this lack of transition is still worth commenting on as it represents a very impressive feature of the DARDAR algorithm, which allows for a real multispectral consistency between it's lidar and radar retrievals. It also shows that some information is used to constrain the  $N_i$  estimates as there do not seem to jump back to some a priori value.

---

RC: 15. Figure 8: Scatter plots of  $N_{D>5\mu\text{m}}$  and  $N_{D>100\mu\text{m}}$  versus  $N_{2D-S}$  would provide much clearer comparisons between the retrievals and measurements. Further, the points could be color coded to indicate whether they are in the lidar-only, lidar-radar, and radar-only regions. In the discussion of Figure 8, the authors claim good agreement between the in situ and retrieved ice concentrations, and they dismiss glaring discrepancies as being caused by the imperfect time coincidence. This argument seems unjustified. The flight track segment has been chosen for good time/space coincidence.

AR: We thank the referee for this comment, it has allowed us to realize that the in situ analyses included in the case study was perhaps not clearly explained. Because of this, and following a comment in RC1 this figure has been moved to supplementary materials (see Fig. S7) and is now only briefly mentioned. This is also justified since this figure mainly supported the previous conclusions, with redundant results. We however think that this figure can in this format still provide good insights on the quality of DARDAR-LIM as it shows that the satellite estimates are to some extent well capable of reproducing the spatial variability in  $N_i^{5\mu\text{m}}$ ,  $N_i^{25\mu\text{m}}$  and  $N_i^{100\mu\text{m}}$  measured by the 2D-S. This is why scatterplots are not proposed for this figure, especially since scatterplots have already been widely examined before. The added-value of figure is to show a consistency in the spatial distribution along the aircraft flight.

We nevertheless agree with the referee's comments and have added information on the instrumental conditions met in DARDAR-LIM in the new figure (see color background in Fig. S7). The  $N_i^{25\mu\text{m}}$  is also included in this study, as it now represents the new reference for small ice concentration from the 2D-S. Finally, the part of the flight leg that was further away from the satellite overpass (more than 10 km) has been removed and the coordinates have been changed so that the reader can easy grasp the temporal and spacial distance between the aircraft track and the satellite overpass.

We agree that discrepancies appear, in particular in the  $N_i^{25\mu\text{m}}$  comparisons and during the descending leg, which we attributed to the distance (about 10 km) from the track. The hypothesis of different cloud sampling between the satellite and the aircraft appears reasonable especially since different  $N_i^{100\mu\text{m}}$  values are noted during this descending leg. We recall that no serious issues are expected in the DARDAR-LIM  $N_i^{100\mu\text{m}}$  estimates based on the previous in situ evaluations and note that similar increases of  $N_i^{100\mu\text{m}}$  can be observed in Fig. 6(h) (of the

revised manuscript) right next to the descending part of the track. It is therefore reasonable to attribute issues in  $N_i^{100\mu\text{m}}$  to the sampling different cloud volumes, which means that differences in  $N_i^{5\mu\text{m}}$  and  $N_i^{25\mu\text{m}}$  could as well be expected in this area.

---

RC: 16. Section 5.3: The authors describe a cloud formation scenario with air parcels ascending across the  $-40^\circ\text{C}$  isoline, which suggests that freezing of liquid drops could be the main ice formation mechanism. Yet they attribute the differences between the high and low ice concentration regions to differences in vertical wind speed and cite the strong sensitivity of  $N_i$  to  $w$  (citing Krämer et al. 2016; papers showing this sensitivity decades earlier should be cited). However, the strong sensitivity to  $w$  occurs primarily when aqueous aerosols freeze, not so much when liquid droplets freeze. Either the description is not clear, or the physical argument made does not make sense.

AR: We are thankful to the reviewer for pointing this out. It appears that the explanation proposed in the original manuscript was misleading. We indeed meant that the relation between  $N_i$  and  $w$ , which we show via the analysis of back-trajectories, is the result of homogeneous freezing events of aqueous aerosols. These events are however likely to occur on top of existing ice crystals formed from liquid droplets, as it is clear that supercooled layers appear close to the region of high  $N_i^{5\mu\text{m}}$  and  $N_i^{25\mu\text{m}}$  (seen in the  $\beta_{\text{ext}}$  profile). We have edited this paragraph and added references and comparisons to studies that analysed these processes [e.g. Kärcher and Ström, 2003, Kärcher et al., 2006].

---

RC: 17. Figures 9 and 10: The discrepancy between  $N_{D>5\mu\text{m}}$  and ATTREX FCDP ice concentrations noted above is apparent in the coldest temperature bins and the TTL. Typical values of  $N_{D>5\mu\text{m}}$  are  $200\text{-}300\text{ L}^{-1}$ , whereas ATTREX in situ measurements indicate ice concentrations of about  $100\text{ L}^{-1}$  (Jensen et al., 2016). It is also interesting that the ice concentrations are higher over continental and convective regions even in the coldest temperature bins (near the tropical tropopause) where the vast majority of clouds form in situ. Additionally, it might be worth noting that the statistics must be poor in the coldest temperature bin poleward of about  $30^\circ$  latitude since such cold temperatures rarely occur there.

AR: We are grateful to the referee for pointing this out and relating these analyses to the observed  $N_i^{5\mu\text{m}}$  discrepancies between D05 and the FCDP at very low temperatures. The section has been edited to note these, as well as the disagreements between concentrations observed in these figures and the findings of Jensen et al. [2013, 2016] for TTL cirrus. These could indeed be caused by a misrepresentation of the small ice concentration in D05, which seems to overestimate the steepness of the concentration towards small particles at low temperatures and therefore overestimates of  $N_i^{5\mu\text{m}}$  (by a factor less than 2). Interestingly, the spatial distributions of  $N_i^{25\mu\text{m}}$  (less impacted by shape assumptions), now added to Fig. 7 of the revised manuscript, indicates concentrations of about  $100\text{ L}^{-1}$  in TTL regions. It can also be noted that  $N_i^{5\mu\text{m}}$  in the same regions and during winter months (see Fig. 8 of revised manuscript), i.e. when in situ clouds should be even more dominant, are about 50% lower. It therefore appears difficult to strongly conclude on disagreements by comparison to in situ observations without an exact knowledge of what cloud type is present in each lat-lon- $T_c$  bin, and further analyses will be

needed to fully assess this disagreement with Jensen et al. [2013, 2016]. This discussion has now been summarized in Sec. 6.1 of the revised manuscript.

We also agree that additional information on the statistical significance of the results provided here would be useful. Fig. S8 and S9 of the supplementary material now indicate the pixel counts corresponding to the spatial and zonal distributions analysed in Sec. 6.

---

RC: 18. Page 22, line 7: Simply stating that the spatial distributions agree with the global model predictions is no doubt too strong. A quick examination shows there are some regions of agreement and some glaring discrepancies. I would either omit this statement or qualify it. Perhaps the comparison really shouldn't be discussed without providing much more detail.

AR: We thank the referee for this comment and fully agree with it. Further comparisons to modeling is beyond the scope of this study and this sentence has been deleted from the manuscript.

---

RC: 19. Section 6.2: Most of the speculations about the physical causes of the zonal-height distributions in this section are either not justified or would require much more detail to adequately discuss. It does not look to me like there is a particularly sharp transition at  $-40^{\circ}\text{C}$ , nor would one be expected given the importance of sedimentation in cirrus. The retrieval probably doesn't work well in the antarctic wintertime stratosphere since PSCs are typically mixtures of ice crystals, NAT particles, and ternary aerosols.

AR: We agree with this point, Sec. 6.2 contained some analyses that remained too hypothetical, such as the attribution of some  $N_i$  patterns to PSCs. After further investigation, it appears that DARDAR retrievals in these regions are highly uncertain due to potential failures in the cloud mask and wrong categorizations of cloud pixels. This does not mean that DARDAR retrievals are always wrong in these regions but further investigation based on the new version of the DARDAR mask should be performed and are out of the scope of this study. It is now clearly stated in the manuscript that this feature in  $N_i$  should not be trusted. Regarding the vertical transition at  $-40^{\circ}\text{C}$ , it could still be argued that  $N_i^{5\mu\text{m}}$  and  $N_i^{25\mu\text{m}}$  values quickly change around this temperature, especially in the tropics.  $N_i^{25\mu\text{m}}$  for instance increases from about  $50\text{L}^{-1}$  to above  $100\text{L}^{-1}$ . We nevertheless agree that this transition cannot be considered sharp and have toned down this analysis.

Following this comment, Sec. 6.2 has been edited to provide further discussion and remove analyses that seemed too far-fetched. The analysis of seasonal variations of  $N_i$  are now also supported by Fig. 8 of the revised manuscript, which shows seasonal variability in spatial distributions. It should also be noted that this section also comes as a natural transition between part 1 and part 2, which further investigates some of the observations made in Sec. 6.2. This is now also reminded.



## References:

- J. Delanoë, A. J. Heymsfield, A. Protat, A. Bansemer, and R. J. Hogan. Normalized particle size distribution for remote sensing application. *J. Geophys. Res.*, 119(7):4204–4227, 2014. doi: 10.1002/2013JD020700. URL <http://dx.doi.org/10.1002/2013JD020700>.
- M. Deng, G. G. Mace, Z. Wang, and R. P. Lawson. Evaluation of several a-train ice cloud retrieval products with in situ measurements collected during the sparticus campaign. *J. Appl. Meteor. and Clim.*, 52(4):1014–1030, 2012. doi: 10.1175/JAMC-D-12-054.1.
- E. J. Jensen, G. Diskin, R. P. Lawson, S. Lance, T. P. Bui, D. Hlavka, M. McGill, L. Pfister, O. B. Toon, and R. Gao. Ice nucleation and dehydration in the tropical tropopause layer. *Proceedings of the National Academy of Sciences*, 110(6):2041–2046, 2013. doi: 10.1073/pnas.1217104110.
- E. J. Jensen, R. Ueyama, L. Pfister, T. V. Bui, R. P. Lawson, S. Woods, T. Thornberry, A. W. Rollins, G. S. Diskin, J. P. DiGangi, and M. A. Avery. On the susceptibility of cold tropical cirrus to ice nuclei abundance. *J. Atmos. Sci.*, 73(6):2445–2464, 2016. doi: 10.1175/JAS-D-15-0274.1.
- B. Kärcher and J. Ström. The roles of dynamical variability and aerosols in cirrus cloud formation. *Atmos. Chem. Phys.*, 3(3):823–838, 2003. doi: 10.5194/acp-3-823-2003.
- B. Kärcher, J. Hendricks, and U. Lohmann. Physically based parameterization of cirrus cloud formation for use in global atmospheric models. *J. Geophys. Res. Atmos.*, 111(D1), 2006. doi: 10.1029/2005JD006219.

Response to referee #3 (in RC1)

RC: The article presents a method to be used as an operational retrieval to derive ice crystal number concentrations of pure ice clouds, Ni, ( $T < -30^\circ \text{C}$ ) from combined spaceborne lidar-radar measurements (CALIPSO-CloudSat) and a thorough evaluation using in situ data from five airborne campaigns. An example of application is shown via a case study, including Lagrangian transport modelling. An interesting result is that regions with stronger updrafts show peaks in Ni with particle sizes  $> 5\text{micron}$  in contrast to regions of mature cloud, as one would expect. At the end, geographical maps and zonal profiles of 10 years of Ni are presented and discussed for particles with sizes  $> 5\text{micron}$  and  $> 100\text{micron}$ . A follow-up paper will use these data in the framework of aerosol-cloud interactions. Ni is an essential microphysical parameter, which is recently used as a prognostic variable in climate models, and therefore it is important to have global observational constraints. The variable is also important for process studies. The combination of lidar and radar measurements, being part of the A-Train, allows to determine the vertical structure of clouds such as top and base of the clouds, cloud layering, as well as ice water content and effective ice crystal diameter. The attempt to derive ice crystal number concentration is relatively recent, as its determination depends on several assumptions (in particular a gamma-modified particle size distribution (PSD) and a specific ice crystal mass-maximal diameter relationship). The presented method is based on a direct constraint of the shape of normalized particle size distributions using lidar extinction and radar reflectivity from the operational liDAR-raDAR (DARDAR) products. 40000 in situ PSD's are used for an evaluation, investigating results separately for ice crystal sizes  $> 5$ ,  $25$  and  $100$  micron, first for the prediction of PSD from  $N_0^*$  and  $D_m$  and then for retrieved Ni. The article is generally well structured and well written. I strongly recommend the publication of this article, after minor revisions.

AR: We thank the referee for all the insightful comments that have greatly helped us to improve the quality of the manuscript. Detailed responses to each of them are provided below.

---

#### Minor Comments

1. RC: 1) The methodology section 2 gains in clarity by integrating the content of section 2.1 into sections 2.3 and section 3.1, in particular as DARDAR products are data and the retrieved variables such as beta-ext, Ze and beta-ext are not defined. In that way the section on the representation of the size distribution gets section 2.1, in which the advantage of using scaled PSD's is described as well as the necessity to assume a certain m-D relationship and a certain shape of PSD. The new section 2.2 (Extracting Ni from DARDAR products) goes then further into detail how to extract Ni from the DARDAR products  $N_0^*$  and IWC. It should be clearly stated in the beginning that from  $N_0^*$  and IWC from DARDAR one deduces  $D_m$  and finally Ni. New Section 2.1: Be careful of replacing DARDAR by 'DARDAR retrieval (see section 3.1)'. Then a short description of the DARDAR products (like in initial sect 2.1) should be integrated into section 3.1. P4,117-18 define beta-ext as (lidar) extinction and Ze as (radar) reflectivity

AR: We are grateful for these suggestions and fully agree with them, sections 2 and 3 have been edited accordingly. Sec. 2 now only focuses on describing the methodology and the DARDAR algorithm is described in Sec. 3.1. It can be noted that further technical details on DARDAR are now also provided in Appendix A.

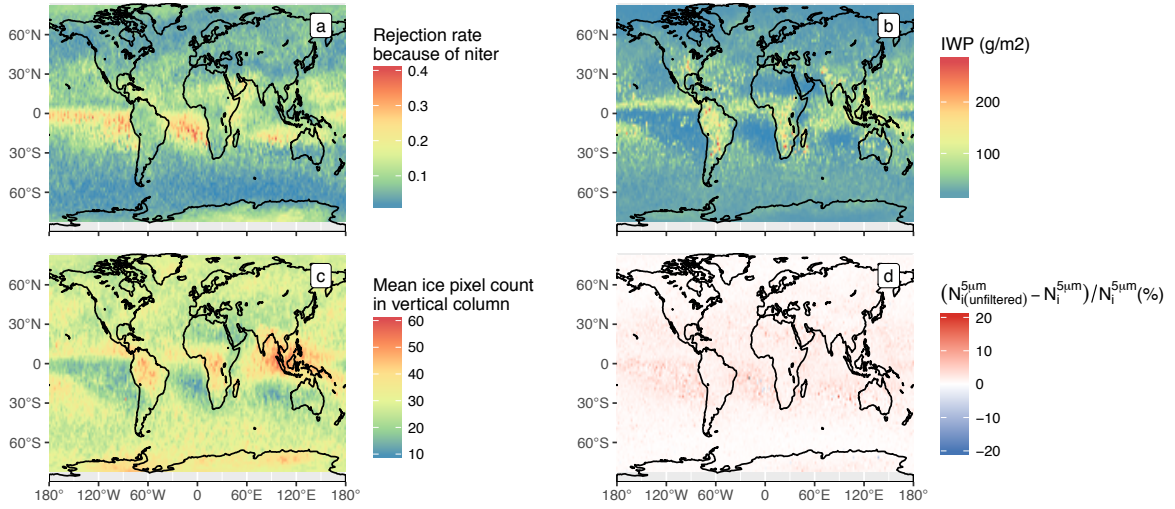


Figure 1: (a) Spatial distribution of the rejection rate associated with the  $n_{\text{iter}} < 2$  filtering for pure ice clouds with  $T_c < -30^\circ\text{C}$ . These results correspond to one year of DARDAR retrievals (2008). (b-c) show the corresponding ice water path (IWP) and average number of ice cloud pixels in the vertical column (we recall that the height of a pixel is 60 m). (d) represents the relative difference on  $N_i^{5\mu\text{m}}$  between  $-60$  and  $-50^\circ\text{C}$  that would be expected if the  $n_{\text{iter}}$  filtering was not applied.)

2. [RC: 2](#)) p 6, l22 it is stated that DARDAR retrievals of pure ice clouds for which the iterative retrieval converged too quickly are ignored. How many of these retrievals are these and can you explain which category of cases these are?

**AR:** We thank the referee for this comment as we had not yet looked into the distributions of rejection rates associated with the filtering based on iteration number. We agree that useful information could be contained there. It is reminded that this filtering is used to avoid pixels associated with a too quick convergence of the forward model with the observations, which could indicate a lack of information and therefore a strong reliance on a priori considerations. This is now further discussed in Appendix A of the revised manuscript.

The spatial distribution of this rejection rate for ice clouds with  $T_c < -30^\circ\text{C}$  is shown in Fig. 1 of this response. A strong latitudinal dependence of the rejection rate is noted, with less than 10% in the mid-latitudes and about 10 to 20% in the tropics. Rejection rates up to 40% are even seen in the north of oceanic subsidence regions of the South hemisphere. A high rejection rate in DARDAR retrievals in the tropics is not surprising as thick clouds with a complex microphysics are likely to be encountered there. However, Fig. 1(b-c) show that the highest rejection rates occur in regions where thin ice clouds with low IWPs are found, most likely retrieved from lidar-only conditions. It could therefore be that, for these thin clouds, a single iteration is sufficient for proper retrievals and we may be over-constraining the dataset filtering. This has never been investigated from DARDAR and would require further analyses to be verified and fully understood. We have nevertheless verified that this filtering actually has a small impact on the overall climatologies. Fig. 1(d) for instance shows the spatial distribution

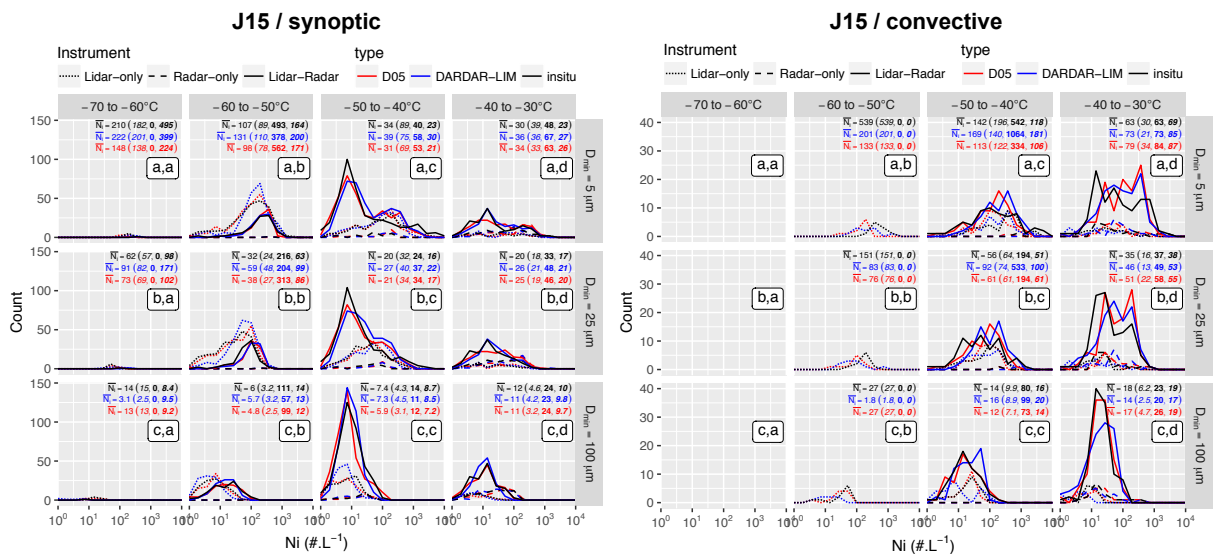


Figure 2: Similar to Fig. 4 of the revised manuscript. The PSDs have here been subsetted following the classification proposed for SPARTICUS by Jackson et al. [2015]. PSDs for synoptic and convective clouds are shown on the left and right panels, respectively.

of relative differences in  $N_i^{5\mu\text{m}}$  (in the  $-60$  to  $-50^\circ\text{C}$  bin) between 1-year climatologies obtained without and with applying the  $n_{\text{iter}}$  filtering. Differences smaller than 10% are typically found in regions where the rejection rate is the most significant. The bias is positive, which seems to indicate that thin cirrus higher  $N_i^{5\mu\text{m}}$  are ignored because of this filtering. It should be noted when comparing these results to Fig. 7(a-c) of the revised manuscript that relatively very low  $N_i^{5\mu\text{m}}$  values are found in regions where this bias is maximum. The  $n_{\text{iter}}$  filtering therefore does not have any significant influence on the results shown in this study. After careful consideration, we have chosen to keep the filtering as but we will keep in mind these analyses and results when producing future versions of the dataset (based on the next version of DARDAR cloud and mask products, which should soon be available). It can also be mentioned that all these filtering options will be provided together with the  $N_i$  dataset, which will hopefully be distributed co-jointly with the publication of this two-part study.

3. **RC:** 3) The evaluation of the prediction of PSD's and  $N_i$  (using all field campaigns) and later for retrieved  $N_i$  (using coincident SPARTICUS measurements) is shown separately for different temperature intervals, which is important as ice crystal particles shapes differ with temperature. It would be very interesting to separate also anvils and synoptic cirrus, as m-D relations might be different. Is there enough statistics of the collocated SPARTICUS campaign measurements to compare  $N_i$  distributions of Fig. 5 for anvils and synoptic cirrus?

**AR:** We thank the referee for this interesting comment. It is a very good point that m-D relations might be different from different cloud types and this could subsequently affect the quality of our evaluation. As mentioned in Sec. 4.1.1, differentiating between different cloud types has not been attempted in this study for reasons of brevity and also because DARDAR does not make any distinction when assuming its PSD shape and m-D relation. It would nevertheless

be interesting, following the referee’s comment, to indeed verify if any specific issue occur when applying a basic differentiation, such as convective vs. synoptic clouds.

To do this, we have associated a cloud type to each PSD from the SPARTICUS dataset used in this study, based on the cloud classifications by Muhlbauer et al. [2014] and Jackson et al. [2015]. Fig. 2 of this response shows comparisons between the histograms of collocated SPARTICUS measurements (Fig. 5 in the original manuscript, Fig. 4 in the revised version) when distinguishing between the “convective” and “synoptic” classification by Jackson et al. [2015]. This classification is chosen here as it is more straightforward. Muhlbauer et al. [2014] offer numerous specific cloud classes, which for this application leads to subsets with a lower statistical significance. It can first be observed in Fig. 2 that convective clouds have higher  $N_i$  means, but are also much less occurrent than synoptic clouds during SPARTICUS. With respect to the quality of DARDAR-LIM retrievals no obvious bias or other issue can be noted in either cloud class. Differences are noted but it remains difficult to estimate if these are within the noise, considering the small number of statistics. Testing the impact of m-D relations would also require to disentangle the impact of a possible misrepresentation of the PSD shape in either of these two cloud classes. Finally, it should be kept in mind that these cloud classification are often very difficult to obtain and can be associated with large uncertainties as well.

For these reasons, and to avoid substantial additional descriptions and discussions in the manuscript, we have still kept analyses based on cloud types out of the revised manuscript. But we recognize the importance of this point and the strong interest to differentiate between cloud types to test the impact of the m-D relation but also the assumptions made on the PSD shape. This will be done in a future study that will focus on improving the PSD representation used for lidar-radar  $N_i$  retrievals.

---

4. RC: 4) section 3.2.2: One specific ice crystal mass-maximum diameter (m-D) relationship is used to determine IWC from the PSD. Indeed, Delanoë et al. 2014 show that the uncertainty to the m-D relationship for the normalized PSD is less important when minimizing using lidar extinction and radar reflectivity. The uncertainty seems to increase if only the lidar extinction is used for the minimization (Fig. 9). As both measurements are complementary, there are clouds for which only the first (thin cirrus) or the latter (towards the base of thick cirrus) are available. We also know that the shape of crystals changes with temperature and Heymsfield et al. 2010 showed that the m-D relation for anvil ice clouds yield masses about a factor of 2 larger than for synoptic ice clouds. Erfani and Mitchell 2016 cite this result in their paper and write that their results showing a similarity in m-D expressions between these two cloud types might be an artefact if the ice particle masses for a given projected area are quite different between these types. The L16 m-D relationship was developed for midlatitude cirrus. So for tropical anvils the computed IWC might be biased. Did you test the IWC computed with the L16 m-D relationship with the measured IWC for tropical anvils (using SPARTICUS and ATTREX) ?

AR: We again thank the referee for this very good point. It is absolutely correct that, as shown by Delanoë et al. [2014] and mentioned by the referee here, uncertainties related to the m-D relation used on the normalized PSD are minimum when both lidar and radar are available. This should lead to smaller uncertainties on lidar-radar  $N_i$  estimates, as now discussed in the appendix of the revised manuscript.

The consequences on  $N_i$  could also be evaluated using the histograms for coincident flights shown in Fig. 2. However, it can be argued that the statistics are for the moment not sufficient

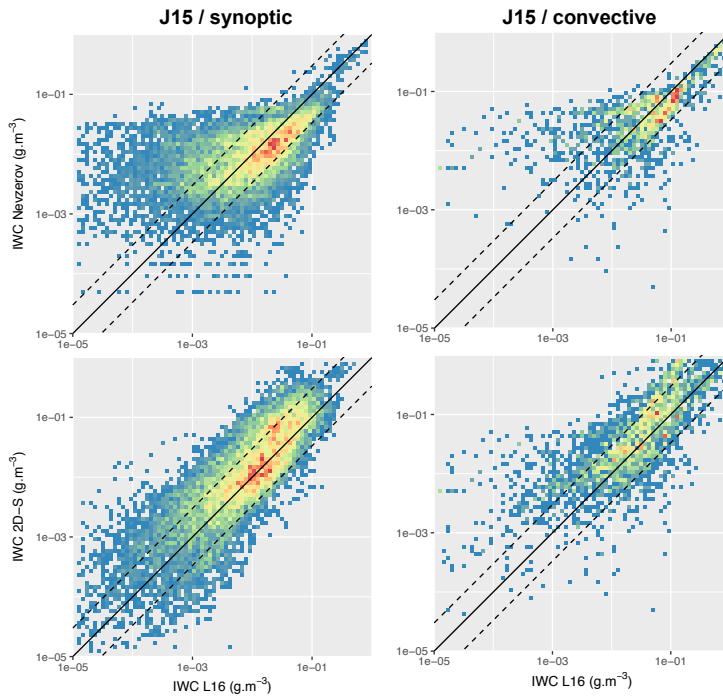


Figure 3: SPARTICUS IWC obtained from Nevzerov (first row) and 2D-S (second row) measurements, as function of L16 predictions based on the 2D-S PSD. The column indicate the cloud category based on Jackson et al. [2015]. A factor of 3 around the one-to-one line is indicated by a dashed line.

to draw any strong conclusions. The impact of m-D assumption will also need to be disentangle from the impact of the PSD shape assumptions, which largely dominate the observed differences. We nevertheless hope to extend this type of evaluation using additional flights coincident with the A-Train, in order to further dig into these issues in the future.

Regarding the use of L16, we have not performed comparison to SPARTICUS or ATTREX measurements in the context of this study, but evaluations of this m-D relation have been made in other studies. Afchine et al. [2018] has for instance shown that this relation should be applicable to tropical clouds, and that the influence of different m-D relations on IWC is small in the temperature range of cirrus. This is now further detailed in Sec. 3.2.2. To provide a more complete response to this comment, we have now analysed the consistency between L16 and SPARTICUS measurements. The classification by Jackson et al. [2015], discussed in the previous response, is used to differentiate between synoptic and convective clouds. IWCs are operationally provided from the 2D-S [based on an assumed area-mass relation; Baker and Lawson, 2006] as well as from bulk measurements from a Nevzerov probe. These comparisons are shown in Fig. 3. It appears that L16 overestimates by a factor of about 2 the IWC measured by the Nevzerov probe. This overestimation seems consistent between synoptic and convective clouds. The 2D-S IWC are in better agreement with L16, for either the synoptic or convective clouds. These results based on SPARTICUS are therefore in agreement with the conclusions by Afchine et al. [2018]. Unfortunately, the ATTREX IWC was not available in the version of the data used for this study and the same analysis could not be repeated. However, it can be noted that Thornberry et al. [2017] showed similarly good agreements between the 2D-S-based IWC and bulk measurements.



---

5. RC: 5) Figs. 6 c and d of the case study present the trajectories as function of UTC. The relevant variable is the time difference which you show in brackets, and then the position on the map in Fig. 6a. If it is not too complicated, it might be clearer to present instead of UTC longitude.

AR: We thank the referee for this comment, adding the spatial coordinates would indeed add clarity to compare Fig. 6(c-d) to Fig. 6a (Fig. 5 in the revised manuscript). We have changed these figures so that the time difference is now used as the reference variable and the corresponding lat-lon coordinates for trajectories A and B are indicated in brackets.

---

6. RC: 6) concerning Fig. 5, is it possible to get also  $D_e$  from DARDAR for this cloud ?

AR: This is a good point, DARDAR  $r_{\text{eff}}$  retrievals are now added in Fig. 6(d) of the revised manuscript and are briefly described in Sec. 5.2.

---

7. RC: 7) The long descriptive text of the case study is sometimes difficult to follow. I suggest for example to move the analysis of the collocated air track comparison (Fig. 8) to a supplement.

AR: We fully agree with this comment, especially considering that the paper already is long and that thorough in situ analyses have extensively been discussed in the previous section. This figure aimed at comforting these results and show that DARDAR-LIM is capable of reproducing the spatial variability of  $N_i$  observed by the 2D-S. Following this comment, it has been moved to supplementary materials (see Fig. S7) and the discussion in Sec. 5.2 has been shortened accordingly.

---

8. RC: 8) I would rename section 6 ‘Presentation of global Ni climatologies’ and 6.1 ‘Geographical distributions’. P2115: ‘considered with caution’ instead of ‘cautiously considered’

AR: We thank the referee for this comment, Sec. 6 has been edited accordingly.

## References:

- A. Afchine, C. Rolf, A. Costa, N. Spelten, M. Riese, B. Buchholz, V. Ebert, R. Heller, S. Kaufmann, A. Minikin, C. Voigt, M. Zöger, J. Smith, P. Lawson, A. Lykov, S. Khaykin, and M. Krämer. Ice particle sampling from aircraft – influence of the probing position on the ice water content. *Atmos. Meas. Tech.*, 11(7):4015–4031, 2018. doi: 10.5194/amt-11-4015-2018.
- B. Baker and R. P. Lawson. Improvement in determination of ice water content from two-dimensional particle imagery. part i: Image-to-mass relationships. *J. Appl. Meteor. and Clim.*, 45(9):1282–1290, 2006. doi: 10.1175/JAM2398.1.
- J. Delanoë, A. J. Heymsfield, A. Protat, A. Bansemer, and R. J. Hogan. Normalized particle size distribution for remote sensing application. *J. Geophys. Res.*, 119(7):4204–4227, 2014. doi: 10.1002/2013JD020700.
- R. C. Jackson, G. M. McFarquhar, A. M. Fridlind, and R. Atlas. The dependence of cirrus gamma size distributions expressed as volumes in  $n_0$ - $\lambda$ - $\mu$  phase space and bulk cloud properties on environmental conditions: Results from the small ice particles in cirrus experiment (sparticus). *Journal of Geophysical Research: Atmospheres*, 120(19):10,351–10,377, 2015. doi: 10.1002/2015JD023492.
- A. Muhlbauer, T. P. Ackerman, J. M. Comstock, G. S. Diskin, S. M. Evans, R. P. Lawson, and R. T. Marchand. Impact of large-scale dynamics on the microphysical properties of midlatitude cirrus. *Journal of Geophysical Research: Atmospheres*, 119(7):3976–3996, 2014. doi: 10.1002/2013JD020035.
- T. D. Thornberry, A. W. Rollins, M. A. Avery, S. Woods, R. P. Lawson, T. V. Bui, and R.-S. Gao. Ice water content-extinction relationships and effective diameter for ttl cirrus derived from in situ measurements during attrex 2014. *J. Geophys. Res. Atmos.*, 122(8):4494–4507, 2017. doi: 10.1002/2016JD025948.

# Ice crystal number concentration estimates from lidar-radar satellite remote sensing. Part 1: Method and evaluation

Odran Sourdeval<sup>1</sup>, Edward Gryspeerd<sup>2</sup>, Martina Krämer<sup>3</sup>, Tom Goren<sup>1</sup>, Julien Delanoë<sup>4</sup>, Armin Afchine<sup>3</sup>, Friederike Hemmer<sup>5</sup>, and Johannes Quaas<sup>1</sup>

<sup>1</sup>Institute for Meteorology, Universität Leipzig, Leipzig, Germany

<sup>2</sup>Space and Atmospheric Physics Group, Imperial College London, London, UK

<sup>3</sup>Forschungszentrum Jülich, Institut für Energie und Klimaforschung (IEK-7), Jülich, Germany

<sup>4</sup>LATMOS/UVSQ/IPSL/CNRS, Guyancourt, France

<sup>5</sup>Laboratoire d'Optique Atmosphérique, Université Lille1, Villeneuve d'Ascq, France

**Correspondence:** Odran Sourdeval (odran.sourdeval@uni-leipzig.de)

**Abstract.** The number concentration of cloud particles is a key quantity for understanding aerosol-cloud interactions and describing clouds in climate and numerical weather prediction models. In contrast with recent advances for liquid clouds, few observational constraints exist on the ice crystal number concentration ( $N_i$ ). This study investigates how combined lidar-radar measurements can be used to provide satellite estimates of  $N_i$ , using a methodology that constrains moments of a parameterized particle size distribution (PSD). The operational liDAR-raDAR (DARDAR) product serves as an existing base for this method, which focuses on ice clouds with temperatures  $T_c < -30^\circ\text{C}$ .

Theoretical considerations demonstrate the capability for accurate retrievals of  $N_i$ , apart from a possible bias in the concentration in small crystals when  $T_c \gtrsim -50^\circ\text{C}$ , due to the assumption of a monomodal PSD shape in the current method. This is verified by comparing satellite estimates to co-incident in situ measurements, which additionally demonstrates the sufficient sensitivity of lidar-radar observations to  $N_i$ . Following these results, satellite estimates of  $N_i$  are evaluated in the context of a case study and a preliminary climatological analysis based on 10 years of global data. Despite of a lack of other large-scale references, this evaluation shows a reasonable physical consistency in  $N_i$  spatial distribution patterns. Notably, increases in  $N_i$  are found towards cold temperatures and, more significantly, in the presence of strong updraughts, such as those related to convective or orographic uplifts. Further evaluation and improvements of this method are necessary but these results already constitute a first encouraging step towards large-scale observational con-

straints for  $N_i$ . Part two of this series uses this new dataset to examine the controls on  $N_i$ .

## 1 Introduction

Clouds play a major role in the climate system and are essential components of the Earth-atmosphere radiation balance (Stephens, 2005). A precise understanding of their properties and processes therefore is necessary to properly address current uncertainties of climate change estimates (Boucher et al., 2013). In particular, the impact of ice clouds on the Earth's radiation budget is recognized as being substantial (e.g. Liou, 1986; Stephens et al., 1990) but still remains difficult to quantify due to the large variability and complexity of their radiative, macro- and micro-physical properties (Zhang et al., 1999; Baran, 2009).

Because of their high spatial and temporal coverage, satellite observations are excellent tools to answer these questions (Lohmann et al., 2007). The A-Train satellite constellation offers a unique synergy between a wide range of active and passive instruments (Stephens et al., 2002), such that numerous methods now exist to provide spaceborne retrievals of ice cloud properties. For instance, bi-spectral approaches based passive visible (Nakajima and King, 1990) or thermal infrared (Inoue, 1985) measurements are often used to directly infer the cloud optical depth ( $\tau_c$ ) and ice crystal effective radius ( $r_{\text{eff}}$ ) (e.g. King et al., 1998; Sourdeval et al., 2013). Direct retrievals of the vertically integrated ice water content (IWC) - the ice water path (IWP) - can

also be obtained from these channels (Sourdeval et al., 2015) (Guignard et al., 2012; Sourdeval et al., 2015), passive microwave sensors (Gong and Wu, 2014), or a synergy of both (Holl et al., 2014). Vertical profiles of the cloud visible extinction ( $\alpha_{\text{ext}}$ ), IWC and ice crystal  $r_{\text{eff}}$  are commonly provided using lidar and/or radar measurements (e.g. Vaughan et al., 2009; Austin et al., 2009; Delanoë and Hogan, 2010). However, only few developments have to date focused on the ice crystal number concentration ( $N_i$ ).

A lack of  $N_i$  retrievals from satellite contrasts with the importance of this quantity for understanding and describing ice cloud processes (Comstock et al., 2008). Along with the mass concentration, the number concentration is often used as a prognostic variable in two-moment bulk microphysics schemes that predict the evolution of clouds in recent climate and numerical weather prediction models (Khain et al., 2000; Seifert and Beheng, 2006). An absence of global observational constraints therefore limits the evaluation of model predictions to sparser in situ measurements (e.g. Jensen et al., 1994; Zhang et al., 2013; Farrington et al., 2016). Moreover,  $N_i$  appears as a particularly useful metric to quantify aerosol-cloud interactions due its potentially close link with the aerosol concentration (Kärcher and Ström, 2003; Kay and Wood, 2008; Hendricks et al., 2011). Consequently, while numerous studies have for these reasons used satellite estimates of the cloud droplet number concentration ( $N_d$ ) to evaluate the indirect aerosol radiative forcing (Boers et al., 2006; Quaas et al., 2006, 2008; Gryspeerd et al., 2016), the contribution of ice clouds to this effect remains largely unknown (Heyn et al., 2017).

One reason for this absence of a global  $N_i$  dataset lies in the difficulty to directly link this quantity to other commonly retrieved cloud properties. For liquid clouds,  $N_d$  can for instance be inferred through relationships between satellite retrievals of  $\tau_c$  and the droplet  $r_{\text{eff}}$  (Brenquier et al., 2000) (Han et al., 1998; Brenquier et al., 2000). These relationships rely on strong assumptions that have shortcomings (Grosvenor et al., 2018) but nonetheless provide  $N_d$  values that compare well against in situ observations (Painemal and Zuidema, 2011) and can be used to establish climatologies (Bennartz and Rausch, 2017) and study aerosol-cloud interactions (Han et al., 2002; Quaas et al., 2008). Such relationships are less trivial for ice clouds due to the high complexity and variability of ice nucleation processes (Kärcher and Lohmann, 2002, 2003; Ickes et al., 2015). Recent attempts have been made, e.g. by Mitchell et al. (2016) Mitchell et al. (2016, 2018) who linked (providing additional lidar information) the absorption  $\tau_c$  and ice crystal  $r_{\text{eff}}$  to  $N_i$  for thin single-layer ice clouds, but rigorous validation remains necessary.

An alternative approach to estimate  $N_i$  has arisen with the emergence of retrieval methods aiming at directly constraining parameters of particle size distributions (PSDs) from remote sensing observations. Indeed, provided that a PSD is properly estimated, the corresponding number concentration

(the zeroth moment of the PSD, or  $\mathcal{M}_0$ ) can be extracted. Important developments on applying these methods to satellite observations can be attributed to Austin and Stephens (2001) who, through an elaborate variational scheme, used the sensitivity of radar reflectivity ( $Z_e$ ) and  $\tau_c$  to other moments, namely  $\mathcal{M}_6$  and  $\mathcal{M}_2$ , respectively, to constrain PSD shape parameters. This method, initially dedicated to liquid clouds, allowed retrieving profiles of droplet geometric mean radius and a vertically homogeneous  $N_d$ . This work was later extended to ice clouds by Benedetti et al. (2003) and further improved by Austin et al. (2009) to perform retrievals of  $N_i$  profiles using better *a priori* assumptions. These developments are now implemented in the operational CloudSat 2B-CWC-RO product, which has extensively been used to study the IWC (e.g. Wu et al., 2009; Waliser et al., 2009; Eliasson et al., 2011) but its  $N_i$  product remains to be thoroughly evaluated. Notably, Protat et al. (2010) highlighted through comparisons to ground-based lidar-radar cloud products the need to improve these  $N_i$  retrievals prior to quantitative use. The authors argued that radar-only methods lack sensitivity to  $N_i$  profiles due to the dominant contribution of small ice particles to the total number concentration, whereas the combined use of a lidar extinction backscatter coefficient ( $\beta_{\text{ext}}$ ) would help to further constrain the amount of small particles. However, no operational estimation of  $N_i$  from satellite lidar-radar observations has to date been attempted.

Based on these early developments, this study aims at investigating the capabilities of lidar-radar methods to estimate  $N_i$  by producing and evaluating a new dataset based on the operational liDAR-raDAR (DARDAR, Delanoë and Hogan, 2010) product. DARDAR retrieves profiles of ice cloud properties by combining measurements from the CloudSat Cloud Profiling Radar (CPR) and the Cloud-Aerosol Lidar with Orthogonal Polarization (CALIOP). Although DARDAR does not operationally provide  $N_i$ , and has not been tested for this purpose, its retrieval framework that aims at constraining parameters of a PSD parameterization (Delanoë et al., 2005, hereinafter D05) makes it ~~an~~ a suitable candidate to estimate this quantity. Nevertheless, a careful evaluation remains necessary to determine if the D05 parameterization is theoretically capable of predicting  $N_i$  and if lidar-radar lidar and/or radar measurements can provide sufficient information to properly constrain it. Therefore, a threefold evaluation is performed here to investigate the quality of these lidar-radar  $N_i$  estimates based on comparisons to in situ observations, a case study and a brief climatological analysis.

The paper is structured as follow: Section 2 presents the methodology used here to estimate  $N_i$  from current DARDAR products. Sec. 3 describes the data utilized in this study. The ability of DARDAR to retrieve in situ measurements of  $N_i$  is investigated in Sec. 4. Then, Sec. 5 discusses the vertical structure of  $N_i$  estimates along a short orbit and Sec. 6 proposes a brief analysis of  $N_i$  climatologies. Finally, Sec. 7 concludes this study. Algorithmic limitations and uncertainties are discussed in an Appendix. The second part of this series

(Gryspeerdt et al., 2018b) will use this new dataset to investigate the processes controlling  $N_i$ .

## 2 Methodology

### 2.1 The DARDAR product

For brevity reasons, this section only provides an introduction to the DARDAR product; the reader is invited to refer to Delanoë and Hogan (2008, 2010) for a thorough description of the retrieval method.

DARDAR (currently v2.1.1) uses a variational framework to merge information from and  $Z_e$  profiles in order to retrieve vertical structures of ice cloud and of a parameter noted  $N_0^*$ . These two parameters, which are closely linked to a PSD parameterization (see Sec. 2.1), are subsequently combined to infer profiles of IWC and ice crystal  $r_{\text{eff}}$ . The lidar and radar measurements are provided by CALIOP and CPR, respectively, which implies that DARDAR retrieves cloud properties with a vertical resolution of 60 m along the CloudSat footprint (about 1.7 km of horizontal resolution). It is worth noting that the simultaneous use of lidar and radar information allows this method to be sensitive to thick and thin ice clouds, with IWP's spanning from about  $0.01 \text{ g}\cdot\text{m}^{-2}$  to  $5 \text{ kg}\cdot\text{m}^{-2}$  (Sourdeval et al., 2016). The position and thermodynamic phase of cloud layers (DARDAR mask, v1.1.4; e.g. Ceccaldi et al., 2013) are determined, prior to the retrieval process, using these measurements and reanalyses from the European Centre for Medium-Range Weather Forecasts (ECMWF).

DARDAR has already been extensively used for improving our understanding of clouds and precipitation (e.g. Battaglia and Delanoë, 2013; Protat et al., 2014; Feofilov et al., 2015; Mascia et al., 2016). Its operational retrievals have also been evaluated against products from a similar lidar-radar method (CloudSat 2C-ICE; Deng et al., 2010) and in situ observations. Deng et al. (2012) found good agreements between the retrievals of the IWC,  $r_{\text{eff}}$  and  $\alpha_v$  from both methods, which also compared well against co-incident in situ observations, despite a small overestimation noted for IWCs retrieved by DARDAR in lidar-only conditions.

### 2.1 Representation of the size distribution

$N_i$  can be expressed as the integral of a given ice particle size distribution  $N(D)$ ,

$$N_i = \mathcal{M}_0 = \int_0^{\infty} N(D) dD, \quad (1)$$

with  $D$  the particle dimension (hereinafter the maximum diameter). Hence,  $N_i$  corresponds to the moment zero of the PSD, noted  $\mathcal{M}_0$ . Other moments also relate to various cloud properties (e.g. to the IWC, through mass-dimension rela-

tions, or to  $D_{\text{eff}} = \mathcal{M}_3/\mathcal{M}_2$ ) and to remote sensing measurements (e.g.  $\beta_{\text{ext}}$  relates to  $\mathcal{M}_2$  and  $Z_e$  to  $\mathcal{M}_6$ ), demonstrating that PSDs act as crucial links between physical parameters and observations. However, although the lidar extinction  $\beta_{\text{ext}}$  and the radar reflectivity  $Z_e$  are sensitive to particle sizes, they each provide information on a single moment of the PSD. Therefore and so, assuming a pair of single-wavelength measurements, their combination is not sufficient to fully constrain every aspect of a complex PSD; simplifications are necessary.

Parameterizing PSDs is a challenging task due to the large variability of their shapes on a global scale or even within a cloud layer (e.g. Mitchell et al., 2011; Krämer et al., 2016). Nevertheless, D05 and Field et al. (2005) showed that two-moment normalization methods can be used to reasonably approximate a wide range of measured size distributions to a single shape function, noted  $F$ , referred to as a “universal” or “normalized” PSD. By normalization it is meant that the dimension and concentration axes are carefully scaled in order to make  $F$  independent of parameters that strongly influence the shape of the original PSD.

In the framework by This study will focus on the D05 parameterization, which is implemented in DARDAR used in DARDAR (see Sec. 3.1) to relate lidar/radar measurements to ice cloud properties. In D05, a normalization factor noted  $N_0^*$  and the ice crystal mean volume-weighted diameter  $D_m$  (defined as the ratio of  $\mathcal{M}_4$  to  $\mathcal{M}_3$ ) serve as scaling parameters to the concentration and dimension axes, respectively. The normalization process can thus then be summarized as

$$F(D_{\text{eq}}/D_m) = N(D_{\text{eq}})/N_0^*, \quad (2)$$

where  $D_m$  and  $N_0^*$  are in D05 specifically set to make  $F$  independent of the IWC and  $D_m$  of the original PSD (i.e. they become constant after normalization). The ice crystal size is represented by the equivalent-melted diameter,  $D_{\text{eq}}$ , which relates to  $D$  through

$$D_{\text{eq}} = \left[ \frac{6m(D)}{\pi\rho_w} \right]^{\frac{1}{3}}, \quad (3)$$

where  $\rho_w = 1000 \text{ kg m}^{-3}$  is the density of liquid water and  $m(D)$  is a given mass-dimension (m-D) relationship. In DARDAR, the latter follows empirical DARDAR uses the empirical m-D formulas by Brown and Francis (1995) when  $D > 300 \mu\text{m}$  and by Mitchell (1996) otherwise. D05 demonstrated with in situ measurements that this approach allows the accurate prediction of  $\mathcal{M}_2$  and  $\mathcal{M}_6$ . Inversely,  $\beta_{\text{ext}}$  and  $Z_e$  can be used to constrain these moments, infer the associated scaling parameters and reproduce the original PSD using Eq. (2). Regarding the shape of  $N(D_{\text{eq}})$ ,

D05 further concluded that a four-parameter gamma-modified distribution,

$$N(D_{\text{eq}}) = N_0 D_{\text{eq}}^{\alpha} \exp\{-k D_{\text{eq}}^{\beta}\}, \quad (4)$$

allows the parameterization to properly fit in situ measurements from mid-latitude and tropical regions. In DARDAR,  $\alpha$  and  $\beta$  are two fixed parameters that were adjusted-chosen to best fit these measurements ( $\alpha = -1$  and  $\beta = 3$ ). On the contrary, whereas  $N_0$  and  $k$  vary-are iteratively adjusted during the retrieval process, where they are iteratively adjusted to fit observational constraints through their relations to the scaling parameters, as shown in Sec. 2.2.

## 2.2 Extracting $N_i$ from DARDAR

Considering the gamma-modified function of in Eq. (4) to describe the shape of  $N(D)$  in Eq. (1), and because the total number of particles is independent of the choice of a dimensional variable,  $N_i$  in DARDAR corresponds to

$$N_i = \int_0^{+\infty} N_0 D_{\text{eq}}^\alpha \exp\{-k D_{\text{eq}}^\beta\} dD_{\text{eq}}. \quad (5)$$

Because  $\alpha$  and  $\beta$  are fixed,  $N_i$  can be obtained-computed given a knowledge of  $N_0$  and  $k$ . These two parameters are not part of the operational products but can be deduced from their link to other retrieved properties. This section shows how  $N_i$ . It is here demonstrated how retrievals of IWC and  $N_0^*$  can be inferred from IWC and  $N_0^*$ , which are both operationally provided. It should be kept in mind that a used to determine  $D_m$ , deduce  $N_0$  and  $k$ , and subsequently estimate  $N_i$ . A strict consistency with the current version of the algorithm must be DARDAR is respected to ensure that  $N_i$  estimates are meaningful; possible improvements, such as proposed by Delanoë et al. (2014) Delanoë et al. (2014, hereinafter D14) for future DARDAR versions, are not included at this stage.

As mentioned in Sec. 2.1, the scaling parameters  $N_0^*$  and  $D_m$  are defined so that  $N(D_{\text{eq}})$  becomes independent of IWC and  $D_m$  after normalization. Using the definition of  $N(D_{\text{eq}})$  from Eq. (2) to rewrite  $D_m = \mathcal{M}_4 / \mathcal{M}_3$ , the latter condition leads to  $\mathcal{M}_4^F = \mathcal{M}_3^F$ , with  $\mathcal{M}_n^F$  the  $n^{\text{th}}$  moment of the normalized PSD  $F(D_{\text{eq}}/D_m)$ . Subsequently,  $\mathcal{M}_3^F$  and  $\mathcal{M}_4^F$  must be equal to an arbitrary constant, which was set by D05 to  $\Gamma(4)/4^4$ . By inserting Eq. (4) into Eq. (2), and after simplification of the definite integral,  $\mathcal{M}_n^F$  becomes

$$\mathcal{M}_n^F = \frac{1}{\beta} \Gamma\left(\frac{\alpha + n + 1}{\beta}\right) \frac{N_0}{N_0^*} D_m^{-(n+1)} k^{-\frac{\alpha+n+1}{\beta}}. \quad (6)$$

Based on this equation, the conditions  $\mathcal{M}_4^F = \mathcal{M}_3^F$  and  $\mathcal{M}_3^F = \Gamma(4)/4^4$  lead to two unique relationships between the PSD parameters  $k$  and  $N_0$  and the scaling parameters variables  $N_0^*$  and  $D_m$ :

$$k = \left[ \frac{1}{D_m} \frac{\Gamma\left(\frac{\alpha+5}{\beta}\right)}{\Gamma\left(\frac{\alpha+4}{\beta}\right)} \right]^\beta \quad (7)$$

and

$$N_0 = N_0^* D_m^{-\alpha} \frac{\Gamma(4)}{4^4} \beta \frac{\Gamma\left(\frac{\alpha+5}{\beta}\right)^{\alpha+4}}{\Gamma\left(\frac{\alpha+4}{\beta}\right)^{\alpha+5}}. \quad (8)$$

respectively. Hence, providing  $N_0^*$  and  $D_m$ , Eq. (7) and (8) can be inserted into Eq. (5) to compute  $N_i$ .

The scaling parameter  $N_0^*$  is provided in DARDAR, whereas  $D_m$  can be deduced from other cloud properties. The IWC, which by definition equals For instance, considering that  $\text{IWC} = \frac{\pi \rho_w}{6} \mathcal{M}_3$  for equivalent-melted spheres, can be related to  $N_0^*$  and  $D_m$ . By and by using Eq. (2) to demonstrated-demonstrate that  $\mathcal{M}_3 = N_0^* D_m^4 \mathcal{M}_3^F$  and, because  $\mathcal{M}_3^F = \Gamma(4)/4^4$ ,  $D_m$  can be inferred from relates to IWC and  $N_0^*$  following

$$D_m = 4 \left[ \frac{1}{\pi \rho_w} \frac{\text{IWC}}{N_0^*} \right]^{\frac{1}{4}}. \quad (9)$$

## 3 Data description

### 3.1 Satellite retrievals

DARDAR Global DARDAR retrievals of IWC and  $N_0^*$  retrievals from 2006 are used to 2016 are used here to compute a 10-year  $N_i$  dataset based on compute  $N_i$  following the methodology described in Sec. 2. It This section only provides a brief introduction to this algorithm; the reader is invited to refer to Delanoë and Hogan (2008, 2010) for further details.

DARDAR (currently v2.1.1) uses a variational method that merges measurements from CALIOP ( $\beta_{\text{ext}}$ ) and CPR ( $Z_e$ ) to constrain the scaling parameters of D05 and infer profiles of various ice cloud properties such as  $\alpha_{\text{ext}}$ , IWC and  $r_{\text{eff}}$ . DARDAR retrievals are provided with a vertical resolution of 60 m along the CloudSat footprint (about 1.7 km of horizontal resolution), i.e. globally with equator crossings around 1:30 am/pm local time.

The position and thermodynamic phase of cloud layers are determined prior to the retrieval process (Ceccaldi et al., 2013) by merging satellite observations with reanalyses from the European Centre for Medium-Range Weather Forecasts (ECMWF). To avoid possibly strong uncertainties in retrievals of the cloud phase and/or properties, only purely ice clouds that are not situated below supercooled or liquid layers are considered in this study (i.e. layers identified as supercooled or mixed-phase are ignored).

DARDAR has extensively been used for improving our understanding of clouds and precipitations (e.g. Battaglia and Delanoë, 2013; Protat et al., 2014; Feofilov et al., 2014). It has also been evaluated against products from a similar lidar-radar method (Deng et al., 2010) and in situ observations. Notably, Deng et al. (2012) found good



agreements between the retrievals of IWC,  $r_{\text{eff}}$  and  $\alpha_{\text{ext}}$  from both methods, which also compared well against co-incident in situ observations, despite a small overestimation noted for IWCs retrieved by DARDAR in lidar-only conditions.

DARDAR retrievals from 2006 to 2016 are here used to produce a 10-year  $N_i$  dataset. It can be noted that the DARDAR products are not continuously available throughout this period due to gaps in the CloudSat measurements but such discontinuities should. Such discontinuities should however not affect the following conclusions as precise analyses of  $N_i$  patterns (e.g. trends or diurnal cycles) are not intended in this study. To avoid possible confusion with the operational product, the research-level  $N_i$  dataset obtained here will be referred to as DARDAR-LIM (DARDAR - Leipzig Institute for Meteorology).

In order to limit erroneous retrievals, two filters were applied to DARDAR-LIM. First,  $N_i$  is only computed for purely ice clouds that are not situated below supercooled or liquid layers (i.e. layers identified as supercooled or mixed-phase by the DARDAR mask are ignored). This condition is required to avoid possibly strong uncertainties in retrievals of the cloud phase and/or properties. Then, pixels where DARDAR converged too quickly, i.e. with a number of iterations  $n_{\text{iter}} \leq 2$ , are ignored in order to limit any strong influence of It can be noted that, as any retrieval algorithm, DARDAR depends on assumptions made on non-retrieved parameters used in its forward model to simulate lidar and radar measurements. Furthermore, additional hypotheses are needed in the absence of information from one instrument, as discussed in Sec. A1. Thanks to its use of a statistical approach, DARDAR is able to rigorously propagate assumed errors on non-retrieved forward model parameters or any other a priori assumptions on the retrieved cloud properties.

It should be mentioned that DARDAR provides uncertainties associated with its retrievals, obtained by the propagation of errors related to the measurements and non-retrieved forward model parameters its retrievals. A propagation of the errors attached to IWC and  $N_i^*$  on  $N_i$  shows relative uncertainties from about 20 to 50% on this parameter (see Sec. A2). Expectedly, these uncertainties are the lowest when lidar and radar measurements are together available. However, no transcriptions into errors on these numbers do not provide a complete estimation of the accuracy of  $N_i$  are shown in this study as they are unlikely to be meaningful for this quantity. Indeed, no uncertainty is associated with as DARDAR does not rigorously account for uncertainties related to assumptions on the PSD shape, whose representation of the small ice crystal distribution is crucial to  $N_i$ . Instead, an estimation of. A preliminary sensitivity study showed that strong deviations from the assumed  $\alpha$  and  $\beta$  parameters could reasonably lead to errors up to 50% on  $N_i$  (see Sec. A3). The overall uncertainties on  $N_i$  due to instrumental sensitivity and physical assumptions is therefore difficult to quantify based on DARDAR products alone. This study instead aims at evaluating the quality of

the DARDAR-LIM dataset will be reached these satellite  $N_i$  estimates through comparisons to in situ measurements.

### 3.2 In situ measurements

In situ PSD measurements from mid-latitude and tropical ice clouds are required to evaluate the satellite estimates of  $N_i$ . This evaluation must determine if (i) the PSD parameterization used in DARDAR (i.e. D05) is capable of predicting  $\mathcal{M}_0$ , and (ii) there is enough sensitivity in lidar-radar measurements to properly constrain  $N_i$ . A few conditions are thus set for this evaluation. To answer (i), it is preferable that the measurements used in this evaluation are independent of the ones utilized by D05 to build the PSD parameterization. Answering (ii) additionally requires measurements from flights that are coincident with the CloudSat overpass. Finally, (i) and (ii) require usable measurements of the concentration in small ice crystals (i.e.  $D < 100 \mu\text{m}$ ), which highly contribute to  $N_i$ . This implies that possible phenomena of ice crystal shattering on the probe tips and inlets (Korolev et al., 2011, 2013) must be accounted for to a reasonable extent, through combined specific instrumental design and post-processing (Field et al., 2006; Korolev and Field, 2015).

#### 3.2.1 Airborne instruments and campaigns

Measurements from five recent airborne campaigns are used during this evaluation process. Three campaigns are described in the ‘Cirrus Guide Part I’ by Krämer et al. (2016), namely COALESC 2011 (Combined Observation of the Atmospheric boundary Layer to study the Evolution of Strato-Cumulus; Osborne et al., 2014), ML-CIRRUS 2014 (Mid-Latitude CIRRUS; Voigt et al., 2016) ACRIDICON-CHUVA 2014 (Aerosol, Cloud, Precipitation, and Radiation Interactions and Dynamics of Convective Cloud Systems; Wendisch et al., 2016). Another two campaigns took place over the US and tropical Pacific: SPARTICUS 2010 (Small PARTICle In Cirrus; Mace et al., 2009) (Small PARTICles In Cirrus; Mace et al., 2009) and AT-TREX 2014 (Airborne Tropical Tropopause EXperiment-2014; Jensen et al., 2015). A detailed description of these field campaigns and of their involved instrumentation can be found in the above-mentioned references and is therefore not repeated here. However, a brief summary of the information relevant to this evaluation is provided below and in Table 1.

The COALESC campaign involved 16 flights performed by the BAe-146 aircraft of the Facility for Airborne Atmospheric Measurements over the South-East coast of England and Wales, during February and March 2011. Despite that the main objectives of COALESC focused on stratocumulus clouds, numerous flights also involved direct measurements of PSDs within mixed-phase and cirrus clouds. The instrumentation for cloud particle measurements notably involved the NIXE-CAPS (Novel Ice Experiment - Cloud-Aerosol Spectrometer) (Meyer, 2012; Luebke et al., 2016), which



**Table 1.** Description of the in situ campaigns. The numbers correspond to PSDs averaged ~~into~~over 10-s periods and for ice clouds with  $T_c < -30^\circ\text{C}$ .

Campaign	Instrument(s)	$\overline{TAS}$	#PSDs / Eq. sampling time
COALESC 2011	NIXE-CAPS	168 m.s <sup>-1</sup>	3459 / 9.6 h
ML-CIRRUS 2014	NIXE-CAPS	207 m.s <sup>-1</sup>	5954 / 16.5 h
ACRIDICON-CHUVA 2014	NIXE-CAPS	209 m.s <sup>-1</sup>	4166 / 11.6 h
SPARTICUS 2010	2D-S	174 m.s <sup>-1</sup>	<del>15090</del> <u>13121</u> / <del>41.936</del> <u>4</u> h
ATTREX 2014	FCDP / 2D-S	157 m.s <sup>-1</sup>	11465 / 31.8 h

provides distributions of the number concentration of particles with sizes from 0.6 to 937  $\mu\text{m}$ . This instrument consists of a combination of the CAS-DPol probe for particles smaller than 50  $\mu\text{m}$  and the Cloud Imaging Probe (CIPg) for particles larger than 15  $\mu\text{m}$ . The in-cloud PSDs are combined from CAS-Dpol (3.0 to 20  $\mu\text{m}$ ) and CIPg (> 20  $\mu\text{m}$ ). It should be noted that the NIXE-CAPS inlets have been designed to limit the occurrence of shattering effects, which are further reduced through the use of post-processing by inter-arrival time algorithms. Flight details and additional information regarding the NIXE-CAPS instrument and its uncertainties are provided in Costa et al. (2017) and Meyer (2012), respectively.

ML-CIRRUS took place in March and April 2014 over Europe and the North Atlantic. This campaign aimed at investigating nucleation and life cycle processes in cirrus, as well as their impact on climate. The High Altitude and Long range (HALO) aircraft flew a total of 16 flights, including 40 h dedicated to the remote sensing or in situ measurement of cirrus. Similar to COALESC, cloud particle measurements were performed by the NIXE-CAPS probe. The reader can refer to Luebke et al. (2016) for further details on these measurements during ML-CIRRUS.

ACRIDICON-CHUVA took place in September 2014 over the Amazonian forest with the primary goal to study the role of anthropogenic aerosols on the life cycle of deep convective clouds and precipitation. This campaign involved the HALO aircraft, which performed 13 research flights for a total of 96 h. The cloud particle measurements were performed by the NIXE-CAPS probe. The algorithms to remove shattered ice fragments were not automatically applied to avoid possible erroneous removal of small droplets in warm and mixed-phase clouds. However, applying the inter-arrival time algorithms generally only negligibly change the cirrus ice particle concentrations, since in cold cirrus the crystals in most cases does not grow to sizes that are subject to shattering. Further details on the use of NIXE-CAPS during ACRIDICON-CHUVA can be found in Costa et al. (2017).

The ATTREX-2014 mission took place between February and March 2014 over the West tropical Pacific. Six flights were performed by the NASA Global Hawk aircraft, for a total of 34 h of measurements inside cirrus

within the tropical tropopause layer (TTL, i.e. from an altitude of about 14 to 19 km). ~~During this campaign, PSD measurements were obtained from Concentrations in small- to moderate-size particles were measured by two instruments;~~ a Two-Dimension Stereo (2D-S) probe (Lawson et al., 2006) for particle sizes between 5 and ~~3205~~1280  $\mu\text{m}$  (~~extended to 3205  $\mu\text{m}$  using the time dimension~~) with a maximal bin resolution of 10  $\mu\text{m}$  ~~and by~~, and a Fast Cloud Droplet Probe (FCDP) for sizes from 1 to 50  $\mu\text{m}$ . ~~Different processing methods, noted  $M_i$ , are available to determine particle concentrations and sizes from the 2D-S (Lawson, 2011). PSDs used here have been processed with  $M_1$  or  $M_7$  when available. Erfani and Mitchell (2016) have shown no significant differences in the concentration of small particles from these two methods.~~ The 2D-S was specifically developed to limit ice shattering through probe inlet design and is combined with a post-processing treatment based on an inter-arrival time algorithm (Lawson, 2011). ~~However, it should be noted that concentrations measured in its first 2 bins (i.e., for particles smaller than 25  $\mu\text{m}$ ) may suffer from large uncertainties (Jensen et al., 2013b; Gurganus and Lawson, 2018), which must be considered when selecting a minimal size threshold for computing  $N_i$  (see Sec. 3.3).~~ The FCDP also is considered to be efficient at removing shattered particles (McFarquhar et al., 2007). These two instruments are therefore combined here to improve the description of small particles in PSD measurements. The FCDP is used to provide the concentration of particles from 3 to 24  $\mu\text{m}$  (i.e. 10 bins) and the 2D-S is used from 25 (i.e. its 3rd bin) to 3205  $\mu\text{m}$ . The 1  $\mu\text{m}$  gap is accounted for by scaling the concentration of the last FCDP bin. More information on 2DS and FCDP measurements during ATTREX-2014 can be found in Thornberry et al. (2017).

SPARTICUS was operated as part of the Atmospheric Measurement and Radiation (ARM) aerial program (Schmid et al., 2013) to reach a better understanding of small ice particles in clouds. This mission took place between January and June 2010 over Central USA and involved a Learjet-25 aircraft that performed 200 h of scientific flights in synoptic and convective ice clouds. Its instrumentation involved the 2D-S probe for particle size measurement. A Forward Scatter-

ing Spectrometer Probe (FSSP) was also available during the campaign but its measurements are not included here due to likely contamination by shattering (Field et al., 2003; McFarquhar et al., 2007; Jackson et al., 2015). The SPARTICUS data used here was treated with a combination of the  $M_1$  method for  $D > 365 \mu\text{m}$  and  $M_4$  otherwise (Lawson, 2011), which allows for a more accurate treatment of out-of-focus particles (Korolev, 2007). An advantage of SPARTICUS for this study is that it contains numerous coincident flights with the A-Train, as detailed in Deng et al. (2012).

### 3.2.2 Data processing

In order to ensure an optimal consistency between the PSD measurements from each airborne campaign, an identical post-processing procedure has been followed to treat 1-Hz measurements from the 2DS, FCDP-2DS and NIXE-CAPS. This section discusses the most important details regarding the treatment of these measurements.

First, the 1-Hz measurements have been averaged into over 10-s period-periods to improve the statistical reliability of cloud sampling by in situ probes. This averaging also allows for a better comparability with cloud volumes sampled by CloudSat (and therefore DARDAR products), which has an along- and across-track horizontal resolution of 1.7 and 1.4 km, respectively. Considering the average true air speeds (TAS) for each campaign (see Table 1), 10-s PSDs are representative of flight legs from about 1.6 to 2.1 km.

Furthermore, to avoid possible ambiguities and uncertainties related to satellite retrievals and in situ measurements in mixed-phase clouds, this study focuses purely ice clouds, i.e. with a temperature  $T_c < -40^\circ\text{C}$ . However, to allow for additional flexibility in the evaluation, all in situ measurements obtained when  $T_c < -30^\circ\text{C}$  are considered. Possible contamination by liquid drops are expected to be negligible at these temperatures (Costa et al., 2017).

Finally, the IWC corresponding to each in situ PSD is required to obtain predictions by D05. Bulk measurements are available for SPARTICUS and ATTREX but the bulk IWC was not measured for ACRIDICON-CHUVA, COALESC and ML-CIRRUS. Alternatively, and consistently with Krämer et al. (2016), the m-D relation by Luebke et al. (2016), noted  $m_{L16}(D)$ , can instead be utilized to estimate IWCs from the NIXE-CAPS PSD measurements.  $m_{L16}(D)$  is based on a m-D relation by Mitchell et al. (2010), which was slightly modified to improve the representativeness of the mass concentration for small ice crystals. The validity of this type of approach, and of  $m_{L16}(D)$  in particular, was recently consolidated by Erfani and Mitchell (2016) and Afchine et al. (2018), who demonstrated their accuracy and generalizability for all types of ice clouds from  $T_c < -20^\circ\text{C}$ . Because Afchine et al. (2018) has in particular shown that this relation should be applicable to tropical clouds and that the influence of different m-D relations on IWC is small in the temperature range of cirrus. Considering this, and

because Mitchell et al. (2010) and Erfani and Mitchell (2016) developed and tested their m-D relation using 2D-S measurements from tropical and mid-latitude campaigns (including SPARTICUS),  $m_{L16}(D)$  should as well be applicable to SPARTICUS and ATTREX2014. Therefore, for the sake of consistency,  $m_{L16}(D)$  is here utilized to estimate the IWC for all campaigns. The uncertainties arising from using a m-D relation are discussed in Erfani and Mitchell (2016) and appear reasonable in the context of this evaluation due to the relatively small sensitivity of D05 predictions to IWC, as discussed in Sec. 4.1.

Overall, more than about 40 000 10-s PSDs, or 110 106 h of equivalent cloud sampling, are used for the evaluation presented in this study. These numbers are summarized in Table 1 and the distribution of temperatures sampled during each campaign is indicated in Fig. S1 of the supplementary materials.

### 3.3 Discussion on the Choice of a minimum integration threshold size

To ensure a consistency with DARDAR when inferring  $N_i$  from Eq. (5), the PSD parameters  $\alpha$  and  $\beta$  are set to -1 and 3, respectively. However,  $\alpha = -1$  implies a discontinuity in  $N(D_{\text{eq}})$  when the diameter equals zero. An analytic solution for  $N_i$  can therefore only be obtained by considering a minimum diameter,  $D_{\text{min}}$ , for the integral. This threshold must here be chosen within the validity range of the in situ measurements used for the evaluation.

As mentioned in Sec. 3.2.1, the 2DS, FCDP and NIXE-CAPS have a different sensitivity to small particles. The former instrument measures ice crystals with sizes down to about  $5 \mu\text{m}$ , whereas the two latter can detect particles down to  $1 \mu\text{m}$ . For consistency reasons, and to avoid possible contamination by aerosols, only ice crystal-crystals larger than  $5 \mu\text{m}$  will here be considered when computing  $N_i$  from each probe. The same threshold is thus applied when computing  $N_i$  from DARDAR.

The and the following results will therefore mostly focus on the concentration-focus on concentrations in crystals larger than  $D_{\text{min}} = 5 \mu\text{m}$ , noted  $N_i^{5 \mu\text{m}}$ . Nevertheless, the concentration in-

In situ measurements of  $N_i^{5 \mu\text{m}}$  can still be associated with large uncertainties that are difficult to quantify. In particular, measurements from the first two size bins of the 2D-S (5 to  $25 \mu\text{m}$ ) are known to suffer from uncertainties due to the instrumental response time and depth-of-field (Jensen et al., 2013b; Gurganus and Lawson, 2018). Also, despite being minimized, a contamination by ice shattering events cannot be excluded. These effects are typically associated with an overestimation of  $N_i^{5 \mu\text{m}}$ . Therefore, the concentration of particles larger than 25 and  $100 \mu\text{m}$ , respectively noted  $(N_i^{25 \mu\text{m}}$  and  $N_i^{100 \mu\text{m}}$ , respectively)

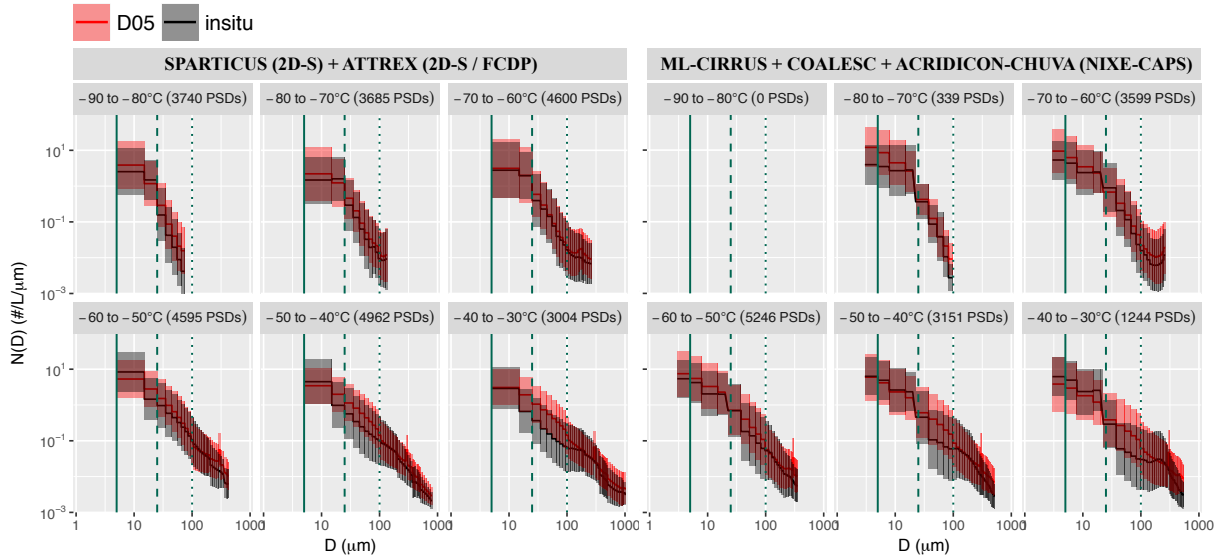


**Figure 1.** Left: Mean PSDs measured (black lines) during ATTREX and SPARTICUS, averaged per  $10^\circ\text{C}$  temperature bins (from  $-90$  to  $-30^\circ\text{C}$ ). Black contours indicate one standard deviation around the mean. The mean and spread of one-to-one predictions by the D05 parameterization are similarly indicated in red. The total amount of PSDs in each  $T_c$  bin is indicated in the legend and the relative contributions from each campaign can be deduced from Fig. S1. Vertical plain, dashed and dotted green lines indicate  $D = 5, 25$  and  $100 \mu\text{m}$ , respectively. The SPARTICUS data with  $T_c < -60^\circ\text{C}$  is here ignored to avoid contaminating FCDP measurements with uncertainties arising from the first first size bins of 2D-S. Right: Similar, for the ACRIDICON-CHUVA, ML-CIRRUS and COALESC campaigns.

will also be used during this evaluation. The  $D_{\min} = 25 \mu\text{m}$  threshold corresponds to allows to represent ice crystals of moderate sizes for which in situ measurements can be considered of higher confidence (e. g. the first two 2D-S bins are removed). The  $D_{\min} = 100 \mu\text{m}$  threshold typically involves measurements where no shattering is expected but also corresponds to sizes for which the concentrations for which in situ measurements are the most accurate and the D05 parameterization is expected to perform well.

It is worth mentioning that different physical processes are likely to influence  $N_i$  depending on the threshold choice. For instance, small particles that are nucleated through homogeneous freezing should dominate  $N_i^{5 \mu\text{m}}$ , whereas large particles resulting from aggregation processes are likely to influence  $N_i^{100 \mu\text{m}}$ .

## 4 In situ evaluation

### 4.1 Theoretical capability to predict Optimal predictability of $N_i$ by D05

Mean PSDs measured during ATTREX and SPARTICUS (black lines), averaged per  $10^\circ\text{C}$  temperature bins (from  $-90$  to  $-30^\circ\text{C}$ ). Black contours indicate one standard deviation around the mean. The mean and spread of one-to-one predictions by the D05 parameterization are similarly indicated by red lines and contours, respectively. The total

amount of PSDs in each temperature bin is indicated in the legend.

This section investigates the ability of the PSD parameterization by The ability of D05 to predict  $N_i$ . PSD predictions are is now investigated. It is reminded that this parameterization is designed to predict  $M_2$  and  $M_6$  and so its representation of the distribution in small particles remains to be tested. PSDs and  $N_i$  predictions by D05 are here computed on the basis of IWC and  $N_0^*$  corresponding to values from each of the 40 000 PSDs composing the dataset described in Sec. 3.2. Comparing these predictions to the back to the original in situ PSDs and  $N_i$  measurements should provide insights on the accuracy of subsequent abilities and limitations of D05 to predict  $N_i$  values to be expected from D05 in case of optimal retrievals (i.e. when assuming that IWC and  $N_0^*$  are perfectly constrained (i.e. if DARDAR retrievals of these parameters were optimal).

#### 4.1.1 Reproducibility of the PSDs by D05

As indicated in Sec. 2.1, the D05 parameterization predicts PSDs based on the assumption of a “universal” size distribution shape and the knowledge of two scaling parameters. Following this formalism, a PSD prediction by D05 can be obtained given the  $D_m$  and  $N_0^*$  values corresponding to each measured PSD.  $D_m$  can directly be extracted from in situ PSDs, as it corresponds to the ratio of  $M_4$  to  $M_3$ .  $N_0^*$  can be indirectly estimated from  $D_m$  and the IWC, using Eq. (9). It can be noted that  $N_0^*$  is proportional to  $\text{IWC} \times D_m^{-4}$ ,

which means that predictions by D05 are much more sensitive to  $D_m$  than to the IWC. This point makes the use of  $m_{L16}(D)$  to estimate IWC a reasonable approximation for the purposes of this evaluation. The size dimension of PSDs predicted by D05 has been converted from  $D_{eq}$  to  $D$  to improve the clarity of the following comparisons. ~~Similar to Fig. ??, for the ACRIDICON-CHUVA, ML-CIRRUS and COALESC campaigns. Density scatterplot showing  $N_i$  theoretically estimated by D05 as function of corresponding in situ measurements (from white to black indicates high to low frequency of occurrence). Color isolines indicate the 68% (one standard deviation) confidence interval for each campaign. Density and confidence intervals are provided per 10°C temperature bins from -80 to -30°C (first to fifth column) and lower integration threshold for  $N_i$  (5, 25 and 100  $\mu\text{m}$  in the first, second and third row, respectively).~~

Comparisons between the PSD measurements obtained during ATTREX2014 and SPARTICUS and corresponding predictions by D05 are shown in Fig. ??1 (left panels). The black and red lines respectively indicate the mean measured and predicted PSDs within 10°C temperature bins. The use of measurements from mid-latitude (SPARTICUS) and TTL ice clouds (ATTREX2014) allows a high statistical significance to be reached (over 3000 PSDs) in each  $T_c$  bin from -90 to -30°C. The colored contours indicate one standard deviation around that mean. It can be noted that the measured and predicted concentrations in the FCDP bins have been averaged within each of the two first 2D-S bins in order to conveniently display the means in Fig. ??1. This figure clearly shows a very good overall agreement between D05 predictions and the in situ measurements. The mean as well as the spread of the 2D-S and FCDP measurements are well represented by D05. The agreement is especially good for  $-90^\circ\text{C} < T_c < -50^\circ\text{C}$ , where the in situ distribution tends to be mono-modal with very few large particles. ~~However, an overestimation of the~~ A small overestimation by D05 of the concentration of crystals smaller than 25  $\mu\text{m}$  is still noted when  $T_c < -70^\circ\text{C}$ . An overestimation of the number of particles with  $D < 100 \mu\text{m}$  is also noted for D05 from  $T_c > -50^\circ\text{C}$ , where a second mode appears for large aggregated particles. Such features and temperature dependency of PSD shapes have already been widely reported in the literature (e.g. Mitchell et al., 2011; Mishra et al., 2014; Luebke et al., 2016). In the occurrence of a bi-modal shape in in situ measurements, the D05 parameterization naturally tends to reproduce the concentration ~~in-of~~ large particles due to their strong weight on  $D_m$  and IWC. Because a monomodal shape is assumed to describe the PSD in D05, an erroneous extrapolation of the concentration ~~in-of~~ small particles leads to the observed overestimation when  $T_c > -50^\circ\text{C}$ . However, this overestimation appears to mainly concern particles from 25 to 100  $\mu\text{m}$ , as the concentration ~~in-of~~ ice particles smaller than about 15  $\mu\text{m}$  seems accurately predicted when  $T_c > -70^\circ\text{C}$  (keeping in mind that measurements for such small particles can be highly uncertain).

These results are supported by the evaluation of the D05 predictions of NIXE-CAPS measurements during ACRIDICON-CHUVA, COALESC and ML-CIRRUS, which are similarly shown ~~in-on the right-hand side of Fig. ??1~~. Despite much fewer measurements of ice clouds with  $T_c < -70^\circ\text{C}$ , very good agreements are found in the mean and the spread predicted by D05 for  $-50 < T_c < -70^\circ\text{C}$ . A ~~slight small~~ overestimation of the concentration of small ice crystals ~~is found between -80 and -70°C, as the concentration keeps increasing in D05 towards small diameters but not for the ( $D < 25 \mu\text{m}$ ) is found for  $T_c < -60^\circ$ , where concentrations measured by the NIXE-CAPS only slightly increase.~~ This feature should ~~nevertheless~~ be carefully accounted for due to the lack of measurements in ~~this temperature bin, the coldest temperature bin, but could again indicate a too steep increase of  $N_i$  towards small particles in D05 (i.e., a too negative  $\alpha$ ) at very low temperatures.~~ Consistent with the previous results, the D05 predictions are less accurate towards higher temperatures as bi-modal structures tend to appear in the in situ measurements above  $-50^\circ\text{C}$ . Moreover, comparing ~~Fig. ?? with Fig. ?? all campaigns~~ shows a very good overall agreement between the NIXE-CAPS and 2D-S/FCDP measurements, which points towards the generalization of these conclusions. It should be mentioned that these analyses are not repeated by explicitly discriminating between cloud types (e.g. synoptic cirrus/anvil or liquid/ice origin) for reasons of brevity. The overall agreements observed in Fig. ?? and Fig. ??1 for each are considered satisfactory in this evaluation, especially since DARDAR does not discriminate between cloud types and the normalized size distribution used in D05 is expected to perform equally for all cloud types. ~~Similar to Fig. 2, scatterplots of  $N_i$  retrieved by DARDAR-LIM as function of the co-incident in situ SPARTICUS measurements.~~

#### 4.1.2 Consequences on $N_i$ predictions

$N_i$  obtained from direct integrations of the measured and predicted PSDs are now compared. Fig. 2 shows a density scatterplot of one-to-one comparisons between the in situ measurements (x-axis) and corresponding D05 predictions (y-axis), obtained by integrating the corresponding PSDs from  $D_{min} = 5, 25$  and  $100 \mu\text{m}$  (first to third row, respectively). The background color indicates the overall density and isolines are provided to show the 68% confidence levels (i.e. from which all values inside fall within one standard deviation  $\sigma$  from the mean) for each campaign. These results are shown per 10°C temperature bins from  $-80^\circ\text{C}$  to  $-30^\circ\text{C}$  (first to fifth column, respectively).

Fig. 2(c,a-e) show that the prediction of  $N_i$  for ice particles larger than 100  $\mu\text{m}$  is very consistent with the in situ ~~truthreference~~, with an agreement close to the one-to-one line for all campaigns and temperatures.  $N_i^{100\mu\text{m}}$  values ranging between about 1 and 100  $\text{L}^{-1}$  are observed. This good agreement was expected from Sec. 4.1.1, and because D05



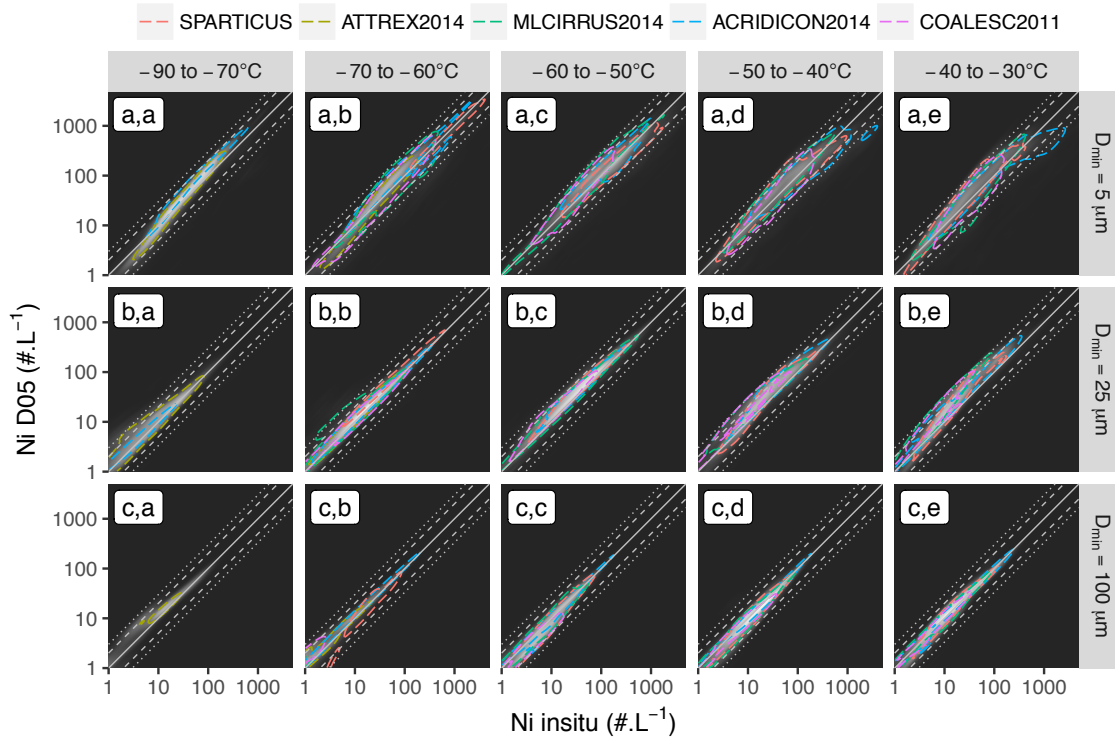


**Figure 2.** Density scatterplot showing  $N_i$  theoretically estimated by D05 as function of corresponding in situ measurements (from white to black indicates high to low frequency of occurrence). Color isolines indicate the 68% (one standard deviation) confidence interval for each campaign. Density and confidence intervals are provided per  $10^\circ\text{C}$  temperature bins from  $-80$  to  $-30^\circ\text{C}$  (first to fifth column) and lower integration threshold for  $N_i$  ( $5$ ,  $25$  and  $100 \mu\text{m}$  in the first, second and third row, respectively). The identity line and a factor of 2 and 3 around it are indicated by grey plain, dashed and dotted lines, respectively.

should in principle perform best at reproducing the concentration in large particles. Fig. 2(b,a-e) also indicates an accurate prediction of  $N_i^{25 \mu\text{m}}$ , well within a factor of 2 (dashed lines), from  $-80$  to  $-50^\circ\text{C}$ . However, at higher temperatures,  $N_i^{25 \mu\text{m}}$  predictions by D05 are can be overestimated by a factor of 2 to 3 (dotted lines) for most field campaigns. These results also hold for  $N_i^{5 \mu\text{m}}$ , as indicated in Fig. 2(a,a-e), despite a larger spread within and between the campaigns in this case. It can be noted that the overestimation is particularly strong for SPARTICUS (red isolines) but is less clear for other campaigns. The overestimation is also not as clear as for  $N_i^{25 \mu\text{m}}$ , as the concentration of in particles smaller than  $25 \mu\text{m}$  appears more properly predicted by D05, as shown in (see Fig. ?? and Fig. ??-1). At  $T_c < -50^\circ\text{C}$ , the D05 predictions are more consistent with the in situ measurements, with maximal  $N_i^{5 \mu\text{m}}$  values of about  $300 \text{ L}^{-1}$  but that can also reach up to  $1000 \text{ L}^{-1}$  for several field campaigns. A small overestimation, by a factor less than 2, can nevertheless be observed in  $N_i^{5 \mu\text{m}}$  predictions by D05 when  $T_c < -60^\circ\text{C}$ . This is consistent with its steeper increase of the concentration in small ice crystals, noted in Fig. 1.

## 4.2 Satellite estimates vs. co-incident measurements

### The theoretical

Section 4.1 demonstrated the ability of the D05 parameterization to predict  $N_i$  measurements from numerous airborne campaigns was demonstrated in Sec. 4.1. However, these conclusions only reflect ideal cases, where the input parameters of this parameterization are perfectly known. In other words, they correspond to the expectations for retrievals where the lidar and/or radar information are capable of perfectly constraining these parameters. D05 are perfectly constrained, since IWC and  $N_0^*$  were extracted from the in situ data. It is now necessary to investigate if enough information is contained in these measurements to constrain  $D_m$  and  $N_0^*$  so that  $N_i$  is well estimated. lidar and radar measurements to sufficiently constrain these two parameters and estimate  $N_i$ .

This question is investigated by comparing the DARDAR-LIM  $N_i$  to measurements from co-incident flights. These flights are selected under the condition that they are within a maximum distance of 5 km and a 30-min time period from the CloudSat/CALIPSO overpass. Among the cam-

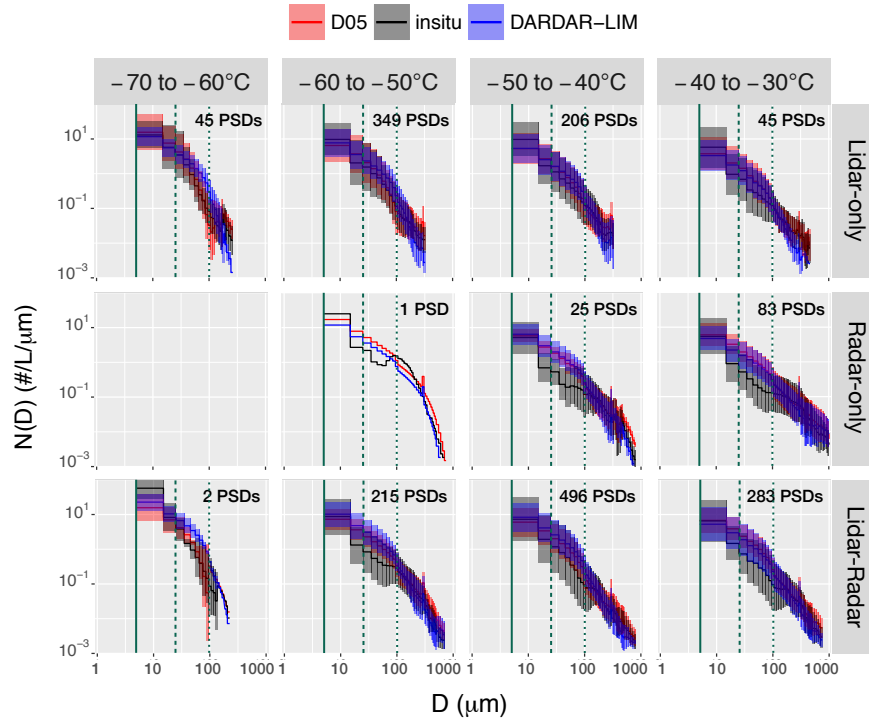


**Figure 3.** Similar to Fig. 1 but for SPARTICUS flights co-incident with the A-Train overpass. PSDs estimated on the basis of DARDAR IWC and  $N_0^*$  retrievals (i.e. corresponding to the DARDAR-LIM  $N_i$ ) is shown in blue. All PSDs are averaged per temperature bin (columns) and instrumental conditions met during DARDAR retrievals (rows).

paings described in Sec. 3.2.1, co-incident flights with the A-Train track were intended during ACRIDICON-CHUVA, ML-CIRRUS and SPARTICUS. Unfortunately, none of the 3 co-incident flights during ACRIDICON-CHUVA could be selected here, due to the absence of CALIOP measurements (12 Sept. 2014) or flights that do not fulfill the above conditions (about 3 h late or 350 km West from the overpass track on 21 and 23 Sept. 2014, respectively). Also, technical issues occurred during the ML-CIRRUS co-incident flights (04 April 2014), making PSD measurements uncertain and not usable for this evaluation. However, numerous flights successfully achieved a close spatial and temporal co-incident with the A-Train during SPARTICUS. A list and description of all these flights can be found in Deng et al. (2012). Overall, about 2150–1750 PSDs were here found to match the above conditions and are considered in this evaluation. The co-incident DARDAR-LIM  $N_i$  are obtained by selecting the closest pixel (based on a great-circle distance) at the altitude of the airplane.

Figure ?? shows 3 compares, similarly to Fig. 2, scatterplots of the DARDAR-LIM  $N_i$  as function of co-incident 1, PSDs measured by the 2D-S measurement for the three considered  $D_{min}$  along A-Train overpasses (black) to corresponding predictions by D05 (red). PSDs predicted by D05 on the basis of co-incident DARDAR IWC and  $N_0^*$  thresholds and four  $T_c$  retrievals are additionally shown

in blue. These correspond to the PSDs that are integrated to compute  $N_i$  bins from  $-70$  to  $-30$  in DARDAR-LIM. All PSDs are averaged per  $10^\circ\text{C}$ . It can first be observed that these comparisons are rather widely scattered, as could be expected due to the difficulty of performing one-to-one comparisons between satellite and airborne measurements. Nevertheless, the  $N_i^{100\mu\text{m}}\text{C}$  bins (columns) and by instrumental conditions met for DARDAR retrievals (rows). In agreement with results from Sec. 4.1.1, the theoretical predictions by D05 are in better agreement with 2D-S observations when the latter display monomodal shapes. This is mainly observed towards low temperatures but also when retrievals are obtained in lidar-only, i.e. for thin cirrus or in regions near cloud-top. The 2D-S PSDs feature a stronger bi-modality in lidar-radar and radar-only regions, where larger crystals resulting from aggregation or complex heterogeneous nucleation processes are likely to appear. D05 is by construction unable to reproduce this behaviour but, despite disagreements with the 2D-S, PSDs retrieved by DARDAR-LIM agree well with D05 predictions based on in situ measurements. This indicates that  $N_0^*$  is in good overall agreement. In spite of the large scatter, the isoline representative a  $1-\sigma$  spread (dashed red) is centered around the one-to-one line. However, a clear tendency towards an overestimation of and IWC are sufficiently retrieved and that errors on  $N_i$  when  $T_c$  are

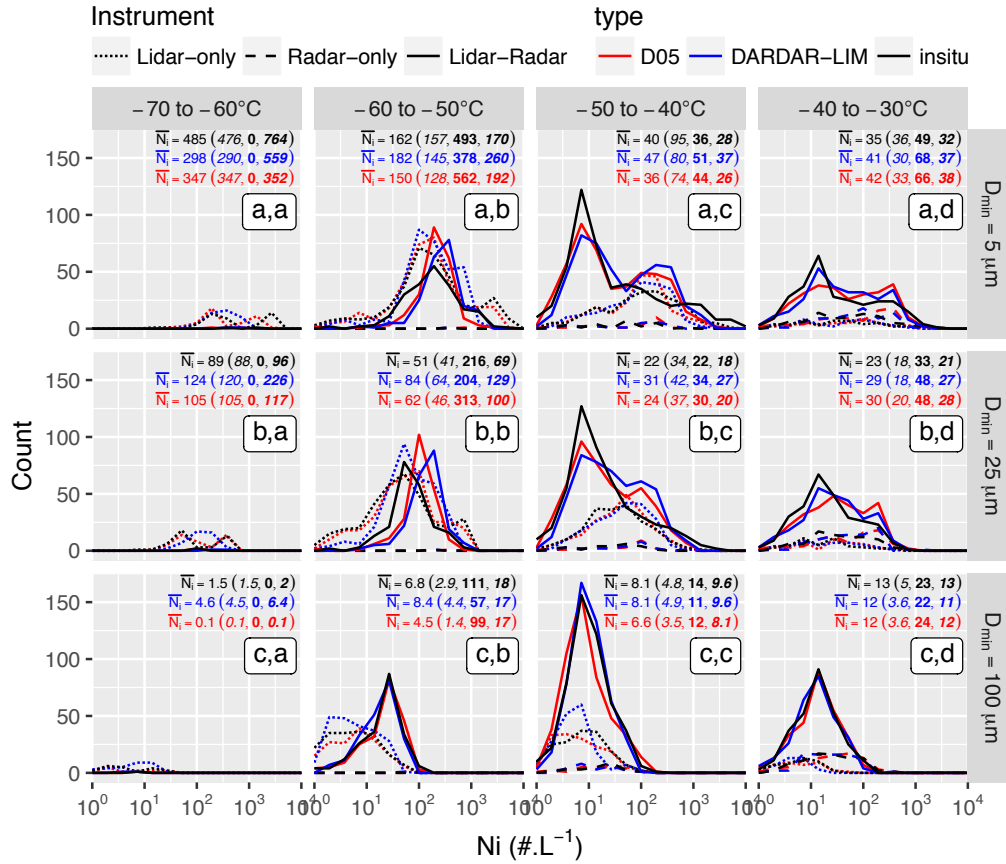


**Figure 4.** Histograms of  $N_i$  measured during SPARTICUS (black), theoretically estimated by D05 (red) and retrieved by DARDAR-LIM (blue). Plain, dotted and dashed lines indicate that DARDAR retrievals were obtained using the lidar-only, radar-only and lidar-radar, respectively. Panels indicate the temperature and integration threshold, similarly to Fig. 2. Geometric means of  $N_i$  (in L<sup>-1</sup>) are shown in each panel for 2D-S, DARDAR-LIM and D05. The overall mean is first indicated, followed in brackets by values for the lidar-only (italic), radar-only (bold) and lidar-radar (bold-italic) subsets.

likely to be dominated by assumptions on the PSD shape. That is especially true in lidar-radar conditions where  $\beta_{ext}$  and  $Z_e$  both provide information on the concentration of small and large particles, respectively. As expected, the concentrations in particles with  $D \gg -50^\circ\text{C}$  is observed for  $N_i^{5\mu m}$  100  $\mu m$  and  $N_i^{25\mu m}$ . For colder temperatures, the DARDAR-LIM  $N_i$  are not well constrained in lidar-only conditions. Inversely, radar-only retrievals poorly constrain concentrations in particles smaller than 100  $\mu m$ . However, Fig. 3 shows that, despite fewer available constraints under lidar-only conditions, reasonable  $N_i^{5\mu m}$  estimates are in much better agreement with the SPARTICUS measurements. Despite the larger scatter, these results are consistent with expectations from Sec. 4.1.2. Histograms of  $N_i$  measured during SPARTICUS (black), theoretically estimated by D05 (red) and retrieved by DARDAR-LIM (blue). Plain, dotted and dashed lines indicate that DARDAR retrievals were obtained using the lidar-radar, lidar-only, radar-only, respectively. Panels indicate the temperature and integration

threshold, similarly to Fig. 2, and  $N_i^{25\mu m}$  estimates are obtained due to simpler PSD shapes.

In order to avoid problems related with one-to-one comparisons of satellite and airplane measurements, a statistical comparison is presented in Fig. 4. This figure shows histograms of  $N_i$  distributions for the 2D-S (black) and DARDAR-LIM (blue) per temperature bin and  $D_{min}$  threshold. Additionally, the theoretical prediction—Theoretical predictions by D05 (obtained using the in situ  $D_m$  and  $N_0^*$ ) also is are indicated in red to provide an idea of the optimal expectations from D05 for DARDAR-LIM. Plain, dotted and dashed lines indicate satellite estimates that were obtained using the correspond to lidar-radar, lidar-only, radar-only measurements conditions, respectively. These histograms are individually shown in Fig. 4(c,a-d) show a very good agreement S6 for a better clarity. Mean  $N_i$  values for 2D-S, DARDAR-LIM and D05 are indicated in each panel. Very good agreements are seen between the satellite  $N_i^{100\mu m}$  in comparison to the in-situ observations estimates and in situ



observations of  $N_i^{100\mu\text{m}}$  at all temperature ranges. This agreement appears to be equally good for retrievals obtained in lidar-only, above  $-60^\circ\text{C}$ . The distributions and mean values of  $N_i^{100\mu\text{m}}$  estimated by DARDAR-LIM are perfectly consistent with the 2D-S for all instrumental conditions. Deviation of radar-only or lidar-radar conditions values in the  $-60$  to  $-50^\circ\text{C}$  bin (Fig. 4(a,a-c)) shows that the estimation of  $N_i^{5\mu\text{m}}$  (c,b)) can be discarded as only representative of 1 PSD. The satellite estimates of  $N_i^{25\mu\text{m}}$  is relatively consistent also agree with the 2D-S observations for  $T_c < -50^\circ\text{C}$ . The expected overestimation for higher temperatures tends is observed, as the, however with the expected overestimation of  $N_i^{25\mu\text{m}}$  in D05 and DARDAR-LIM histograms appear nearly shifted by a factor of about 2 to 3. It should nevertheless be kept in mind that SPARTICUS featured the strongest biases at these temperature range by comparison to other campaigns, as seen in due to limited PSD shape assumptions. Overestimations by about 10 to 30% and 20 to 60% are found in the mean values of  $N_i^{25\mu\text{m}}$  by D05 and DARDAR-LIM, respectively. This overestimation is less in lidar-only conditions, consistently with the weaker bi-modality of PSDs (see Fig. 2,  $N_i^{5\mu\text{m}}$ 3). Similar observations can be made for  $N_i^{5\mu\text{m}}$  with a slightly smaller overestimation of the mean values by DARDAR-LIM due to good agreements between DARDAR-LIM and 2D-S for  $D < 15\mu\text{m}$  estimates obtained from lidar-only and lidar-radar measurements are all in good agreement, which indicates that reliable noted in Fig. 3. However, it is reminded that uncertainties in the 2 first bins of the 2D-S can contaminate its estimations of  $N_i^{5\mu\text{m}}$  and so  $N_i^{25\mu\text{m}}$  represents a more trustworthy estimate of  $N_i$  estimates can be obtained from any of these combinations. The statistical sampling of retrievals obtained in radar-only condition is too poor to draw any strong conclusions, from this instrument. Finally, it clearly appears from Fig. 4 that, even when the distributions from DARDAR-LIM and the 2D-S do not perfectly agree, the satellite estimates very often remain close to the D05 predictions. Because the latter represent ideal retrievals, this again proves that sufficient information is contained in lidar-radar measurements to successfully constrain the. This again indicates that errors in  $N_i$  estimates by DARDAR-LIM are dominated by assumptions made on the PSD shape rather than by a lack of instrumental sensitivity.

Figures 3 and 4 therefore demonstrate that DARDAR-LIM is capable of statistically reproducing 2D-S measurements of  $N_i^{100\mu\text{m}}$ ,  $N_i^{25\mu\text{m}}$  and  $N_i^{5\mu\text{m}}$  with an overestimation up to about a factor of 2 that can be expected in the mean  $N_i^{25\mu\text{m}}$  and  $N_i^{5\mu\text{m}}$  values due to a misrepresentation of the PSD shape by D05 input parameters and estimate  $N_i$  at warm temperatures. An analysis of one-to-one comparisons between DARDAR-LIM/D05 and 2D-S (see Fig. S4 and S5) also support these conclusions.

## 5 Case study

A first examination of  $N_i$  profiles by DARDAR-LIM is performed here in the context of a case study corresponding to a frontal ice cloud structure observed on 03 February 2010 around 20:00 UTC over South Central USA. This case is of particular interest as it contains a leg of high spatial and temporal coincidence between the A-Train and the Learjet-25 aircraft involved during SPARTICUS.

### 5.1 Overall context

The cloud structure analyzed here is part of a mature cyclonic system that has reached an occluded stage, as featured by the brightness temperature snapshot shown in Fig. 5(a). Further analyses of the weather conditions (not shown here for brevity reasons) indicated that this system originated from a mid-tropospheric wave pattern that crossed the US and supported a surface low pressure area over North Central Mexico. The storm then moved northwesterly, eventually reaching Northeastern USA on 05 February as a major blizzard.

The CloudSat track crossed the cyclone from south to north around 19:55 UTC (dashed green line). The section of interest for this case study (plain green line) captures a frontal cloud associated with the ascending southern moist warm air flow atop cold continental air mass. The corresponding CloudSat  $Z_e$  and CALIOP  $\beta_{\text{ext}}$  profiles, shown in Fig. 6(a-b), typically hint to high water contents and precipitation toward the center of the cyclone and to thin ice clouds as the A-Train moves northwards toward its periphery.

The Learjet-25 performed in situ measurements in a cirrus at the edge of the cyclone. The flight track is shown by black lines in Fig. 5(a-b) and Fig. 6. These figures indicate that the aircraft approached from the west at an altitude of about 10.7 km (near cloud top) and descended to about 8 km (near cloud base) before reaching the overpass. The aircraft then closely followed the A-Train while ascending to cloud top and finally descended back to cloud base in a spiral. Optimal comparisons between the A-Train and Learjet-25 measurements are thus expected within the ascending leg from about  $39.5$  to  $40.7^\circ\text{N}$ , where the time and space coincidences are well within 15 min and 10 km, respectively.

### 5.2 Vertical structure along the overpass

Profiles of  $r_{\text{eff}}$ , IWC,  $N_i^{5\mu\text{m}}$ ,  $N_i^{25\mu\text{m}}$  and  $N_i^{100\mu\text{m}}$  along the selected A-Train overpass are respectively shown in Fig. 6(d-fd-h). As expected, high IWC values are retrieved between altitudes of 2.5 and 7.5 km along the southern half of the track ( $31.2$ - $35.4^\circ\text{N}$ ), i.e. towards the center of the cyclone. Retrievals of  $r_{\text{eff}}$  indicate small crystals (about  $30\mu\text{m}$  or less) above the  $40^\circ\text{C}$  isoline (dashed red line) and particles larger than  $100\mu\text{m}$  below 8 km. The clear cut below 2.5 km, associated with high  $Z_e$ , corresponds to pixels classified as rain by the DARDAR mask. Fig. 6(ef) shows that large high

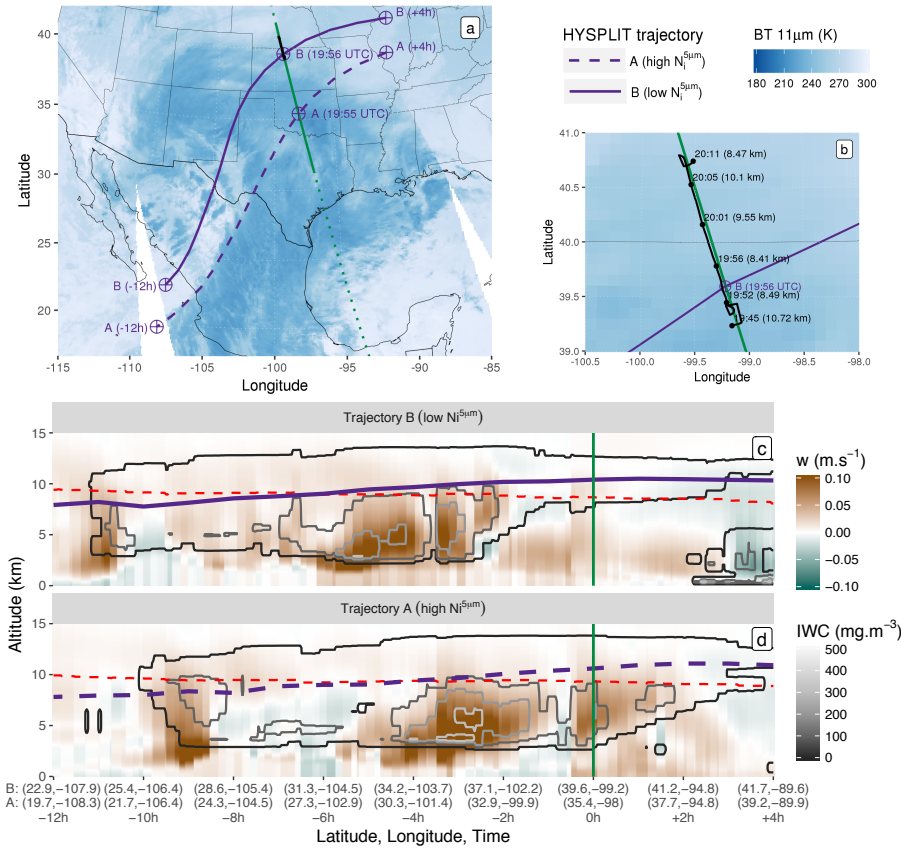


**Figure 5.** (a): Map summarizing the observations during the case study. The shaded blue background corresponds to MODIS/Aqua 11  $\mu\text{m}$  brightness temperature measurements around the A-Train overpass. The CloudSat track is shown by a dotted green line and a plain green line highlights the region of interest. The Learjet-25 flight track is shown in black. Dashed and plain purple lines represent HYSPLIT trajectories computed for 2 air parcels of high (A) and low (B)  $N_i^{5\mu\text{m}}$ , respectively, at 11 km along the overpass. (b): Similar to (a) but zoomed in around the flight area. The aircraft UTC times and altitudes are indicated in black. (c-d): Vertical cross sections of  $w$  (background color) and IWC (grey contours) predicted by NARR along the B and A trajectories, respectively. The positions of the corresponding air parcel are indicated in purple. A dashed red line shows the  $-40^\circ\text{C}$  isotherm. The overpass time is highlighted by a vertical green line.

$N_i^{5\mu\text{m}}$  values are found towards cloud top, with values ranging from 250 to more than  $1000\text{ L}^{-1}$ .  $N_i^{5\mu\text{m}}$  strongly increases above the  $-40^\circ\text{C}$  isotherm (dashed red line), consistently with the probable occurrence of homogeneous nucleation below that temperature threshold. However, the increase in  $N_i^{5\mu\text{m}}$  when  $T_c < -40^\circ\text{C}$  is not spatially homogeneous. Indeed, very high values (reaching  $1000\text{ L}^{-1}$ ) are observed between  $33.3$  and  $36.5^\circ\text{N}$ , where the cloud-base heights starts increasing in relation with the frontal system. However, lower  $N_i^{5\mu\text{m}}$  with values, typically between  $250$  and  $500\text{ L}^{-1}$ , are observed above  $-40^\circ\text{C}$  toward the cyclone periphery ( $36.5$  to  $41.5^\circ\text{N}$ ). This distribution of  $N_i^{5\mu\text{m}}$  is could be consistent with expectations of stronger updraughts and vertical transport of moisture closer to near the center of the cyclone, resulting in higher homogeneous nucleation rates by comparison to a more mature stage of the cloud (Krämer et al., 2016). This could result from high homogeneous freezing rates of aqueous aerosols that occur

on top of existing ice crystals heterogeneously formed from liquid droplets (the area of high backscatter around  $33.3^\circ\text{N}$  in Fig. 6(b) indicates the presence of supercooled liquid water). This hypothesis will further be discussed in Sec. 5.3.

Vertical profiles of  $N_i^{100\mu\text{m}}$  The vertical distribution of  $N_i^{25\mu\text{m}}$  are in Fig. 6(g) shows patterns that are similar to  $N_i^{5\mu\text{m}}$ , with absolute values that are about 50% lower. Profiles of  $N_i^{100\mu\text{m}}$  shown in Fig. 6(f) — It is observed — indicate that areas of high  $N_i^{100\mu\text{m}}$  are located deeper in the cloud than where high  $N_i^{5\mu\text{m}}$  and  $N_i^{25\mu\text{m}}$  are found.  $N_i^{100\mu\text{m}}$  tends to increase below regions of high  $N_i^{5\mu\text{m}}$ , which is coherent with possible aggregation processes, and remains constant or decreases slightly towards cloud base before precipitating from the lowermost layers. Very high  $N_i^{100\mu\text{m}}$  values appear around  $33.0^\circ\text{N}$ , coincident with high IWC values. However, Fig. 6(b) shows the presence of a supercooled cloud layer in this area, typically below an area of high backscatter coefficient at high altitude, this area is subject

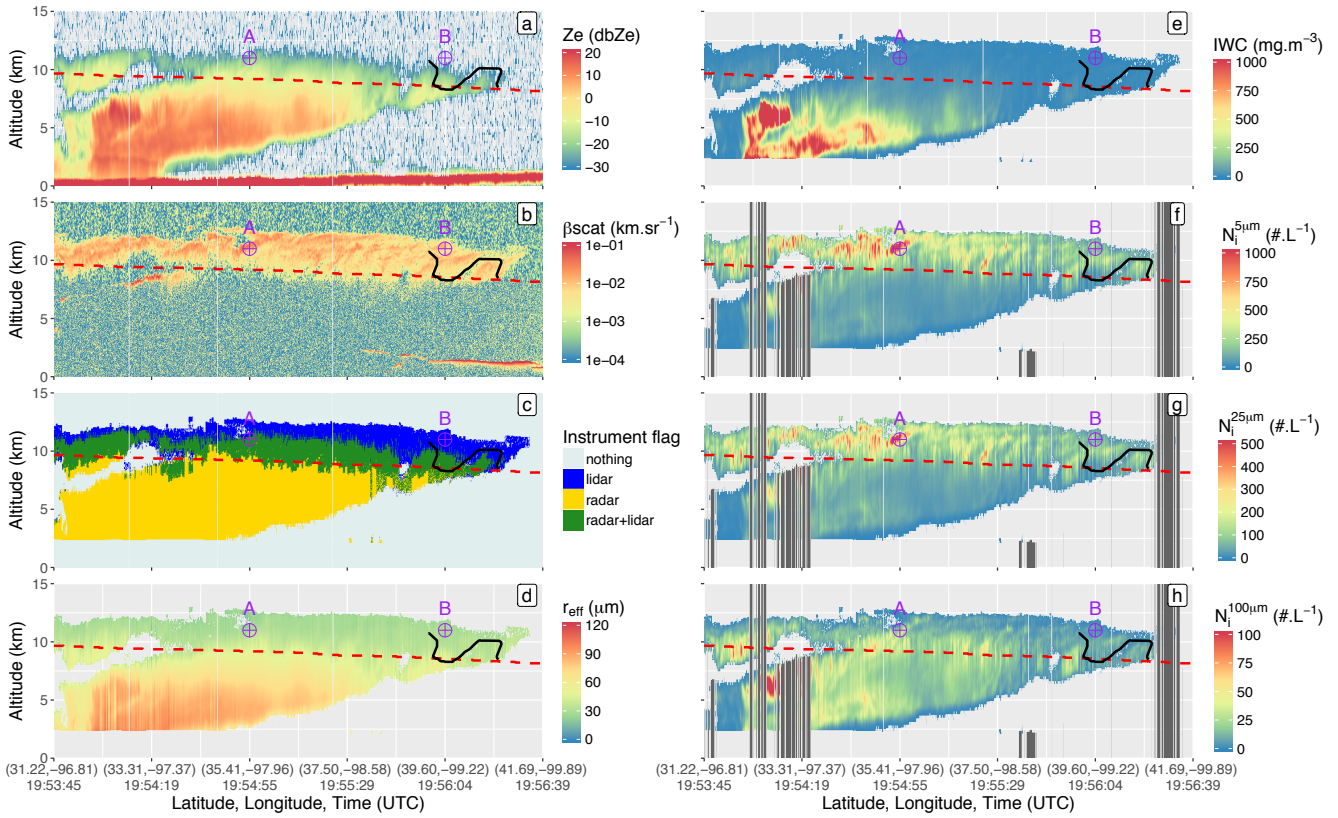


**Figure 6.** Vertical profiles of the (a) CloudSat reflectivity factor, (b) CALIOP backscatter coefficient, (c) DARDAR instrument flag, (d)  $r_{\text{eff}}$ , (e) IWC, (e-ff-h) DARDAR-LIM  $N_i^{5\mu\text{m}}$ ,  $N_i^{25\mu\text{m}}$  and  $N_i^{100\mu\text{m}}$ , respectively, along the selected A-Train overpass (plain green line in Fig. 5). Dark-grey shaded areas in (e-ff-h) indicate a rejection of the retrievals (insufficient  $n_{\text{iter}}$  or the below a supercooled layer; see Sec. 3.1). The  $-40^\circ\text{C}$  isotherm is in dashed red, the location of the A and B air parcels are indicated in purple, and the Learjet-25 track is shown in black.

to supercooled layers, where retrievals are highly uncertain. It is worth noting that the  $N_i^{100\mu\text{m}}$  distribution does not necessarily follows that of the IWC.

Furthermore, finally, it can be noted when comparing the  $N_i$  profiles in Fig. 6(e-ff-h) with the corresponding instrumental flags shown in Fig. 6(c) indicates that no clear bias is observed within transition areas between the cloud properties obtained in lidar-only, radar-only and lidar-radar conditions, confirming the conclusions from Fig. 4 consistent with conclusions from Sec. 4.2.

Finally, comparisons between DARDAR-LIM and coincident A detailed analysis of 2D-S measurements are presented in Fig. ???. The method for co-locating and comparing aircraft and satellite observations is identical to that used in Sec. 4.2, except that no filters based on the coincidence distance and time are applied here. Overall, this figure shows very similar  $N_i^{5\mu\text{m}}$  and  $N_i^{100\mu\text{m}}$  patterns between the satellite estimates and the in situ measurements, with especially good agreements along the ascending leg corresponding to the optimal coincidence region ( $39.5\text{--}40.7^\circ\text{N}$ ). Few discrepancies are nevertheless observed

outside this region. For instance, DARDAR-LIM does not capture well the sporadic strong increases of  $N_i^{5\mu\text{m}}$  observed above 10 km, which however corresponds to measurements where the aircraft largely deviated from the A-Train track (western leg in along the co-incident flight leg (see Fig. 5(b))), and slightly overestimates  $N_i^{5\mu\text{m}}$  along the descending leg around  $40.75^\circ\text{N}$ . Also, the increase in  $N_i^{100\mu\text{m}}$  observed by the 2D-S along the descending leg around  $39.4^\circ\text{C}$  is well not captured by the satellite, possibly because of a movement of the cloud layer or a slight difference in the co-location (Fig. 6(f) indicates  $N_i^{100\mu\text{m}}$  values between 25 and  $50\text{ L}^{-1}$  next to the aircraft track). However, accounting for the difficulties to directly compare aircraft and satellite observations, it can be concluded here that S7) showed good overall agreements with DARDAR-LIM reproduces reasonably well the average values and variations of the  $N_i^{5\mu\text{m}}$  estimates of  $N_i^{5\mu\text{m}}$ ,  $N_i^{25\mu\text{m}}$  within this cloud layer, thus supporting the conclusions drawn from Sec. 4.2. and  $N_i^{100\mu\text{m}}$ . Despite few discrepancies, the overall variations of  $N_i$  appear well captured by DARDAR-LIM, in particular



along the ascending leg, which has the highest time and space coincidence with the satellite overpass.

### 5.3 Trajectory analysis of $N_i^{5\mu\text{m}}$ patterns

~~(a,a-b)  $N_i^{5\mu\text{m}}$  measured by the 2-DS and retrieved by DARDAR-LIM, respectively, along a projection of the Learjet-25 track on the A-Train overpass. (b,a-b) Similar to previous but for  $N_i^{100\mu\text{m}}$ .~~

Thorough investigations of nucleation processes based on DARDAR-LIM are not in the scope of this paper and will further be discussed in the part two of this series. Nevertheless, a qualitative analysis is here presented to provide further explanation to the  $N_i^{5\mu\text{m}}$  patterns observed in this case study.

To achieve this, back- and forward-trajectories were computed from the points A and B indicated in Fig. 6, using the Hybrid Single Particle Lagrangian Integrated Trajectory Model (HYSPLIT; Stein et al., 2015) coupled with the North American Regional Reanalysis (NARR; Mesinger et al., 2006) model. A and B correspond to air parcels associated with high and low  $N_i^{5\mu\text{m}}$ , respectively, when  $T_c < -40^\circ\text{C}$ . Their trajectories (from -12 to +4h starting at the overpass time) are shown as dashed and plain purple lines, respectively, in Fig. 5(a). The corresponding altitudes are similarly indicated as function of time in Fig. 5(c-d). Complementarily, the vertical cross-sections of vertical wind velocities ( $w$ ) predicted by NARR along the trajectories are indicated by a color background in Fig. 5(c-d). Contours of the NARR IWC are shown in grey to serve as rough indicators of the presence of ice cloud layers in the model. It can be noted that NARR provides reanalyses with an horizontal resolution of 32 km, 29 vertical levels and with 3-hourly outputs; the closest output times and grid-points were therefore selected.

It is observed that, in agreement with expectations, both air parcels originated from warm moist air over the Pacific and slowly ascended atop the cold continental air following northwesterly trajectories associated with slow vertical motions (light brown ~~colours~~ colors). Parcel B ascended from about 8 km at 08:00 UTC to 11 km at the overpass time (20:00 UTC) and then remained at a constant altitude. The  $-40^\circ\text{C}$  isoline (dashed red line) is crossed around 14:00 UTC and this parcel then appears to belong to an anvil-like maturing cloud layer from 19:00 UTC, supported by small  $w$  (less than  $1\text{ cm}\cdot\text{s}^{-1}$ ) observed around the overpass time. On the contrary, parcel A, which also started ascending from an altitude around 7.5 km, met ~~strong convective events~~ stronger uplifts later during the day, around 16:00 UTC. Consistently, the  $-40^\circ\text{C}$  isoline is also crossed about 2 h later than for parcel B. This parcel keeps ascending upon meeting with the overpass, where ~~strong updraughts are still indicated~~ updraughts stronger than  $5\text{ cm}\cdot\text{s}^{-1}$  are found.

These observations are in agreement with the high  $N_i^{5\mu\text{m}}$  values observed at A, thus likely to be caused by strong and recent updraughts ~~that carry moisture above the  $-40^\circ\text{C}$~~

~~isotherm and allow for high homogeneous nucleation rates. This is consistent with a very strong sensitivity of  $N_i$ . The high sensitivity to  $w$  (Krämer et al., 2016) could indeed relate to high in situ homogeneous freezing event of aqueous aerosols, occurring on top of ice crystals formed, probably heterogeneously, from liquid droplets (Kärcher and Ström, 2003; Kärcher et al., 2006; Krämer et al., 2016).~~

. On the contrary, B corresponds to an air parcel within a mature cloud, where  $w$  is too small to cause further ice nucleation and small ice crystals have already started to sublimate or aggregate. It is worth mentioning that these variations of  $N_i$  with  $w$  are in good agreement with findings by Kärcher et al. (2006) based on a physically-based ice nucleation scheme. An exact comparison of absolute numbers is however difficult as Kärcher et al. (2006) also shows a dependence on background ice nuclei concentrations, which are unknown for this case study.

Keeping in mind possible uncertainties associated with the NARR reanalyses and HYSPLIT trajectories, this analysis still provides comforting arguments as to physical meaningfulness of  $N_i^{5\mu\text{m}}$  and  $N_i^{25\mu\text{m}}$  patterns in DARDAR-LIM.

## 6 Preliminary evaluation of Global $N_i$ climatologies

Spatial distributions of  $N_i^{5\mu\text{m}}$ ,  $N_i^{25\mu\text{m}}$  and  $N_i^{100\mu\text{m}}$  corresponding to 10 years of DARDAR-LIM products are now analysed. A thorough evaluation of these distributions remains difficult due to a lack of other reference for such climatological data; preliminary results are thus discussed here to assess the overall coherence of the observed  $N_i$  patterns with general expectations ~~but should be cautiously considered~~. The interpretation of these distributions in terms of evidence of controls on  $N_i$  are here only briefly addressed as they will be the focus of part two.

### 6.1 Global spatial Geographical distributions

Figures 7(a,a-e) show the spatial distribution of  $N_i^{5\mu\text{m}}$  averaged in a  $2\times 2^\circ$  lat-lon grid and subset into  $10^\circ\text{C}$  bins from  $-80$  to  $-30^\circ\text{C}$ . Corresponding pixel counts are shown in Fig. S8. The  $N_i^{5\mu\text{m}}$  shows a strong temperature dependence, with higher  $N_i^{5\mu\text{m}}$  values being observed at colder  $T_c$  globally (Fig. 7(a,a-e)). This  $T_c$  dependence is particularly strong important over tropical land regions and in regions experiencing strong convection (the tropical warm pool, intertropical convergence zone). This is consistent with the strong updraughts in convective regions producing high supersaturations and so higher nucleation rates, causing these increased  $N_i^{5\mu\text{m}}$  values (Kärcher and Lohmann, 2002; Krämer et al., 2016).

Low  $N_i^{5\mu\text{m}}$  below  $100\text{ L}^{-1}$  are observed in subsidence regions, where thin cirrus are typically met. Nevertheless, it should be kept in mind that these regions contain only few ice clouds, most likely remnants of jets stream or

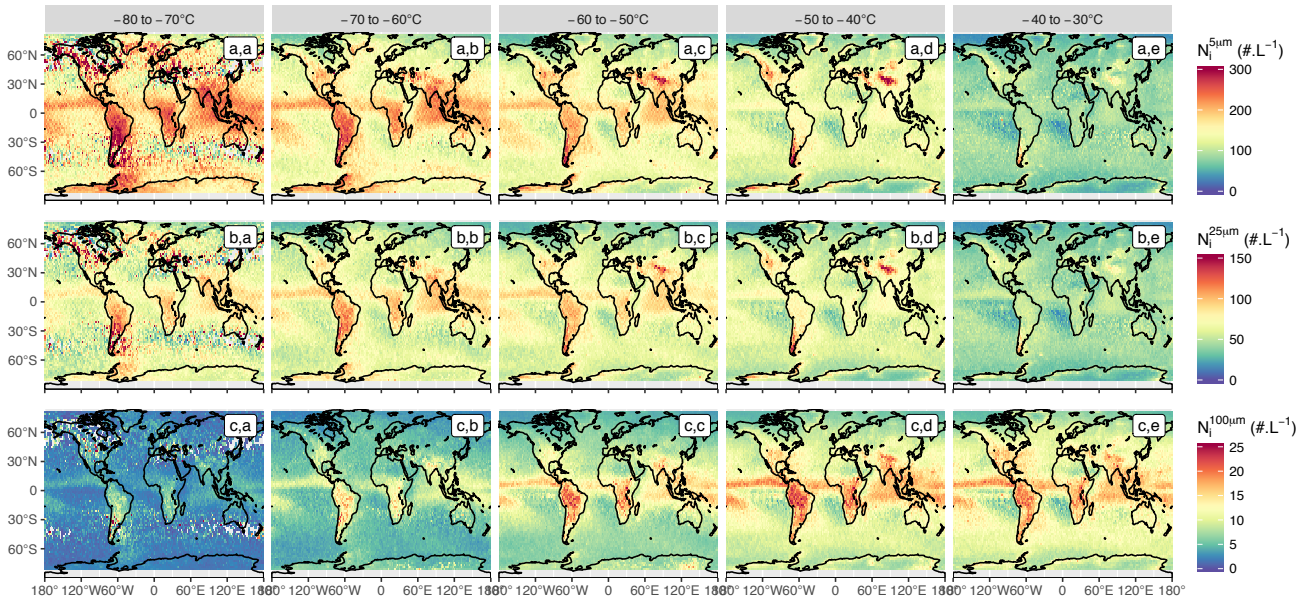


**Figure 7.** Spatial distribution of  $N_i^{5\mu\text{m}}$  (a,a-e),  $N_i^{25\mu\text{m}}$  (b,a-e) and  $N_i^{100\mu\text{m}}$  (bc,a-e) from 2006 to 2016, averaged in a  $2 \times 2^\circ$  lat-lon grid and per  $10^\circ\text{C}$  temperature bin from  $-80$  to  $-30^\circ\text{C}$ .

tropical anvils (see Fig. S8). On the contrary, maximum mean  $N_i^{5\mu\text{m}}$  values, between  $200$  and  $300\text{L}^{-1}$ , appear at very low temperatures and in deep convective regions. It can be noted that these numbers are about 2-3 times higher than the concentrations reported by Jensen et al. (2013a, 2016) for TTL cirrus, which are more consistent with the  $100\text{L}^{-1}$  that are here found in subsidence regions. This could hint at an overestimation of  $N_i^{5\mu\text{m}}$  by DARDAR-LIM at these temperatures, possibly related to the too steep increase of the concentration towards small ice crystals noted for D05 in Fig. 1 and 2. However, it is difficult based on Fig. 7 to disentangle the contributions from different cloud types or meteorological conditions to  $N_i$ , which would be required to properly compare these  $N_i$  climatologies to specific in situ measurements. This point will be further discussed in part two.

There is also a strong  $T_c$  relationship in orographic regions, but it is prominent at warmer temperatures, with a large increase in  $N_i^{5\mu\text{m}}$  being observed in the Himalayas, the Rockies, Southern Andes and the Antarctic Peninsula, as well as the edge of the East Antarctic ice sheet (Fig. 7(a,d)). These higher  $N_i^{5\mu\text{m}}$  values are typically found in the mid-latitudes, where higher windspeeds provide stronger orographic uplifts (Gryspeerd et al., 2018a). Consequently, such features are less likely in the tropics, where the atmosphere is barotropic. This is for instance clearly noted in the Andes, where no high  $N_i^{5\mu\text{m}}$  values appear at the northern end.

Similar features are seen in the distributions of  $N_i^{25\mu\text{m}}$ , with absolute values that are about 50% smaller than  $N_i^{5\mu\text{m}}$ . Maximum  $N_i^{25\mu\text{m}}$  values, found at low  $T_c$  in the tropics or in orographic regions, are therefore of about  $100\text{L}^{-1}$ . It is reminded that  $N_i^{25\mu\text{m}}$  is relatively robust to PSD shape assumptions (see sec. A3) and was found to agree well with in situ measurements for  $T_c < -60^\circ\text{C}$ . Another notable difference with  $N_i^{5\mu\text{m}}$  is the weaker temperature dependence of  $N_i^{25\mu\text{m}}$  below  $-50^\circ\text{C}$ , particularly in convective regions. This could be due to ice crystals larger than  $25\mu\text{m}$  being less directly related to homogeneous freezing events.

The spatial distribution of the  $N_i^{100\mu\text{m}}$  shown in Fig. 7(bc,a-e) is noticeably different, with a significantly reduced  $N_i^{100\mu\text{m}}$  at lower temperatures. This might be expected through the reduced efficiency of the aggregation and deposition processes needed to generate larger crystals at colder  $T_c$ , along with the size-sorting of ice crystals in cirrus clouds. At all the temperatures examined, higher  $N_i^{100\mu\text{m}}$  values are observed in convective regions, where updraughts are sufficient to transport large particles to the upper troposphere, but also where high  $N_i^{5\mu\text{m}}$  and  $N_i^{25\mu\text{m}}$  at colder temperatures subsequently lead to high  $N_i^{100\mu\text{m}}$  as the clouds mature.

~~These spatial distributions agree with recent studies showing the distribution of nucleation rates and The seasonal variability of  $N_i$  spatial distributions in the  $-60$  to  $-50^\circ\text{C}$  bin is shown in Fig. 8. Strong variations are found in the tropics and along the ITCZ, where large cloud structures are convectively driven. High  $N_i$  based on global modeling (e.g. Gasparini and Lohmann, 2016; Barahona et al., 2017)~~

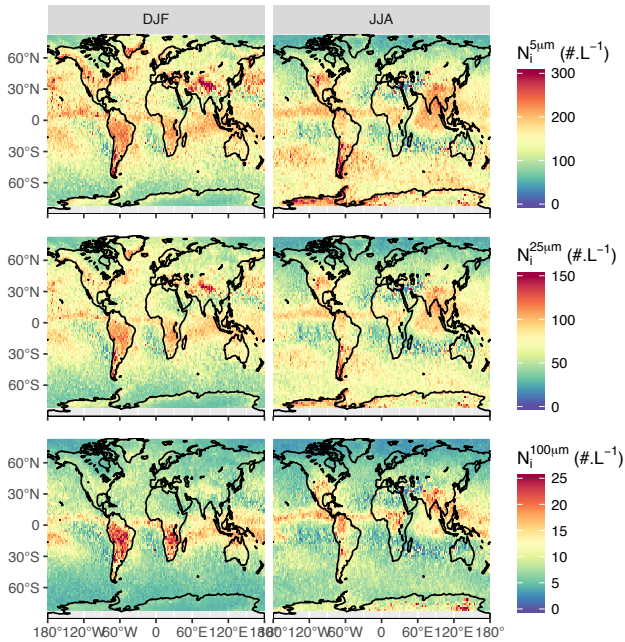


**Figure 8.** Spatial distribution in  $N_i^{5\mu\text{m}}$ ,  $N_i^{25\mu\text{m}}$  and  $N_i^{100\mu\text{m}}$  between  $-60$  and  $-50^\circ\text{C}$ , during northern hemisphere winter (DJF; a-b,a) and summer (JJA; a-b,b) seasons.

—although detailed comparisons are out of the scope of this study, values are noted in these regions during summer seasons, therefore strengthening their link to freezing events associated with deep convective structures. These values typically decrease by a factor of 2-3 during winter seasons. Inversely,  $N_i^{5\mu\text{m}}$  and  $N_i^{25\mu\text{m}}$  in the mid-latitude storm tracks and orographic regions are found to be higher during winter months, consistent with stronger jets (Gryspeerd et al., 2018a).

Comparisons of these results with recent findings by Mitchell et al. (2016, 2018) based on thermal-infrared and lidar measurements show good consistency in mid-latitude regions (increases in orographic and storm track regions). Lower absolute  $N_i$  values are found here, possibly due to the use of a  $D_{\text{min}}$  threshold. These two studies also identify a strong decrease of  $N_i$  in the tropics between  $-55^\circ\text{C}$  and  $-45^\circ\text{C}$  that do not clearly appear in Fig. 7(a,c-d). A possible explanation for this could be the different cloud sampling between the two methods. Lidar and thermal-infrared measurements indeed only provide the concentrations of thin cirrus or at cloud-top found at this temperature range, whereas Fig. 7 also indicates  $N_i$  within deep convective clouds, where high values can be expected (Paukert et al., 2017). More consistent comparisons with these studies would therefore require to look at the spatial distributions of DARDAR-LIM  $N_i$  at cloud top. These will be analysed in part two.

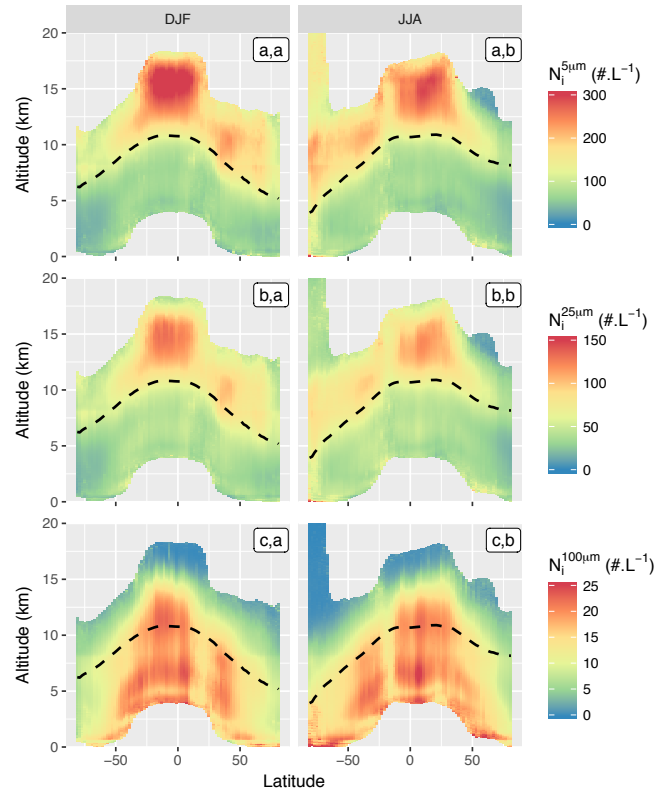


**Figure 9.** Zonal profiles of  $N_i^{5\mu\text{m}}$  (a,a-b),  $N_i^{25\mu\text{m}}$  (b,a-b) and  $N_i^{100\mu\text{m}}$  (c,c-a-b), during northern hemisphere winter (DJF; a-b,a) and summer (JJA; a-b,b) seasons. The  $-40^\circ\text{C}$  isotherm is shown as a dashed black line.

## 6.2 Zonal profile distributions

Subsets of zonal profiles distributions of  $N_i^{5\mu\text{m}}$ ,  $N_i^{25\mu\text{m}}$  and  $N_i^{100\mu\text{m}}$  corresponding to the northern hemisphere winter (DJF) and summer (JJA) seasons are presented in Fig. 9(a,a-b). Corresponding pixels counts are provided in Fig. S9.

As with the global maps in Fig. 7(a, a-e), a strong increase in  $N_i^{5\mu\text{m}}$ , a dependency between  $N_i$  and the temperature is observed. It is observed at  $T_c$  decreases. However, it is clear from these zonal plots that this relationship is not linear, as a strong increase in  $N_i^{5\mu\text{m}}$  is observed around the  $T_c = -40^\circ\text{C}$  and  $N_i^{25\mu\text{m}}$  nearly double their values upon crossing the  $-40^\circ\text{C}$  isotherm isoline (dashed line). Because homogeneous nucleation rates become significant at colder temperatures (Koop et al., 2000), this suggests that the  $N_i^{5\mu\text{m}}$  at temperatures colder than  $-40^\circ\text{C}$  is strongly influenced by homogeneous nucleation processes. This freezing. The increase in  $N_i^{5\mu\text{m}}$  is particularly strong in the tropics, where strong convective updrafts may be able to generate the high supersaturations required for homogeneous nucleation. In the mid-latitudes, the temperature dependence is stronger in the



winter hemisphere. This may indicate the role of seasonal variations in cloud or aerosol types, a subject that will be explored in more detail in part two

It is also observed that  $N_i^{25\mu\text{m}}$  and  $N_i^{5\mu\text{m}}$  to a lesser extent, decrease at very low temperatures towards the tropopause. This could indicate lower  $N_i^{25\mu\text{m}}$  and  $N_i^{100\mu\text{m}}$  at cloud top, but should be carefully considered due to the low statistical significance of retrievals in the high troposphere (see Fig. S9). This feature also appears in convective regions and could hint at lower  $N_i$  in very cold TTL cirrus by comparison to the high values found within convective structures below the freezing level. It can also be noted that the vertical structure of  $N_i^{5\mu\text{m}}$  and  $N_i^{25\mu\text{m}}$  observed here in the tropics is consistent with recent simulations of deep convective clouds by Paukert et al. (2017). Finally, it should be mentioned that the  $N_i^{5\mu\text{m}}$  values of about  $150\text{L}^{-1}$  are observed above 12 km over the Antarctic Antarctica during the winter season, possibly related to the presence of polar stratospheric clouds (Noel et al., 2008) are highly uncertain due to likely issues in the cloud mask and retrievals in this region.

Consistent with the global maps in Fig. 7(bc,a-e), there is a strong decrease in  $N_i^{100\mu\text{m}}$  with decreasing temperature. This temperature dependence is much stronger for  $T_c < -40^\circ\text{C}$ , becoming much weaker at warmer temperatures. Despite being lower than  $N_i^{5\mu\text{m}}$ , at warmer temperatures, the  $N_i^{5\mu\text{m}}N_i^{100\mu\text{m}}$  reaches values higher than  $20\text{L}^{-1}$ , such that large crystals comprise a significant fraction of the total  $N_i^{5\mu\text{m}}$  ( $50\text{-}100\text{L}^{-1}$ ). The temperature dependence will be further investigated in part 2.

## 7 Summary and conclusions

A novel approach to estimate  $N_i$  from combined CALIPSO-CloudSat measurements, called DARDAR-LIM, is here presented and evaluated against in situ measurements and in the context of a case study and a preliminary climatological analysis.

Based on over about 40 000 PSD measurements from five recent in situ campaigns, it is demonstrated that  $N_i$  can be predicted by constraining the moments of normalized PSDs using  $\beta_{\text{ext}}$  and  $Z_e$  measurements. The D05 parameterization appears capable of predicting reasonably well the measured concentration of particles from different minimum size thresholds and for ice clouds with  $T_c$  spanning from  $-90$  to  $-30^\circ\text{C}$ , demonstrating good predictions of  $N_i^{5\mu\text{m}}$ ,  $N_i^{25\mu\text{m}}$  and  $N_i^{100\mu\text{m}}$  (Fig. 2). A possible bias in  $N_i^{5\mu\text{m}}$  and  $N_i^{25\mu\text{m}}$  predictions is nevertheless noted when  $T_c \gtrsim -50^\circ\text{C}$  and is explained by a misrepresentation in D05 of the bi-modality and is observed in the measured PSDs (Fig. ??-??-1). A slight overestimation of  $N_i^{5\mu\text{m}}$  by D05, by a factor less than 2, is also noted when  $T_c < -60^\circ\text{C}$  due to its too steep representation of the concentration in particles smaller than  $25\mu\text{m}$ .  $N_i^{25\mu\text{m}}$  does

not seem significantly impacted, as it is less sensitive to PSD shape assumptions (Sec. A3).

Following these results, it is verified that  $N_i$  estimates inferred from IWC and  $N_0^*$  retrievals of DARDAR, which uses D05, are also in good agreement with the in situ measurements from co-incident flights (Fig. ??3-4). These comparisons further demonstrate the Good agreements are observed between DARDAR-LIM and co-incident D05 predictions based on the co-incident in situ measurements, thus demonstrating the sufficient sensitivity in  $\beta_{\text{ext}}$  and  $Z_e$  to constrain  $N_i$ . It is also observed that similarly good agreements are found in Observed differences between DARDAR-LIM and the in situ data are consistent with the aforementioned expectations and are explained by limited PSD shape assumptions in D05. It was noted that lidar-only and lidar-radar conditions, while more statistics are required to draw strong conclusions for estimates of  $N_i$ , are possible because, despite being associated with fewer observational constraints, they correspond to PSDs observed at cloud top or in thin cirrus that tend to follow a monomodal shape. Due to the strong bi-modality of PSDs associated with radar-only condition, retrievals, corresponding estimates of  $N_i^{5\mu\text{m}}$  and  $N_i^{25\mu\text{m}}$  are more difficult. Finally, it should be noted that these analyses of co-incident flights are only based on 2D-S measurements, which can be uncertain for sizes between 5 and  $25\mu\text{m}$ . More in situ comparisons will therefore be necessary to further evaluate  $N_i^{5\mu\text{m}}$  from DARDAR-LIM.

Reasonable physical consistency is also found in the vertical distribution of  $N_i$  estimates analysed along a short orbital track in the context of a case study representative of an occluded frontal system. Strong  $N_i^{5\mu\text{m}}$  increases are observed and  $N_i^{25\mu\text{m}}$  are found to increase below  $-40^\circ\text{C}$  (Fig. 6(ef-g)), in conformity with higher homogeneous nucleation rates. Large  $N_i^{100\mu\text{m}}$  values are found deeper in thick cloud layers. As expected, very good consistency is observed between estimates obtained in lidar-only, radar-only and lidar-radar conditions. Based on a quantitative analysis of the trajectory of two air masses, it is observed that regions that are subject to stronger updraughts and therefore supplied moisture show peaks in  $N_i^{5\mu\text{m}}$ , whereas regions representative of mature cloud parcels do not. Direct comparisons to aircraft measurements that are co-incident with the satellite track again confirm that DARDAR-LIM reproduces well the overall values and spatial variability measured in situ (Fig. ??-??).

Finally, global distributions of  $N_i^{5\mu\text{m}}$  and  $N_i^{100\mu\text{m}}$  are analysed on the basis of a 10-year climatology (Fig. 7-9). An overall increase of  $N_i^{5\mu\text{m}}$  with decreasing temperature is observed but its rate is regionally dependent. A global increase is observed as  $T_c$  reaches  $-40^\circ\text{C}$ , consistent with a strong temperature dependency of the homogeneous nucleation rate. However, steep increases when  $T_c < -50^\circ\text{C}$  are only observed in regions where uplifts are sustained by con-



vection or orography, in agreement with expectations of high sensitivity of the  $N_i$  to updraughts.

The lidar-radar  $N_i$  estimates introduced in this study thus constitute a first and very encouraging basis to provide global observational constraints of this quantity, which open the door to a better understanding of cloud processes and their evaluation in climate and numerical weather prediction models. Improvements of the method remain necessary to reduce the uncertainties related to these  $N_i$  estimates. In particular, the use of a PSD parameterization that is better fitted to retrieving  $N_i$  (i. e. with ~~This includes~~ a better representation of bi-modality ~~) should be implemented~~ and possibly a less steep increase of the concentration in small particles at low temperatures. Further comparisons to in situ measurements as well as modeling are also intended to continue to evaluation of this new  $N_i$  product. A detailed investigation of the controls on  $N_i$  based on the DARDAR-LIM dataset is presented in part two of this series.

## Appendix A: Expected uncertainties and limitations

### A1 $N_i$ under lidar- and radar-only conditions

The simultaneous use of lidar and radar observations makes DARDAR sensitive to a wide variety of ice clouds, with IWPs spanning from about  $0.01 \text{ g.m}^{-2}$  to  $5 \text{ kg.m}^{-2}$  (Sourdeval et al., 2016). Nevertheless, it should be kept in mind that the information provided by these two instruments does not always overlap, leading to lidar- and radar-only regions in the vertical profiles where cloud layers are optically very thin or thick, respectively. Fewer constraints are applied on D05 in this partial or complete absence of information from one instrument and so retrievals may be more uncertain.

Under such conditions, DARDAR relies on *a priori* information provided by an empirical relation between  $N_0^*$ ,  $\alpha_{\text{ext}}$  and the layer temperature  $T_c$  (Hogan et al., 2006). This relation is further constrained in the occurrence of lidar-radar conditions within the same column to improve the physical consistency of the *a priori* constraints (Hogan, 2007). The exact weight of these constraints on lidar- and radar-only retrievals is nevertheless difficult to quantify from the operational products only. The number of iteration is here used as a proxy to avoid any strong influence of *a priori* assumptions on the retrievals; Cloud products associated with  $n_{\text{iter}} < 2$  are excluded from this study.

Following these considerations, it can be expected that DARDAR retrievals are optimal when both lidar and radar measurements are available. However, predicting the consequence of lidar-only or radar-only conditions on  $N_i$  is not trivial. Reasonable  $N_i$  estimates should be possible in lidar-only regions due to  $\beta_{\text{ext}}$  being sensitive to small particules (to  $\mathcal{M}_2$ ), which largely contribute to  $N_i$  ( $\mathcal{M}_0$ ). PSDs observed in lidar-only conditions, i.e.

towards cloud-top, are also likely to be monomodal and therefore easier to represent for D05. Radar-only estimates may be more difficult due to  $Z_e$  being mainly sensitive to large particles (to  $\mathcal{M}_6$ ) and will therefore depend on the capability of D05 to extrapolate the concentration in small particles. These questions will be investigated and discussed throughout the manuscript (see in particular Sec. 4.2).

### A2 Propagation of DARDAR operational errors

A qualitative estimation of the errors expected on  $N_i$  can be obtained based on the uncertainties associated to DARDAR IWC and  $N_0^*$  retrievals. These account for instrumental errors and uncertainties attached to non-retrieved parameters used to simulate the lidar and radar measurements. A direct propagation of these errors on  $N_i$  can be reached from

$$\sigma_{N_i}^2 = \left(\frac{\partial N_i}{\partial \text{IWC}}\right)^2 \sigma_{\text{IWC}}^2 + \left(\frac{\partial N_i}{\partial N_0^*}\right)^2 \sigma_{N_0^*}^2$$

The variances  $\sigma_{\text{IWC}}^2$  and  $\sigma_{N_0^*}^2$  are provided in DARDAR and the partial derivatives can be solved from the equations provided in Sec. 2.2. The relative uncertainties  $\sigma_{N_i} / N_i$  typically increase from about 25% in lidar-radar conditions to 50% in lidar-only or radar-only (see Figure S2), which confirms expectations of lidar-radar estimates being more precise due to a higher information content. However, these numbers only provide rough estimates of the actual uncertainties expected on  $N_i$  as no rigorous errors are associated with non-retrieved parameters that are critical for its accuracy. For instance, the errors associated with PSD shape assumptions are only represented by fixed errors on  $\beta_{\text{ext}}$  and  $Z_e$  simulations instead of being computed from the exact sensitivity of these measurements to  $\alpha$  and  $\beta$  to the atmospheric state at each iteration.

### A3 Influence of PSD shape assumptions on $N_i$

Important uncertainties on  $N_i$  can be expected from the choice of  $\alpha$  and  $\beta$  in Eq. (4). The former parameter is especially critical as it controls the steepness of the PSD towards small particles and strongly varies depending on the dominating nucleation processes (Mitchell, 1991). The normalization approach by D05 should in principle account for such variations in the PSD shape by adjusting the scaling parameters  $N_0^*$  and  $D_w$ , but large deviations from the assumed  $\alpha$  value due to unusual conditions could still have consequences on subsequent  $N_i$  estimates. For instance, an overestimation of  $\alpha$  (i.e., a less negative  $\alpha$ ) in D05 will lead to an underestimation of  $N_i$ . This could occur in the presence of very high homogeneous nucleation rates (e.g., related strong orographic updraft) where  $\alpha$  is very negative. Reciprocally, an underestimation of  $\alpha$  is possible in case of highly dominant aggregation processes and will lead to an overestimation of  $N_i$ . The variability of  $\alpha$  and  $\beta$  between numerous airborne campaigns has been investigated by D14 in order to propose an updated version of the PSD parameterization for future DARDAR versions. Based on

the shape parameters extracted in this study, it could be estimated that uncertainties within about 50% (usually an overestimation) can reasonably be expected on  $N_i$  as results of variations from the PSD shape assumed in DARDAR (see Fig. S3 for details). Lower uncertainties should nevertheless be expected if the PSD is not too broad (i.e., in cases where homogeneous nucleation dominates) and if very small particles are discarded by a high integration threshold. Consequently,  $N_i^{25\mu\text{m}}$  is less sensitive to errors on  $\alpha$  and  $\beta$  than  $N_i^{5\mu\text{m}}$ . These numbers remain preliminary as the average  $N_0^*$  and IWC values used here may not be fully representative of each couple of  $\alpha$  and  $\beta$ . Finally, it can be noted that the coefficients chosen by D14 for future DARDAR versions, noted “all (DARDAR)” in Fig. S3, should lead to smaller  $N_i^{5\mu\text{m}}$  and  $N_i^{25\mu\text{m}}$  values due to a less negative  $\alpha$ .

~~The DARDAR product was retrieved from the ICARE data center.~~

*Data availability.* The DARDAR product was retrieved via the ICARE data center (<http://www.icare.univ-lille1.fr>) and the MODIS MYD09CMG product via the NASA Land Processes Distributed Active Archive Center (<https://e4ftl01.cr.usgs.gov>). All in situ data is available through mission-based databases and can be accessed after signing a data agreement. ACRIDICON-CHUVA and ML-CIRRUS are available via the DLR HALO database (<https://halo-db.pa.op.dlr.de>), COALESC via the MetOffice FAAM database (<http://data.ceda.ac.uk/badc/faam>), SPARTICUS via the ARM data discovery center (<https://www.archive.arm.gov/discovery/>) and ATTREX via the NASA Earth Science Project Office (<https://espoarchive.nasa.gov>).

*Acknowledgements.* The authors gratefully acknowledge the science teams involved in collecting and providing the airborne measurements used in this study. The ~~SPARTICUS and ATTREX data were respectively retrieved from the ARM data discovery center and NASA Earth Science Project Office.~~ The authors are grateful to P. Lawson and S. Woods for helpful discussions regarding the processing of 2DS and FCDP data from these two campaigns. ~~NIXE-CAPS measurements for ACRIDICON-CHUVA, COALESC and ML-CIRRUS were provided by AA and MK. The authors acknowledge the~~ NOAA Air Resources Laboratory and National Center for Atmospheric Prediction ~~is acknowledged~~ for the provision of HYSPLIT trajectories and NARR reanalyses. ~~The MODIS-MYD09CMG data product was retrieved from the online Data Pool, courtesy of the NASA Land Processes Distributed Active Archive Center (LP DAAC).~~ We are grateful to the Deutsches Klimarechenzentrum (DKRZ) for providing computational resources necessary for this study. This work was funded by the European Research Council (Grant 306284 “QUAERERE”), by the Federal Ministry for Education and Research in Germany (Bundesministerium für Bildung und Forschung, BMBF) in the “HD(CP)<sup>2</sup>” project (FKZ 01LK1210D, 01LK1503A and 01LK1505E) and by the German Research Foundation (Deutsche Forschungsgemeinschaft, DFG) in Priority Programme SPP 1294 “HALO”, project

QU 311/14-1 (“FLASH”). TG received funding from the European Union Horizon 2020 research and innovation programme under the Marie Skłodowska-Curie Grant Agreement No. 703880. EG was supported by and ~~Imperial~~ Imperial College London Junior Research Fellowship. We acknowledge support from the German Research Foundation (DFG) and Leipzig University within the program of Open Access Publishing.

## References

- Afchine, A., Rolf, C., Costa, A., Spelten, N., Riese, M., Buchholz, B., Ebert, V., Heller, R., Kaufmann, S., Minikin, A., Voigt, C., Zöger, M., Smith, J., Lawson, P., Lykov, A., Khaykin, S., and Krämer, M.: Ice particle sampling from aircraft – influence of the probing position on the ice water content, *Atmos. Meas. Tech.*, 11, 4015–4031, <https://doi.org/10.5194/amt-11-4015-2018>, 2018.
- Austin, R. T. and Stephens, G. L.: Retrieval of stratus cloud microphysical parameters using millimeter-wave radar and visible optical depth in preparation for CloudSat: 1. Algorithm formulation, *J. Geophys. Res. Atmos.*, 106, 28 233–28 242, 2001.
- Austin, R. T., Heymsfield, A. J., and Stephens, G. L.: Retrieval of ice cloud microphysical parameters using the CloudSat millimeter-wave radar and temperature, *J. Geophys. Res. Atmos.*, 114, <https://doi.org/10.1029/2008JD010049>, 2009.
- Barahona, D., Molod, A., and Kalesse, H.: Direct estimation of the global distribution of vertical velocity within cirrus clouds, *Scientific Reports*, 7, 6840, <https://doi.org/10.1038/s41598-017-07038-6>, 2017.
- Baran, A. J.: A review of the light scattering properties of cirrus, *J. Quant. Spectrosc. Radiat. Transfer*, 110, 1239–1260, <https://doi.org/10.1016/j.jqsrt.2009.02.026>, 2009.
- Battaglia, A. and Delanoë, J.: Synergies and complementarities of CloudSat-CALIPSO snow observations, *J. Geophys. Res. Atmos.*, 118, 721–731, <https://doi.org/10.1029/2012JD018092>, 2013.
- Benedetti, A., Stephens, G. L., and Haynes, J. M.: Ice cloud microphysics retrievals from millimeter radar and visible optical depth using an estimation theory approach, *J. Geophys. Res. Atmos.*, 108, 2156–2202, <https://doi.org/10.1029/2002JD002693>, 2003.
- Bennartz, R. and Rausch, J.: Global and regional estimates of warm cloud droplet number concentration based on 13 years of AQUA-MODIS observations, *Atmos. Chem. Phys.*, 17, 9815–9836, 2017.
- Boers, R., Acarreta, J. R., and Gras, J. L.: Satellite monitoring of the first indirect aerosol effect: Retrieval of the droplet concentration of water clouds, *J. Geophys. Res. Atmos.*, 111, 2156–2202, 2006.
- Boucher, O., Randall, D., Artaxo, P., Bretherton, C., Feingold, G., Forster, P., Kerminen, V.-M., Kondo, Y., Liao, H., Lohmann, U., Rasch, P., Satheesh, S., Sherwood, S., Stevens, B., and Zhang, X.: Clouds and Aerosols, in: *Climate Change 2013: The Physical Science Basis. Contribution of Working Group I to the Fifth Assessment Report of the Intergovernmental Panel on Climate Change*, edited by Stocker, T., Qin, D., Plattner, G.-K., Tignor, M., Allen, S., Boschung, J., Nauels, A., Xia, Y., Bex, V., and Midgley, P., 10.1017/CBO9781107415324.016, Cambridge University Press, Cambridge, United Kingdom and New York, NY, USA, 2013.

- Brenguier, J.-L., Pawlowska, H., Schüller, L., Preusker, R., Fischer, J., and Fouquart, Y.: Radiative Properties of Boundary Layer Clouds: Droplet Effective Radius versus Number Concentration, *J. Atmos. Sci.*, 57, 803–821, 2000.
- 5 Brown, P. R. A. and Francis, P. N.: Improved Measurements of the Ice Water Content in Cirrus Using a Total-Water Probe, *J. Atmos. Oceanic Technol.*, 12, 410–414, 1995.
- Ceccaldi, M., Delanoë, J., Hogan, R. J., Pounder, N. L., Protat, A., and Pelon, J.: From CloudSat-CALIPSO to EarthCare: Evolution of the DARDAR cloud classification and its comparison to airborne radar-lidar observations, *J. Geophys. Res. Atmos.*, 118, 7962–7981, <https://doi.org/10.1002/jgrd.50579>, 2013.
- 10 Comstock, J. M., Lin, R.-F., Starr, D. O., and Yang, P.: Understanding ice supersaturation, particle growth, and number concentration in cirrus clouds, *J. Geophys. Res. Atmos.*, 113, <https://doi.org/10.1029/2008JD010332>, 2008.
- Costa, A., Meyer, J., Afchine, A., Luebke, A., Günther, G., Dorsey, J. R., Gallagher, M. W., Ehrlich, A., Wendisch, M., Baumgardner, D., Wex, H., and Krämer, M.: Classification of Arctic, Mid-Latitude and Tropical Clouds in the Mixed-Phase Temperature Regime, *Atmos. Chem. Phys. Discuss.*, 2017, 1–40, <https://doi.org/10.5194/acp-2017-226>, 2017.
- Delanoë, J. and Hogan, R. J.: A variational scheme for retrieving ice cloud properties from combined radar, lidar, and infrared radiometer, *J. Geophys. Res. Atmos.*, 113, <https://doi.org/10.1029/2007JD009000>, 2008.
- Delanoë, J. and Hogan, R. J.: Combined CloudSat-CALIPSO-MODIS retrievals of the properties of ice clouds, *J. Geophys. Res. Atmos.*, 115, <https://doi.org/10.1029/2009JD012346>, 2010.
- 30 Delanoë, J., Protat, A., Testud, J., Bouniol, D., Heymsfield, A. J., Bansemer, A., Brown, P. R. A., and Forbes, R. M.: Statistical properties of the normalized ice particle size distribution, *J. Geophys. Res. Atmos.*, 110, <https://doi.org/10.1029/2004JD005405>, 2005.
- 35 Delanoë, J., Heymsfield, A. J., Protat, A., Bansemer, A., and Hogan, R. J.: Normalized particle size distribution for remote sensing application, *J. Geophys. Res.*, 119, 4204–4227, <https://doi.org/10.1002/2013JD020700>, 2014.
- Deng, M., Mace, G. G., Wang, Z., and Okamoto, H.: Tropical Composition, Cloud and Climate Coupling Experiment validation for cirrus cloud profiling retrieval using CloudSat radar and CALIPSO lidar, *J. Geophys. Res. Atmos.*, 115, <https://doi.org/10.1029/2009JD013104>, 2010.
- 40 Deng, M., Mace, G. G., Wang, Z., and Lawson, R. P.: Evaluation of Several A-Train Ice Cloud Retrieval Products with In Situ Measurements Collected during the SPARTICUS Campaign, *J. Appl. Meteor. and Clim.*, 52, 1014–1030, <https://doi.org/10.1175/JAMC-D-12-054.1>, 2012.
- Eliasson, S., Buehler, S. A., Milz, M., Eriksson, P., and John, V. O.: Assessing observed and modelled spatial distributions of ice water path using satellite data, *Atmos. Chem. Phys.*, 11, 375–391, <https://doi.org/10.5194/acp-11-375-2011>, 2011.
- Erfani, E. and Mitchell, D. L.: Developing and bounding ice particle mass- and area-dimension expressions for use in atmospheric models and remote sensing, *Atmos. Chem. Phys.*, 16, 4379–4400, <https://doi.org/10.5194/acp-16-4379-2016>, 2016.
- 55 Farrington, R. J., Connolly, P. J., Lloyd, G., Bower, K. N., Flynn, M. J., Gallagher, M. W., Field, P. R., Dearden, C., and Choullarton, T. W.: Comparing model and measured ice crystal concentrations in orographic clouds during the INUPIAQ campaign, *Atmos. Chem. Phys.*, 16, 4945–4966, <https://doi.org/10.5194/acp-16-4945-2016>, 2016.
- Feofilov, A. G., Stubenrauch, C. J., and Delanoë, J.: Ice water content vertical profiles of high-level clouds: classification and impact on radiative fluxes, *Atmos. Chem. Phys.*, 15, 12 327–12 344, <https://doi.org/10.5194/acpd-15-16325-2015>, 2015.
- 65 Field, P. R., Wood, R., Brown, P. R. A., Kaye, P. H., Hirst, E., Greenaway, R., and Smith, J. A.: Ice Particle Interarrival Times Measured with a Fast FSSP, *J. Atmos. Oceanic Technol.*, 20, 249–261, [https://doi.org/10.1175/1520-0426\(2003\)020<0249:IPITMW>2.0.CO;2](https://doi.org/10.1175/1520-0426(2003)020<0249:IPITMW>2.0.CO;2), 2003.
- Field, P. R., Hogan, R. J., Brown, P. R. A., Illingworth, A. J., Choullarton, T. W., and Cotton, R. J.: Parametrization of ice-particle size distributions for mid-latitude stratiform cloud, *Quart. J. Roy. Meteor. Soc.*, 131, 1997–2017, <https://doi.org/10.1256/qj.04.134>, 2005.
- 75 Field, P. R., Heymsfield, A. J., and Bansemer, A.: Shattering and Particle Interarrival Times Measured by Optical Array Probes in Ice Clouds, *J. Atmos. Oceanic Technol.*, 23, 1357–1371, <https://doi.org/10.1175/JTECH1922.1>, 2006.
- Gasparini, B. and Lohmann, U.: Why cirrus cloud seeding cannot substantially cool the planet, *J. Geophys. Res. Atmos.*, 121, 4877–4893, <https://doi.org/10.1002/2015JD024666>, 2016.
- Gong, J. and Wu, D. L.: CloudSat-constrained cloud ice water path and cloud top height retrievals from MHS 157 and 183.3 GHz radiances, *Atmos. Meas. Tech.*, 7, 1873–1890, <https://doi.org/10.5194/amt-7-1873-2014>, 2014.
- Grosvenor, D. P., Sourdeval, O., Zuidema, P., Ackerman, A. S., Alexandrov, M. D., Bennartz, R., Boers, R., Cairns, B., Chiu, C., Christensen, M., Deneke, H., Diamond, M., Feingold, G., Fridlind, A., Hünerbein, A., Knist, C., Kollias, P., Marshak, A., McCoy, D., Merk, D., Painemal, D., Rausch, J., Rosenfeld, D., Russchenberg, H., Seifert, P., Sinclair, K., Stier, P., van Diedenhoven, B., Wendisch, M., Werner, F., Wood, R., Zhang, Z., and Quaas, J.: Remote sensing of droplet number concentration in warm clouds: A review of the current state of knowledge and perspectives, *Reviews of Geophysics*, 56, <https://doi.org/10.1029/2017RG000593>, 2018.
- 90 Gryspeerdt, E., Quaas, J., and Bellouin, N.: Constraining the aerosol influence on cloud fraction, *J. Geophys. Res. Atmos.*, 121, 3566–3583, <https://doi.org/10.1002/2015JD023744>, <http://dx.doi.org/10.1002/2015JD023744>, 2016.
- Gryspeerdt, E., Quaas, J., Goren, T., Klocke, D., and Brueck, M.: An automated cirrus classification, *Atmos. Chem. Phys.*, 18, 6157–6169, <https://doi.org/10.5194/acp-18-6157-2018>, 2018a.
- 105 Gryspeerdt, E., Sourdeval, O., Quaas, J., Delanoë, J., and Kühne, P.: Ice crystal number concentration estimates from lidar-radar satellite retrievals. Part 2: Controls on the ice crystal number concentration, *Atmos. Chem. Phys. Discuss.*, 2018, 1–25, <https://doi.org/10.5194/acp-2018-21>, 2018b.
- 110 Guignard, A., Stubenrauch, C. J., Baran, A. J., and Armante, R.: Bulk microphysical properties of semi-transparent cirrus from AIRS: a six year global climatology and statistical analysis in synergy with geometrical profiling data from CloudSat-CALIPSO, *Atmos. Chem. Phys.*, 12, 503–525, <https://doi.org/10.5194/acp-12-503-2012>, 2012.
- Gurganus, C. and Lawson, P.: Laboratory and Flight Tests of 2D Imaging Probes: Toward a Better Understanding of Instru-

- ment Performance and the Impact on Archived Data, *J. Atmos. Oceanic Technol.*, 0, <https://doi.org/10.1175/JTECH-D-17-0202.1>, 2018.
- Han, Q., Rossow, W. B., Chou, J., and Welch, R. M.: Global variation of column droplet concentration in low-level clouds, *Geophys. Res. Lett.*, 25, 1419–1422, <https://doi.org/10.1029/98GL01095>, 1998.
- Han, Q., Rossow, W. B., Zeng, J., and Welch, R.: Three Different Behaviors of Liquid Water Path of Water Clouds in Aerosol–Cloud Interactions, *J. Atmos. Sci.*, 59, 726–735, [https://doi.org/10.1175/1520-0469\(2002\)059<0726:TDBOLW>2.0.CO;2](https://doi.org/10.1175/1520-0469(2002)059<0726:TDBOLW>2.0.CO;2), 2002.
- Hendricks, J., Kärcher, B., and Lohmann, U.: Effects of ice nuclei on cirrus clouds in a global climate model, *J. Geophys. Res. Atmos.*, 116, <https://doi.org/10.1029/2010JD015302>, 2011.
- Heyn, I., Block, K., Mülmenstädt, J., Gryspeerdt, E., Kühne, P., Salzmann, M., and Quaas, J.: Assessment of simulated aerosol effective radiative forcings in the terrestrial spectrum, *Geophys. Res. Lett.*, 44, 1001–1007, <https://doi.org/10.1002/2016GL071975>, 2017.
- Hogan, R. J.: A Variational Scheme for Retrieving Rainfall Rate and Hail Reflectivity Fraction from Polarization Radar, *J. Appl. Meteor. and Clim.*, 46, 1544–1564, <https://doi.org/10.1175/JAM2550.1>, 2007.
- Hogan, R. J., Mittermaier, M. P., and Illingworth, A. J.: The Retrieval of Ice Water Content from Radar Reflectivity Factor and Temperature and Its Use in Evaluating a Mesoscale Model, *J. Appl. Meteor. and Clim.*, 45, 301–317, <https://doi.org/10.1175/JAM2340.1>, 2006.
- Holl, G., Eliasson, S., Mendorok, J., and Buehler, S. A.: SPARE-ICE: Synergistic ice water path from passive operational sensors, *J. Geophys. Res. Atmos.*, 119, 1504–1523, <https://doi.org/10.1002/2013JD020759>, 2014.
- Ickes, L., Welti, A., Hoose, C., and Lohmann, U.: Classical nucleation theory of homogeneous freezing of water: thermodynamic and kinetic parameters, *Atmos. Chem. Phys.*, 17, 5514–5537, <https://doi.org/10.1039/C4CP04184D>, 2015.
- Inoue, T.: On the temperature and effective emissivity determination of semi-transparent cirrus clouds by bi-spectral measurements in the 10  $\mu\text{m}$  window region, *J. Meteor. Soc. Japan*, 63, 88–98, [https://doi.org/10.2151/jmsj1965.63.1\\_88](https://doi.org/10.2151/jmsj1965.63.1_88), 1985.
- Jackson, R. C., McFarquhar, G. M., Fridlind, A. M., and Atlas, R.: The dependence of cirrus gamma size distributions expressed as volumes in  $N_0$ - $\lambda$ - $\mu$  phase space and bulk cloud properties on environmental conditions: Results from the Small Ice Particles in Cirrus Experiment (SPARTICUS), *Journal of Geophysical Research: Atmospheres*, 120, 10,351–10,377, <https://doi.org/10.1002/2015JD023492>, 2015.
- Jensen, E. J., Toon, O. B., Westphal, D. L., Kinne, S., and Heymsfield, A. J.: Microphysical modeling of cirrus: 1. Comparison with 1986 FIRE IFO measurements, *J. Geophys. Res. Atmos.*, 99, 10 421–10 442, <https://doi.org/10.1029/93JD02334>, 1994.
- Jensen, E. J., Diskin, G., Lawson, R. P., Lance, S., Bui, T. P., Hlavka, D., McGill, M., Pfister, L., Toon, O. B., and Gao, R.: Ice nucleation and dehydration in the Tropical Tropopause Layer, *Proceedings of the National Academy of Sciences*, 110, 2041–2046, <https://doi.org/10.1073/pnas.1217104110>, 2013a.
- Jensen, E. J., Lawson, R. P., Bergman, J. W., Pfister, L., Bui, T. P., and Schmitt, C. G.: Physical processes controlling ice concentrations in synoptically forced, midlatitude cirrus, *Journal of Geophysical Research: Atmospheres*, 118, 5348–5360, <https://doi.org/10.1002/jgrd.50421>, <http://dx.doi.org/10.1002/jgrd.50421>, 2013b.
- Jensen, E. J., Pfister, L., Jordan, D. E., Bui, T. V., Ueyama, R., Singh, H. B., Thornberry, T., Rollins, A. W., Gao, R.-S., Fahey, D. W., Rosenlof, K. H., Elkins, J. W., Diskin, G. S., DiGangi, J. P., Lawson, R. P., Woods, S., Atlas, E. L., Navarro Rodriguez, M. A., Wofsy, S. C., Pittman, J., Bardeen, C. G., Toon, O. B., Kindel, B. C., Newman, P. A., McGill, M. J., Hlavka, D. L., Lait, L. R., Schoeberl, M. R., Bergman, J. W., Selkirk, H. B., Alexander, M. J., Kim, J.-E., Lim, B. H., Stutz, J., and Pfeilsticker, K.: The NASA Airborne Tropical Tropopause Experiment (ATTREX): High-Altitude Aircraft Measurements in the Tropical Western Pacific, *Bull. Amer. Meteor. Soc.*, 98, 129–143, <https://doi.org/10.1175/BAMS-D-14-00263.1>, 2015.
- Jensen, E. J., Ueyama, R., Pfister, L., Bui, T. V., Lawson, R. P., Woods, S., Thornberry, T., Rollins, A. W., Diskin, G. S., DiGangi, J. P., and Avery, M. A.: On the Susceptibility of Cold Tropical Cirrus to Ice Nuclei Abundance, *J. Atmos. Sci.*, 73, 2445–2464, <https://doi.org/10.1175/JAS-D-15-0274.1>, 2016.
- Kärcher, B. and Lohmann, U.: A parameterization of cirrus cloud formation: Homogeneous freezing of supercooled aerosols, *J. Geophys. Res. Atmos.*, 107, <https://doi.org/10.1029/2001JD000470>, 2002.
- Kärcher, B. and Lohmann, U.: A parameterization of cirrus cloud formation: Heterogeneous freezing, *J. Geophys. Res. Atmos.*, 108, <https://doi.org/10.1029/2002JD003220>, 2003.
- Kärcher, B. and Ström, J.: The roles of dynamical variability and aerosols in cirrus cloud formation, *Atmos. Chem. Phys.*, 3, 823–838, <https://doi.org/10.5194/acp-3-823-2003>, 2003.
- Kärcher, B., Hendricks, J., and Lohmann, U.: Physically based parameterization of cirrus cloud formation for use in global atmospheric models, *J. Geophys. Res. Atmos.*, 111, <https://doi.org/10.1029/2005JD006219>, 2006.
- Kay, J. E. and Wood, R.: Timescale analysis of aerosol sensitivity during homogeneous freezing and implications for upper tropospheric water vapor budgets, *Geophys. Res. Lett.*, 35, <https://doi.org/10.1029/2007GL032628>, 2008.
- Khain, A., Ovchinnikov, M., Pinsky, M., Pokrovsky, A., and Krugliak, H.: Notes on the state-of-the-art numerical modeling of cloud microphysics, *Atmos. Res.*, 55, 159 – 224, [https://doi.org/10.1016/S0169-8095\(00\)00064-8](https://doi.org/10.1016/S0169-8095(00)00064-8), 2000.
- King, M. D., Tsay, S. C., Platnick, S., Wang, M., and Liou, K. N.: Cloud Retrieval Algorithms for MODIS: Optical Thickness, Effective Particle Radius, and Thermodynamic Phase., *Algorithm Theor. Basis Doc. ATBD-MOD-05*, NASA Goddard Space Flight Cent., Greenbelt, Md., 1998.
- Koop, T., Luo, B., Tsias, A., and Peter, T.: Water activity as the determinant for homogeneous ice nucleation in aqueous solutions, *Nature*, 406, 611–614, <https://doi.org/10.1038/35020537>, 2000.
- Korolev, A.: Reconstruction of the Sizes of Spherical Particles from Their Shadow Images. Part I: Theoretical Considerations, *J. Atmos. Oceanic Technol.*, 24, 376–389, <https://doi.org/10.1175/JTECH1980.1>, 2007.
- Korolev, A. and Field, P. R.: Assessment of the performance of the inter-arrival time algorithm to identify ice shattering artifacts in cloud particle probe measurements, *Atmos. Meas. Tech.*, 8, 761–777, <https://doi.org/10.5194/amt-8-761-2015>, 2015.

- Korolev, A., Emery, E. F., Strapp, J. W., Cober, S. G., Isaac, G. A., Wasey, M., and Marcotte, D.: Small Ice Particles in Tropospheric Clouds: Fact or Artifact? Airborne Icing Instrumentation Evaluation Experiment, *Bull. Amer. Meteorol. Soc.*, 92, 967–973, <https://doi.org/10.1175/2010BAMS3141.1>, 2011.
- Korolev, A. V., Emery, E. F., Strapp, J. W., Cober, S. G., and Isaac, G. A.: Quantification of the Effects of Shattering on Airborne Ice Particle Measurements, *Journal of Atmospheric and Oceanic Technology*, 30, 2527–2553, <https://doi.org/10.1175/JTECH-D-13-00115.1>, <https://doi.org/10.1175/JTECH-D-13-00115.1>, 2013.
- Krämer, M., Rolf, C., Luebke, A., Afchine, A., Spelten, N., Costa, A., Meyer, J., Zöger, M., Smith, J., Herman, R. L., Buchholz, B., Ebert, V., Baumgardner, D., Borrmann, S., Klingebiel, M., and Avallone, L.: A microphysics guide to cirrus clouds – Part I: Cirrus types, *Atmos. Chem. Phys.*, 16, 3463–3483, <https://doi.org/10.5194/acp-16-3463-2016>, 2016.
- Lawson, R. P.: Effects of ice particles shattering on the 2D-S probe, *Atmos. Meas. Tech.*, 4, 1361–1381, <https://doi.org/10.5194/amt-4-1361-2011>, <http://www.atmos-meas-tech.net/4/1361/2011/>, 2011.
- Lawson, R. P., O'Connor, D., Zmarzly, P., Weaver, K., Baker, B., Mo, Q., and Jonsson, H.: The 2D-S (Stereo) Probe: Design and Preliminary Tests of a New Airborne, High-Speed, High-Resolution Particle Imaging Probe, *J. Atmos. Oceanic Technol.*, 23, 1462–1477, <https://doi.org/10.1175/JTECH1927.1>, 2006.
- Liou, K.: Influence of cirrus clouds on weather and climate processes: A global perspective, *Mon. Wea. Rev.*, 114, 1167–1199, [https://doi.org/10.1175/1520-0493\(1986\)114<1167:IOCCOW>2.0.CO;2](https://doi.org/10.1175/1520-0493(1986)114<1167:IOCCOW>2.0.CO;2), 1986.
- Lohmann, U., Quaas, J., Kinne, S., and Feichter, J.: Different Approaches for Constraining Global Climate Models of the Anthropogenic Indirect Aerosol Effect, *Bull. Amer. Meteor. Soc.*, 88, 243–249, <https://doi.org/10.1175/BAMS-88-2-243>, 2007.
- Luebke, A. E., Afchine, A., Costa, A., Grooß, J.-U., Meyer, J., Rolf, C., Spelten, N., Avallone, L. M., Baumgardner, D., and Krämer, M.: The origin of midlatitude ice clouds and the resulting influence on their microphysical properties, *Atmos. Chem. Phys.*, 16, 5793–5809, <https://doi.org/10.5194/acp-16-5793-2016>, 2016.
- Mace, J., Jensen, E., McFarquhar, G., Comstock, J., Ackerman, T., Mitchell, D., Liu, X., and Garrett, T.: SPARTICus: Small Particles In Cirrus science and operations plan, Tech. rep., ARM, Available at <https://www.arm.gov/publications/programdocs/doe-sc-arm-10-003.pdf>, 2009.
- Massie, S. T., Delanoë, J., Bardeen, C. G., Jiang, J. H., and Huang, L.: Changes in the shape of cloud ice water content vertical structure due to aerosol variations, *Atmos. Chem. Phys.*, 16, 6091–6105, <https://doi.org/10.5194/acp-16-6091-2016>, 2016.
- McFarquhar, G. M., Um, J., Freer, M., Baumgardner, D., Kok, G. L., and Mace, G.: Importance of small ice crystals to cirrus properties: Observations from the Tropical Warm Pool International Cloud Experiment (TWP-ICE), *Geophysical Research Letters*, 34, <https://doi.org/10.1029/2007GL029865>, 2007.
- Mesinger, F., DiMego, G., Kalnay, E., Mitchell, K., Shafran, P. C., Ebisuzaki, W., Jović, D., Woollen, J., Rogers, E., Berbery, E. H., Ek, M. B., Fan, Y., Grumbine, R., Higgins, W., Li, H., Lin, Y., Manikin, G., Parrish, D., and Shi, W.: North American Regional Reanalysis, *Bull. Amer. Meteor. Soc.*, 87, 343–360, <https://doi.org/10.1175/BAMS-87-3-343>, 2006.
- Meyer, J.: Ice Crystal Measurements with the New Particle Spectrometer NIXE-CAPS, Ph.D. thesis, Schriften des Forschungszentrum Jülich, Reihe Energie und Umwelt, 2012.
- Mishra, S., Mitchell, D. L., Turner, D. D., and Lawson, R. P.: Parameterization of ice fall speeds in midlatitude cirrus: Results from SPARTICus, *J. Geophys. Res. Atmos.*, 119, 3857–3876, <https://doi.org/10.1002/2013JD020602>, 2014.
- Mitchell, D., Mishra, S., and Lawson, P.: Cirrus Clouds and Climate Engineering: New Findings on Ice Nucleation and Theoretical Basis, in: *Planet Earth 2011 - Global Warming Challenges and Opportunities for Policy and Practice*, edited by Carayannis, E., InTech, <https://doi.org/10.5772/24664>, 2011.
- Mitchell, D. L.: Evolution of Snow-Size Spectra in Cyclonic Storms. Part II: Deviations from the Exponential Form, *J. Atmos. Sci.*, 48, 1885–1899, [https://doi.org/10.1175/1520-0469\(1991\)048<1885:EOSSSI>2.0.CO;2](https://doi.org/10.1175/1520-0469(1991)048<1885:EOSSSI>2.0.CO;2), 1991.
- Mitchell, D. L.: Use of Mass- and Area-Dimensional Power Laws for Determining Precipitation Particle Terminal Velocities, *J. Atmos. Sci.*, 53, 1710–1723, [https://doi.org/10.1175/1520-0469\(1996\)053<1710:UOMAAD>2.0.CO;2](https://doi.org/10.1175/1520-0469(1996)053<1710:UOMAAD>2.0.CO;2), 1996.
- Mitchell, D. L., d'Entremont, R. P., and Lawson, R. P.: Inferring Cirrus Size Distributions through Satellite Remote Sensing and Microphysical Databases, *J. Atmos. Sci.*, 67, 1106–1125, <https://doi.org/10.1175/2009JAS3150.1>, 2010.
- Mitchell, D. L., Garnier, A., Avery, M., and Erfani, E.: CALIPSO observations of the dependence of homo- and heterogeneous ice nucleation in cirrus clouds on latitude, season and surface condition, *Atmos. Chem. Phys. Discuss.*, 2016, 1–60, <https://doi.org/10.5194/acp-2016-1062>, 2016.
- Mitchell, D. L., Garnier, A., Pelon, J., and Erfani, E.: CALIPSO (IIR-CALIOP) Retrievals of Cirrus Cloud Ice Particle Concentrations, *Atmospheric Chemistry and Physics Discussions*, 2018, 1–60, <https://doi.org/10.5194/acp-2018-526>, 2018.
- Nakajima, T. and King, M. D.: Determination of the Optical Thickness and Effective Particle Radius of Clouds from Reflected Solar Radiation Measurements. Part I: Theory, *J. Atmos. Sci.*, 47, 1878–1893, <https://doi.org/10.1175/1520-0469.1990>, 1990.
- Noel, V., Hertzog, A., Chepfer, H., and Winker, D. M.: Polar stratospheric clouds over Antarctica from the CALIPSO spaceborne lidar, *J. Geophys. Res. Atmos.*, 113, <https://doi.org/10.1029/2007JD008616>, 2008.
- Osborne, S. R., Abel, S. J., Boutle, I. A., and Marenco, F.: Evolution of Stratocumulus Over Land: Comparison of Ground and Aircraft Observations with Numerical Weather Prediction Simulations, *Boundary-Layer Meteorology*, 153, 165–193, <https://doi.org/10.1007/s10546-014-9944-0>, 2014.
- Painemal, D. and Zuidema, P.: Assessment of MODIS cloud effective radius and optical thickness retrievals over the Southeast Pacific with VOCALS-REX in situ measurements, *J. Geophys. Res. Atmos.*, 116, <https://doi.org/10.1029/2011JD016155>, 2011.
- Paukert, M., Hoose, C., and Simmel, M.: Redistribution of ice nuclei between cloud and rain droplets: Parameterization and application to deep convective clouds, *J. Adv. Model. Earth Sy.*, 9, 514–535, <https://doi.org/10.1002/2016MS000841>, 2017.
- Protat, A., Delanoë, J., O'Connor, E. J., and L'Ecuyer, T. S.: The Evaluation of CloudSat and CALIPSO Ice Microphysical Products Using Ground-Based Cloud Radar and Lidar Observations, *J. Atmos. Oceanic Technol.*, 27, 793–810, <https://doi.org/10.1175/2009JTECHA1397.1>, 2010.

- Protat, A., Young, S. A., McFarlane, S. A., L'Ecuyer, T., Mace, G. G., Comstock, J. M., Long, C. N., Berry, E., and Delanoë, J.: Reconciling Ground-Based and Space-Based Estimates of the Frequency of Occurrence and Radiative Effect of Clouds around Darwin, Australia, *J. Appl. Meteor. and Clim.*, 53, 456–478, <https://doi.org/10.1175/JAMC-D-13-072.1>, 2014.
- Quaas, J., Boucher, O., and Lohmann, U.: Constraining the total aerosol indirect effect in the LMDZ and ECHAM4 GCMs using MODIS satellite data, *Atmos. Chem. Phys.*, 6, 947–955, <https://doi.org/10.5194/acp-6-947-2006>, 2006.
- Quaas, J., Boucher, O., Bellouin, N., and Kinne, S.: Satellite-based estimate of the direct and indirect aerosol climate forcing, *J. Geophys. Res. Atmos.*, 113, <https://doi.org/10.1029/2007JD008962>, 2008.
- Schmid, B., Tomlinson, J. M., Hubbe, J. M., Comstock, J. M., Mei, F., Chand, D., Pekour, M. S., Kluzek, C. D., Andrews, E., Biraud, S. C., and McFarquhar, G. M.: The DOE ARM Aerial Facility, *Bull. Amer. Meteor. Soc.*, 95, 723–742, <https://doi.org/10.1175/BAMS-D-13-00040.1>, 2013.
- Seifert, A. and Beheng, K. D.: A two-moment cloud microphysics parameterization for mixed-phase clouds. Part 1: Model description, *Meteor. Atmos. Phys.*, 92, 45–66, <https://doi.org/10.1007/s00703-005-0112-4>, 2006.
- Sourdeval, O., Labonnote, L. C., Brogniez, G., Jourdan, O., Pelon, J., and Garnier, A.: A variational approach for retrieving ice cloud properties from infrared measurements: application in the context of two IIR validation campaigns, *Atmos. Chem. Phys.*, 13, 8229–8244, <https://doi.org/10.5194/acp-13-8229-2013>, 2013.
- Sourdeval, O., C. Labonnote, L., Baran, A. J., and Brogniez, G.: A methodology for simultaneous retrieval of ice and liquid water cloud properties. Part I: Information content and case study, *Quart. J. Roy. Meteor. Soc.*, 141, 870–882, <https://doi.org/10.1002/qj.2405>, 2015.
- Sourdeval, O., C. Labonnote, L., Baran, A. J., Mülmenstädt, J., and Brogniez, G.: A methodology for simultaneous retrieval of ice and liquid water cloud properties. Part 2: Near-global retrievals and evaluation against A-Train products, *Quart. J. Roy. Meteor. Soc.*, 142, 3063–3081, <https://doi.org/10.1002/qj.2889>, 2016.
- Stein, A. F., Draxler, R. R., Rolph, G. D., Stunder, B. J. B., Cohen, M. D., and Ngan, F.: NOAA's HYSPLIT Atmospheric Transport and Dispersion Modeling System, *Bull. Amer. Meteor. Soc.*, 96, 2059–2077, <https://doi.org/10.1175/BAMS-D-14-00110.1>, 2015.
- Stephens, G. L.: Cloud Feedbacks in the Climate System: A Critical Review, *J. Clim.*, 18, 237–273, <https://doi.org/10.1175/JCLI-3243.1>, 2005.
- Stephens, G. L., Tsay, S.-C., Stackhouse, P. W., and Flatau, P. J.: The Relevance of the Microphysical and Radiative Properties of Cirrus Clouds to Climate and Climatic Feedback, *Journal of the Atmospheric Sciences*, 47, 1742–1754, 1990.
- Stephens, G. L., Vane, D. G., Boain, R. J., Mace, G. G., Sassen, K., Wang, Z., Illingworth, A. J., O'Connor, E. J., Rossow, W. B., Durden, S. L., Miller, S. D., Austin, R. T., Benedetti, A., Mitrescu, C., and CloudSat Science Team, T.: The CLOUDSAT Mission and the A-Train, *Bull. Amer. Meteor. Soc.*, 83, 1771–1790, <https://doi.org/10.1175/BAMS-83-12-1771>, 2002.
- Thornberry, T. D., Rollins, A. W., Avery, M. A., Woods, S., Lawson, R. P., Bui, T. V., and Gao, R.-S.: Ice water content-extinction relationships and effective diameter for TTL cirrus derived from in situ measurements during ATTREX 2014, *J. Geophys. Res. Atmos.*, 122, 4494–4507, <https://doi.org/10.1002/2016JD025948>, 2017.
- Vaughan, M., Powell, K., Kuehn, R., Young, S., Winker, D., Hostetler, C., Hunt, W., Liu, Z., McGill, M., and Getzewich, B.: Fully Automated Detection of Cloud and Aerosol Layers in the CALIPSO Lidar Measurements, *J. Atmos. Oceanic Technol.*, 26, 2034–2050, <https://doi.org/10.1175/2009JTECHA1228.1>, 2009.
- Voigt, C., Schumann, U., Minikin, A., Abdelmonem, A., Afchine, A., Borrmann, S., Boettcher, M., Buchholz, B., Bugliaro, L., Costa, A., Curtius, J., Dollner, M., Dörnbrack, A., Dreiling, V., Ebert, V., Ehrlich, A., Fix, A., Forster, L., Frank, F., Fütterer, D., Giez, A., Graf, K., Groöß, J.-U., Groß, S., Heimerl, K., Heinold, B., Hüneke, T., Järvinen, E., Jurkat, T., Kaufmann, S., Kenntner, M., Klingebiel, M., Klimach, T., Kohl, R., Krämer, M., Krisna, T. C., Luebke, A., Mayer, B., Mertes, S., Molleker, S., Petzold, A., Pfeilsticker, K., Port, M., Rapp, M., Reutter, P., Rolf, C., Rose, D., Sauer, D., Schäfler, A., Schlage, R., Schnaiter, M., Schneider, J., Spelten, N., Spichtinger, P., Stock, P., Walser, A., Weigel, R., Weinzierl, B., Wendisch, M., Werner, F., Wernli, H., Wirth, M., Zahn, A., Ziereis, H., and Zöger, M.: ML-CIRRUS: The Airborne Experiment on Natural Cirrus and Contrail Cirrus with the High-Altitude Long-Range Research Aircraft HALO, *Bull. Amer. Meteor. Soc.*, 98, 271–288, <https://doi.org/10.1175/BAMS-D-15-00213.1>, 2016.
- Waliser, D. E., Li, J.-L. F., Woods, C. P., Austin, R. T., Bacmeister, J., Chern, J., Del Genio, A., Jiang, J. H., Kuang, Z., Meng, H., Minnis, P., Platnick, S., Rossow, W. B., Stephens, G. L., Sun-Mack, S., Tao, W.-K., Tompkins, A. M., Vane, D. G., Walker, C., and Wu, D.: Cloud ice: A climate model challenge with signs and expectations of progress, *J. Geophys. Res.*, 114, <https://doi.org/10.1029/2008JD010015>, 2009.
- Wendisch, M., Pöschl, U., Andreae, M. O., Machado, L. A. T., Albrecht, R., Schlager, H., Rosenfeld, D., Martin, S. T., Abdelmonem, A., Afchine, A., Araújo, A. C., Artaxo, P., Aufmhoff, H., Barbosa, H. M. J., Borrmann, S., Braga, R., Buchholz, B., Cecchini, M. A., Costa, A., Curtius, J., Dollner, M., Dorf, M., Dreiling, V., Ebert, V., Ehrlich, A., Ewald, F., Fisch, G., Fix, A., Frank, F., Fütterer, D., Heckl, C., Heidelberg, F., Hüneke, T., Jäkel, E., Järvinen, E., Jurkat, T., Kanter, S., Kästner, U., Kenntner, M., Kesselmeier, J., Klimach, T., Knecht, M., Kohl, R., Kölling, T., Krämer, M., Krüger, M., Krisna, T. C., Lavric, J. V., Longo, K., Mahnke, C., Manzi, A. O., Mayer, B., Mertes, S., Minikin, A., Molleker, S., Münch, S., Nillius, B., Pfeilsticker, K., Pöhlker, C., Roiger, A., Rose, D., Rosenow, D., Sauer, D., Schnaiter, M., Schneider, J., Schulz, C., de Souza, R. A. F., Spanu, A., Stock, P., Vila, D., Voigt, C., Walser, A., Walter, D., Weigel, R., Weinzierl, B., Werner, F., Yamasoe, M. A., Ziereis, H., Zinner, T., and Zöger, M.: ACRIDICON-CHUVA Campaign: Studying Tropical Deep Convective Clouds and Precipitation over Amazonia Using the New German Research Aircraft HALO, *Bull. Amer. Meteor. Soc.*, 97, 1885–1908, <https://doi.org/10.1175/BAMS-D-14-00255.1>, 2016.
- Wu, D. L., Austin, R. T., Deng, M., Durden, S. L., Heymsfield, A. J., Jiang, J. H., Lambert, A., Li, J.-L., Livesey, N. J., McFarquhar, G. M., Pittman, J. V., Stephens, G. L., Tanelli, S., Vane, D. G., and Waliser, D. E.: Comparisons of global cloud ice from

MLS, CloudSat, and correlative data sets, *J. Geophys. Res. Atmos.*, 114, <https://doi.org/10.1029/2008JD009946>, 2009.

Zhang, K., Liu, X., Wang, M., Comstock, J. M., Mitchell, D. L., Mishra, S., and Mace, G. G.: Evaluating and constraining ice  
5 cloud parameterizations in CAM5 using aircraft measurements from the SPARTICUS campaign, *Atmos. Chem. Phys.*, 13, 4963–4982, <https://doi.org/10.5194/acp-13-4963-2013>, 2013.

Zhang, Y., Macke, A., and Albers, F.: Effect of crystal size spectrum and crystal shape on stratiform cirrus radiative forcing, *Atmos.  
10 Res.*, 52, 59–75, 1999.



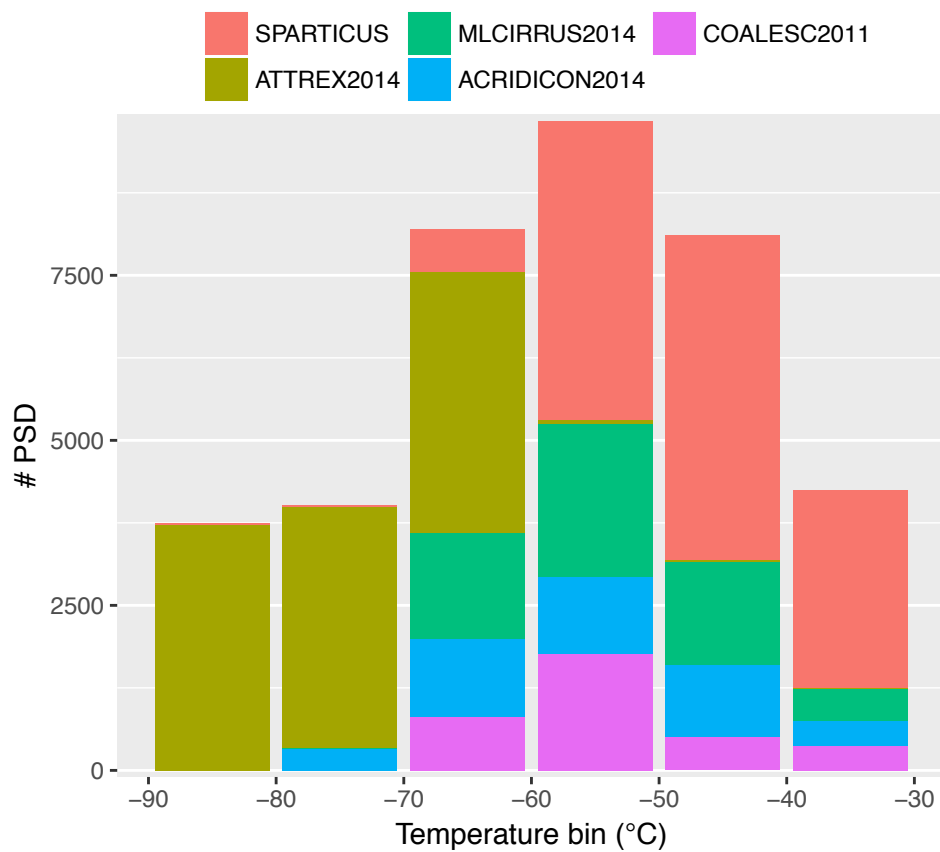


Figure S1: Stacked histogram showing the distribution of PSDs for each campaign described in Sec. 3.2 (color code above figure) per 10°C bins from -90 to -30°C.

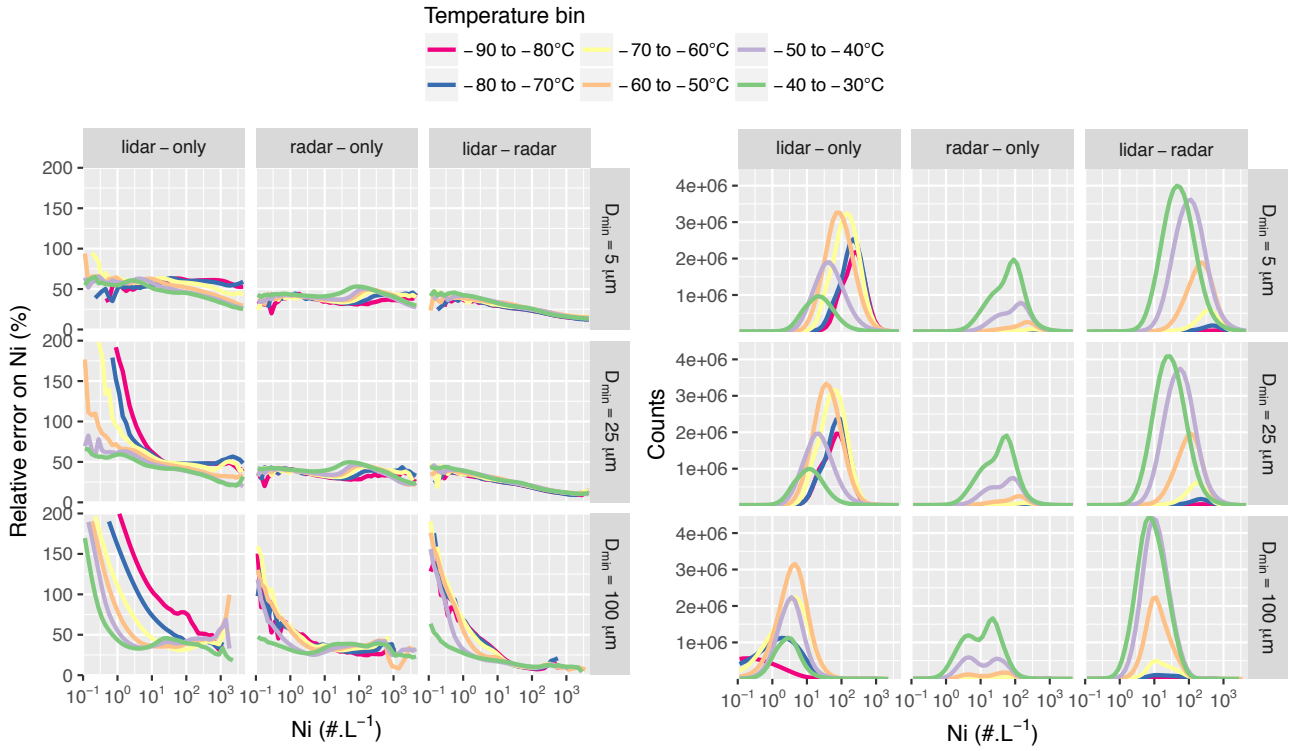


Figure S2: The left figure shows relative errors on DARDAR-LIM  $N_i$  estimates obtained by propagating the Gaussian standard-deviations on IWC and  $N_0^*$  provided in DARDAR operational retrievals (here based on 500 orbits; Jan-Feb 2008). The propagation method is mentioned in Sec. A2. These errors are provided as function of  $N_i$  per temperature bins (color lines), minimum diameter threshold bins for the  $N_i$  integration (rows; see Sec. 3.3), and instrumental conditions (columns; see Sec. A1). To clearly identify the dominating errors under different temperature and instrumental conditions, the right figure similarly indicates the distribution of  $N_i$  values in each panel.

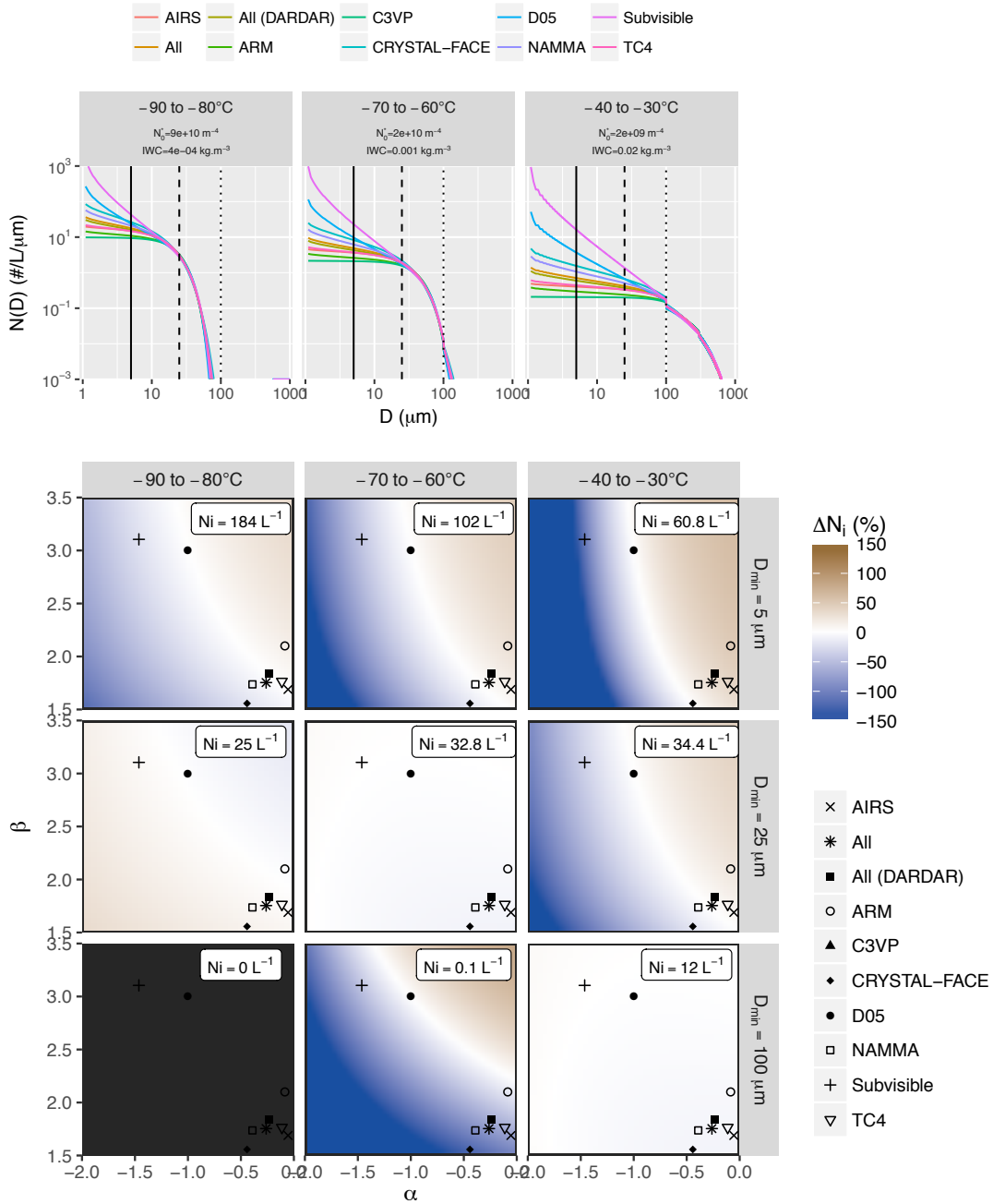


Figure S3: Analysis of the sensitivity of DARDAR-LIM  $N_i$  estimates to prior PSD shape assumptions ( $\alpha$  and  $\beta$  parameters in Eq. (4)). The top figure shows PSD predictions by the D05 parameterization in 3 temperature bins. For each bin, representative  $N_0^*$  and  $D_m$  values (indicated in the legend) have been selected based on all in situ campaigns described in Sec. 3.2. The D05 PSD is shown in blue and other colors correspond to PSDs computed using  $\alpha$  and  $\beta$  values extracted by Delanoë et al. [2014, D14] from multiple in situ campaigns (see Table 4 of that study or figure below). Vertical plain, dashed and dotted lines indicate the position of  $D_{\min} = 5, 25$  and  $100 \mu\text{m}$ , respectively. The bottom figure indicates relative biases  $\Delta N_i$  between predictions by D05 ( $N_{iD05}$ ) and the  $N_i$  obtained from a wide range of  $\alpha$  (x-axis) and  $\beta$  (y-axis) values. Brown and blue color therefore indicate an overestimation and underestimation of  $N_i$  by D05. Specific  $\alpha$  and  $\beta$  values from each campaign used in D14 are indicated by various point shapes. D05 is represented by a black dot.  $\Delta N_i$  is computed for each selected  $D_{\min}$  threshold (rows; see Sec. 3.3) and per temperature bins (columns) similarly to the top figures. The  $N_{iD05}$  values are indicated in each panel.

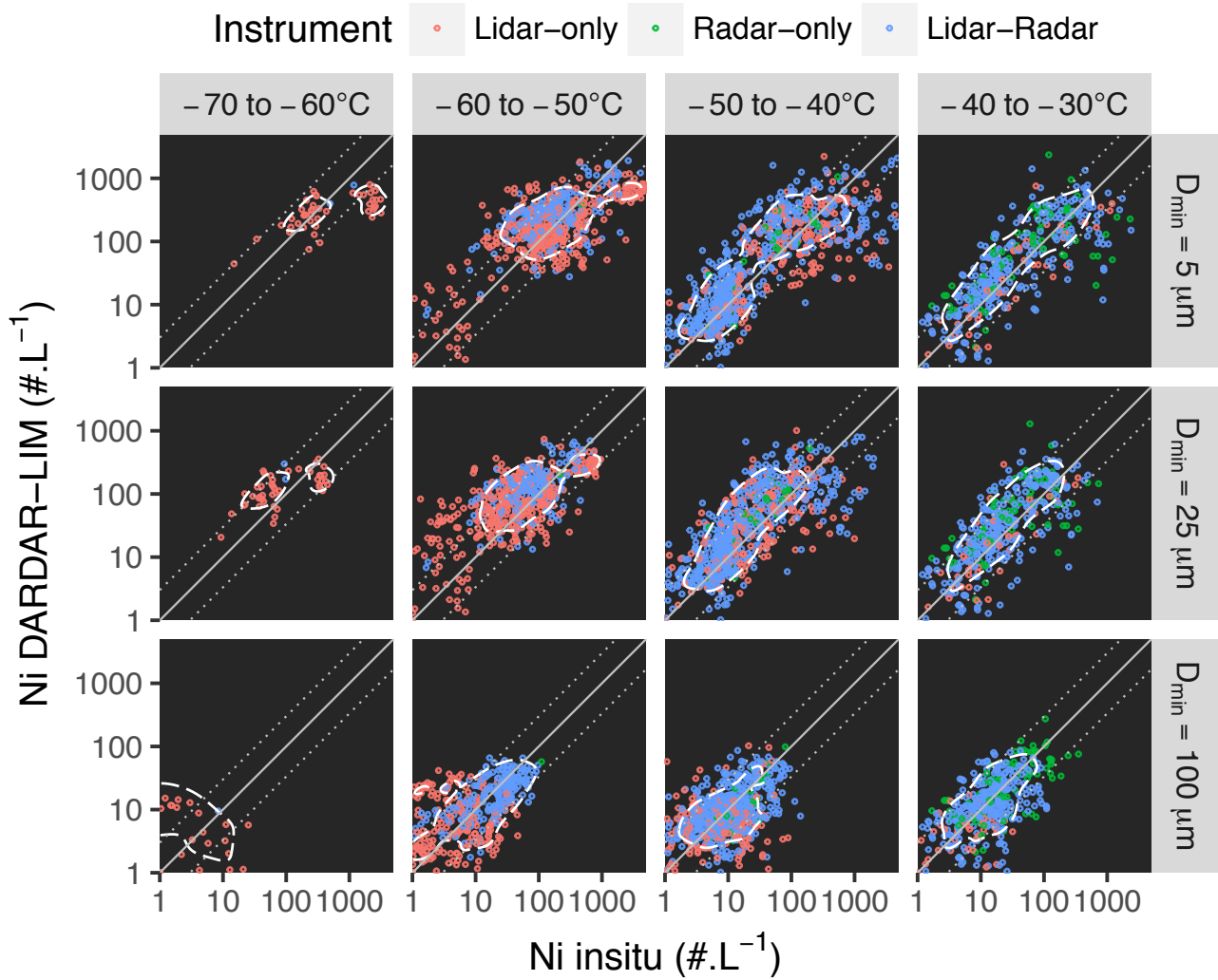


Figure S4: Similar to Fig. 2 of the paper, scatterplots of  $N_i$  retrieved by DARDAR-LIM as function of the co-incident 2D-S measurements during SPARTICUS. Red, green and blue dots indicate that  $N_i$  estimates were obtained in lidar-, radar-only and lidar-radar conditions. White isolines show the overall 68% confidence interval per  $D_{\min}$  and  $T_c$  bins.

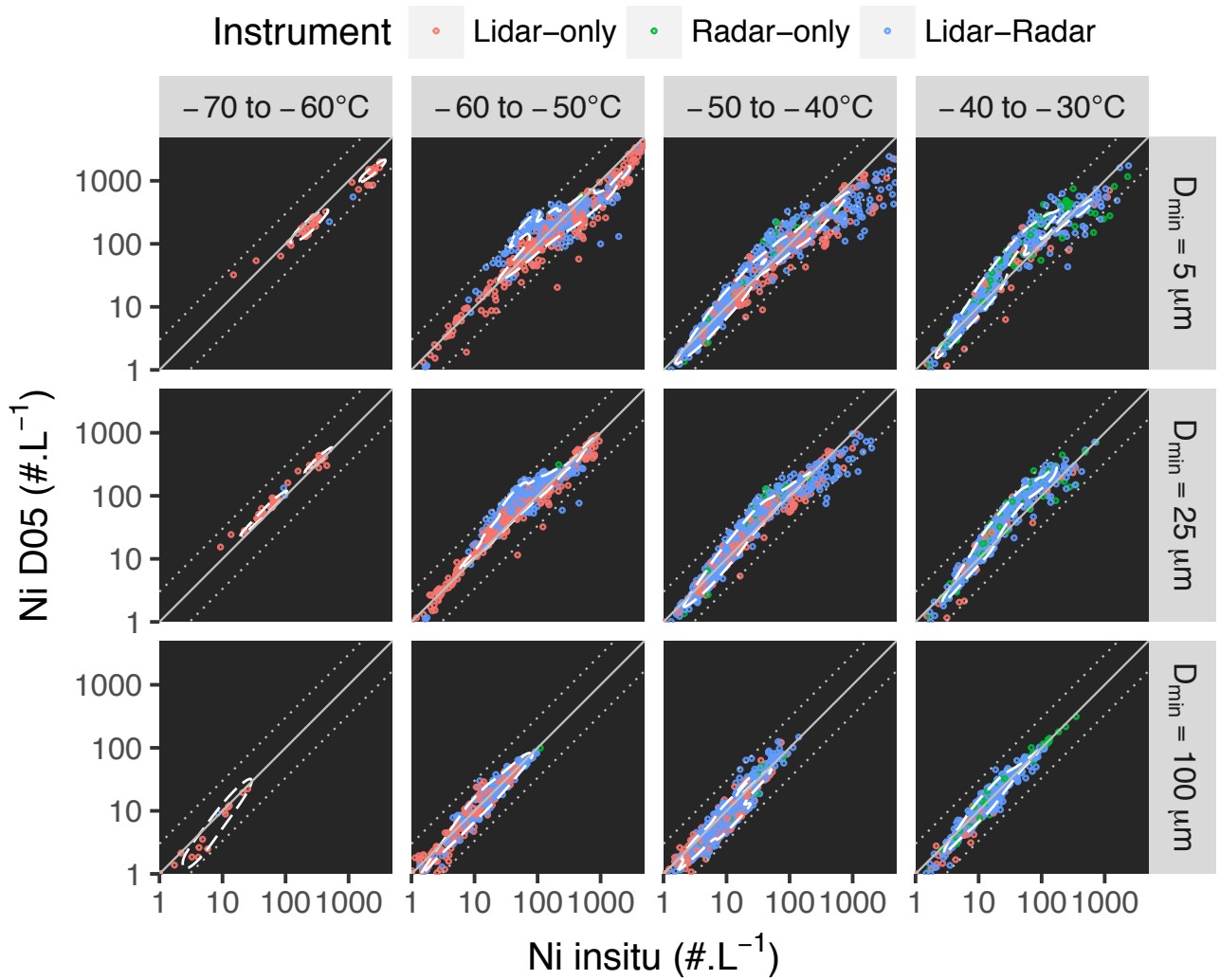


Figure S5: Similar to Fig. S4 but for D05 predictions (based on in situ IWC and  $N_0^*$ ) as function of 2D-S measurements.

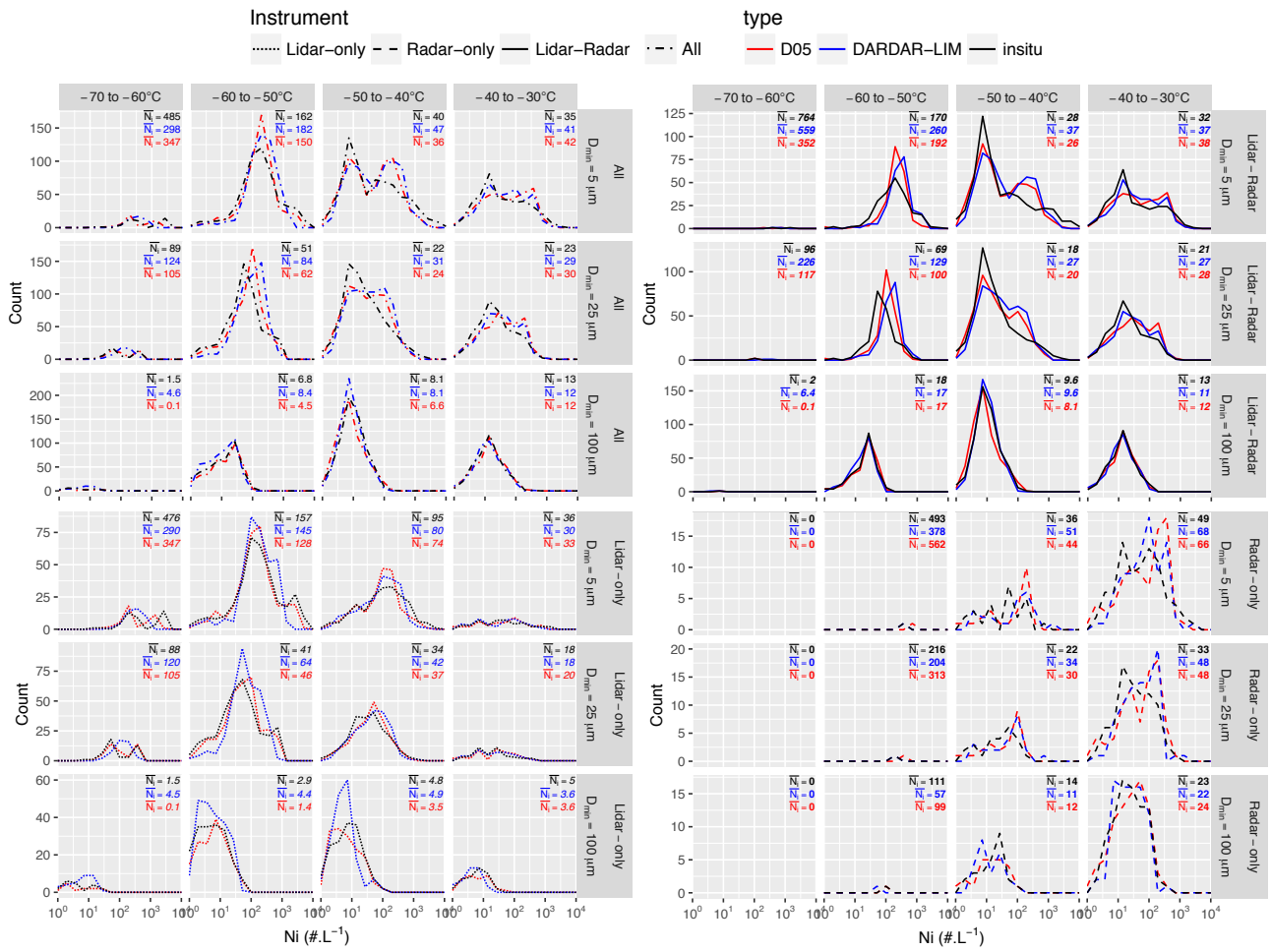


Figure S6: Similar to Fig. 4 of the paper, but the histograms are separated per instrumental conditions.



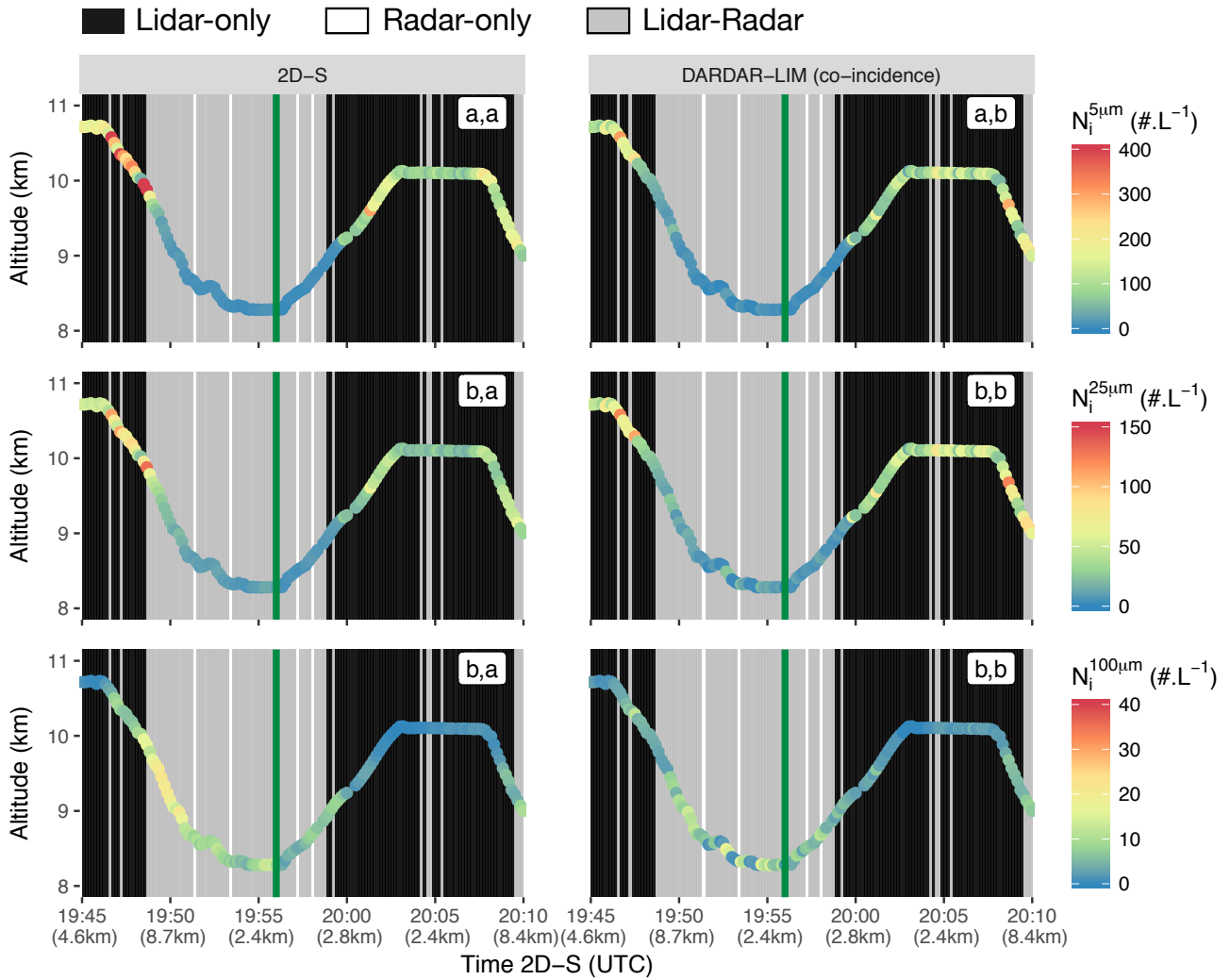


Figure S7:  $N_i$  measured by the 2D-S (first column) and retrieved by DARDAR-LIM (second column) along a projection of the Learjet-25 track on the A-Train overpass, show in Fig. 5(a-b) and Fig. 6 of the paper. The  $N_i$  is provided as function of the aircraft flight time (x-axis), with the distance to the satellite overpass track indicated in brackets. The overpass time (about 19:56 UTC) is shown by a vertical green line. The color background indicates if the DARDAR-LIM  $N_i$  has been estimated under lidar-only (black), radar-only (white) or lidar-radar (grey) conditions.

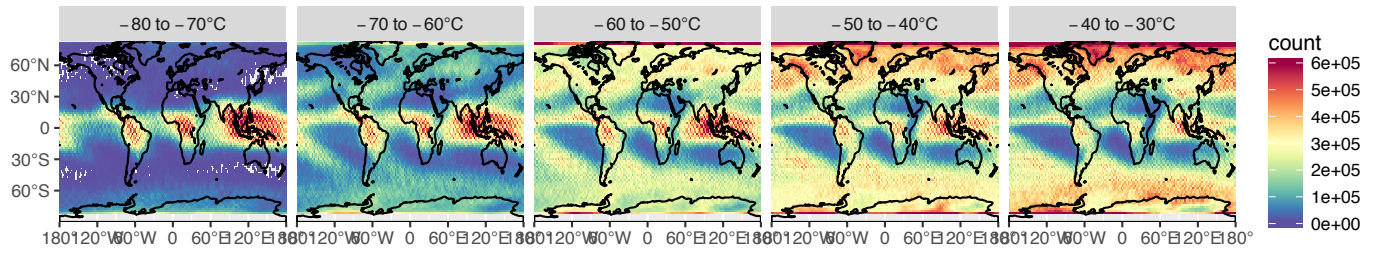


Figure S8: Spatial distribution of the count of  $N_i$  retrievals by DARDAR-LIM per temperature bin, corresponding to Fig. 7 of the paper.

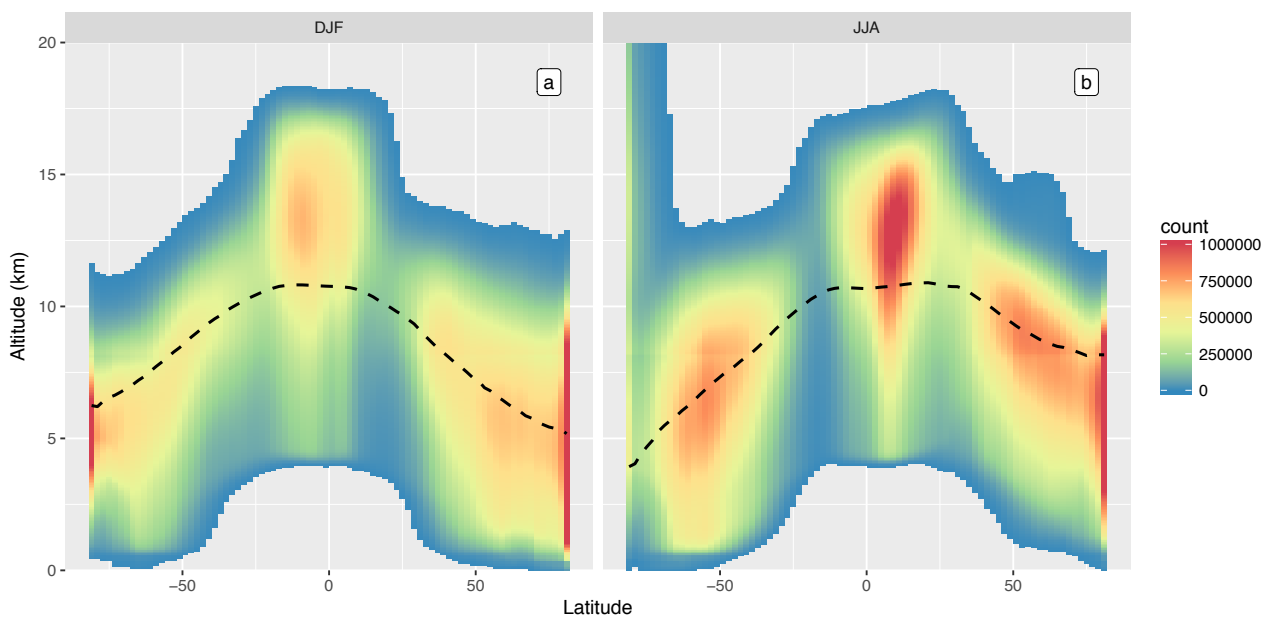


Figure S9: Spatial distribution of the count of  $N_i$  retrievals by DARDAR-LIM per temperature bin, corresponding to Fig. 9 of the paper.

## References:

- J. Delanoë, A. J. Heymsfield, A. Protat, A. Bansemer, and R. J. Hogan. Normalized particle size distribution for remote sensing application. *J. Geophys. Res.*, 119(7):4204–4227, 2014. doi: 10.1002/2013JD020700. URL <http://dx.doi.org/10.1002/2013JD020700>.